NORTHWESTERN UNIVERSITY

Tailoring Modular Spherical Nucleic Acids for DNA and RNA Delivery

A DISSERTATION

SUBMITTED TO THE GRADUATE SCHOOL
IN PARTIAL FULFILLMENT OF THE REQUIREMENTS

for the degree

DOCTOR OF PHILOSOPHY

Field of Biomedical Engineering

By

Andrew J. Sinegra

EVANSTON, ILLINOIS

September 2021

ABSTRACT

Tailoring Modular Spherical Nucleic Acid Structures for DNA and RNA Delivery

Andrew Joseph Sinegra

Effective delivery at clinically relevant doses is the central challenge limiting the implementation of nucleic acid-based therapeutics. Nucleic acids such as DNA or RNA of various lengths and structures expand the scope of functions of typical drugs. Nucleic acids can be used for: gene silencing, genome editing, gene replacement, immune system modulation, and theranostics. While significant progress has been made in each of these areas, therapy development requires extensive modification of both the sequence of the nucleic acids and the structure of their nanoparticle carrier to address key barriers to effective delivery. The main hurdles to effective delivery are clearance from circulation, crossing biological barriers, and effectively entering the target cell. The spherical nucleic acid (SNA) addresses some of the challenges of nucleic acid delivery through changes in the three-dimensional arrangement of nucleic acids. In these structures, the oligonucleotides, DNA or RNA, are radially oriented around a spherical nanoparticle template. This dense, outward arrangement improves nucleic acid delivery by increasing circulation time, resistance to degradation, and accumulation in many cell types. While these improvements have been documented with SNAs formed from inorganic nanoparticles such as gold nanoparticles (AuNPs), further characterization is necessary to explore the possible design space of modifications to nucleic acid sequences and the associated nanoparticle.

SNAs retain the delivery advantages of increased circulation time, resistance to degradation, and cellular uptake across many different nanoparticle types. These have included, but are not limited to: AuNPs, polymeric nanoparticles, liposomes, and proteins. The diversity of

synthesis and structure of SNAs has opened new avenues to exploring structure-function relationships, especially in the case of more modular organic nanoparticles, such as those made with lipid components (liposomes and lipid nanoparticles). This dissertation presents an investigation of how liposome and lipid nanoparticle (LNP)-based SNA structures can be tuned for enhanced delivery and function of nucleic acids *in vivo*. Chapter one builds the basis for this work by analyzing previous SNAs, their applications, and their structures. Chapter two describes an investigation of how liposomal SNAs can be tuned for enhanced DNA delivery to major organs outside of the liver using hydrophobic anchors with different affinities for the liposomal nanoparticle core. Chapter three explores a strategy to reprogram the function of existing LNP formulations by targeting them with DNA, forming LNP-SNAs. LNP-SNA formulations were optimized in cellular assays for greatest cytosolic delivery, and their function was assessed in wild-type mice in the context of mRNA delivery. Chapter four further investigates the relationships between LNP-SNA structure and where the nanoparticles distribute and function *in vivo*. The overall goal of these studies is to build a basis for creating nanoparticle structures with predictable delivery and function when delivering DNA or RNA inside cells.

_____

Thesis Advisor: Prof. Chad A. Mirkin

ACKNOWLEDGEMENTS

I would like to thank the many people who have helped me become a better human, thinker, and scientist along the way to getting my PhD. First, I would like to thank my parents for providing support for my growth and scientific curiosity. I remember fondly my Dad explaining the various cool things you could do if you became an engineer when I was a kid. I became excited about science and engineering when he told me how power plants work and how large in scale chemical production was in industry. I am grateful to my Mom for always being there to talk and laugh on the phone even in times when I didn't believe in myself. I would also like to thank my brothers Dave and Dan for providing some laughs along the way.

I am grateful to my advisor, Prof. Chad Mirkin, for providing a great environment for research as well as inspiration for my growth as a scientist. Working in the group with Chad made me realize that you don't need to be afraid to be competitive with the best in science and engineering, as long as you commit to doing things the right way and communicate effectively. I have become so much of a better scientist in the group. I would also like to thank my committee members, Profs. Evan Scott, Neha Kamat, and Nathan Gianneschi for their kind words and feedback over the years. I would especially like to thank Prof. Scott for teaching excellent courses in the BME department. In his biomaterials course, I learned the basics the right way and was inspired by his commitment that engineers should also know the basic science behind the materials and devices they design. Profs. Scott and Kamat also provide a great leadership example in the department, leading commitments to greater diversity, equity, and inclusion as well as recruiting students who are from backgrounds not represented enough in graduate school.

In the Mirkin group and at Northwestern in General, I am thankful to have met some of the best colleagues and friends. My experience started with my mentor, Dr. Jen Ferrer, who

believed in me even when I didn't believe in myself and helped me grow in a variety of areas: life, relationships, science, and even skincare. I would like to thank my collaborators Prof. Jason Wertheim and David Ivancic for their help on the manuscript in chapter 2 and insightful feedback. My lipid nanoparticle work would have not been possible without great discussions while injecting mice with Michael Evangelopoulos as well as discussion with Jungsoo Park. I would also like to thank others like Dr. Sara Rupich, Dr. Tanushri Sengupta, Dr. Katherine Bujold, Dr. Brian Meckes, and Dr. Devleena Samanta for their help over the years.

Finally, I am grateful for having the best friends in this world that I met at Northwestern. Sasha Ebrahimi is a great guy and extremely capable scientist with whom I have had so much fun with over my time at Northwestern. He was also always willing to help and very supportive. Jungsoo Park is a great friend and dad with whom I've had great scientific discussions about life, sports, and sneakers. The Mirkin BMEs Matt Vasher, Jasper Dittmar, and Michael Evangelopoulos are the best BME crew to have in the lab. I would also like to thank others who are always there for me: the BME fine dining crew of Max Greenberg and Yuni The, the Lakeview Distance Project of Justin Deffenbacher, Patrick Melendez, Michael Ryzhov, and Zach Whetstone, the Trivia team, and all of my other BME friends. Thanks everyone very much !

LIST OF ABBREVIATIONS

2’-OMe	2 prime O-methylation
cGAS	cyclic GMP-AMP synthase
Cy5	cyanine 5
dsDNA	double-stranded DNA
D-Lin-MC3-DMA	dilinoleylmethyl-4-dimethylaminobutyrate
DoE	Design of Experiments
DC	dendritic cell
DLS	dynamic light scattering
DNA	deoxyribonucleic acid
DOPC	1,2-dioleoyl-*sn*-glycero-3-phosphocholine
DOPE	1,2-dioleoyl-*sn*-glycero-3-phosphoethanolamine
DSPC	1,2-distearoyl-*sn*-glycero-3-phosphocholine
DOTAP	1,2-dioleoyl-3-dimethylammonium-propane
EE	encapsulation efficiency
FBS	fetal bovine serum
ICP-OES	inductively coupled plasma-optical emission spectrometry
i.v.	intravenous
IVIS	*in vivo* imaging system
LNP	lipid nanoparticle
LSNA	liposomal spherical nucleic acid
mRNA	messenger RNA
MPS	mononuclear phagocyte system

NGS	next-generation sequencing
NP	nanoparticle
PS	phosphorothioate
RNA	ribonucleic acid
RNP	ribonucleoprotein
siRNA	small interfering RNA
SNA	Spherical Nucleic Acid
SR-A	class A scavenger receptor
ssDNA	single-stranded DNA
SUV	small unilamellar vesicle
TAMRA	tetramethylrhodamine
TLR	toll-like receptor

TABLE OF CONTENTS

LIST OF TABLES, ILLUSTRATIONS, AND FIGURES

List of Figures

List of Tables

CHAPTER ONE

1 INTRODUCTION

1.1 Introduction to motivation for nucleic acid delivery

Understanding various structures of nucleic acids and their mechanisms of action within cells has led to several new classes of therapeutics. One of the first examples of this was the discovery of small interfering RNA (siRNA). The work of Mello and Fire elucidated an endogenous mechanism by which short double-stranded RNA sequences 19-23 bases in length could silence endogenous genes.[1] In this case, if the siRNA sequences were able to enter cells and be recognized by proteins part of the RISC complex, the antisense strand of the siRNA complexed with RISC, causing catalytic cleavage degradation of mRNA.[2–4] Because this mechanism, in theory, is only based on the siRNA sequence used, this strategy could be used to target nearly every gene present in the body, a range superior to that while using small molecule drugs. While this catalytic mechanism makes siRNA delivery more potent than delivery of antisense oligonucleotides (ASOs) on a per sequence basis,[5] the effects of siRNA-mediated mRNA degradation are estimated to last for 3-7 days.[6,7] Three siRNA therapeutics have been commercialized and approved by the U.S. Food and Drug Administration (FDA), all by Alnylam Pharmaceuticals, Inc.[8]

In addition to the transient gene silencing afforded by siRNA delivery, strategies have been explored to deliver nucleic acids that permanently alter the genome, which codes for every function that a cell can possibly use. The discovery of CRISPR and enzymes capable of editing the genome[9–11] and single bases[12] within it have led to an effort to create one-shot doses of drugs that cure disease by genome editing. While it is possible to carry out genome editing functions by delivering the active ribonucleoprotein complex, longer exposure to a nuclease or base editor increases the likeliness of potentially harmful off-target editing.[12,13] For safer delivery, it has

been shown that delivery of mRNA coding for the base editor along with a guide RNA can be accomplished using nanoparticle carriers, such as lipid nanoparticles (LNPs).[14–17]

While siRNA delivery and delivery of mRNA coding for genome editors are two of the most powerful applications of nucleic acid delivery, there are several other powerful applications that warrant mention. These include: gene replacement,[18,19] immune system modulation,[20–22] and theranostics.[23–25] While these applications unlock very powerful functions and may easily change targets *via* simple changes in DNA and RNA sequence, they are subject to many delivery limitations.

1.1 Barriers to delivery and function of nucleic acids in cells and in the body

The central challenge to implementing nucleic acid-based therapeutics and probes is delivery. The scope of this thesis will discuss the barriers to systemic administration of nucleic acids, or intravenous (i.v.) injection. While tissues such as the eye, skin, mucus membranes, and some tumors can potentially be reached *via* local delivery, systemic administration of a therapeutic aims to reach targets that are only met through the bloodstream. First, after injection, the nucleic acids and carrier will travel throughout the body in the circulation. The primary barrier to delivery is uptake and clearance by tissues that are not being targeted. The main parts of this barrier are kidney filtration[26,27], uptake by cells of the mononuclear phagocyte system (MPS),[28] and degradation by endogenous nucleases.[29] While the kidney filters the blood and receives a large portion of the cardiac output, cells of the MPS are present mainly in the liver and spleen, making the liver, spleen, and kidneys the primary organs that sequester nanoparticles carrying nucleic acids.[30,31]

After circulating around the body, nanoparticles must egress from the bloodstream to accumulate in the target tissue. Molecules larger than 5 nm in diameter do not readily cross gaps

in the capillary endothelium in most tissues.[32] However, there are some tissues that readily allow the entry of larger molecules, including the spleen and liver.[33] While junctions between endothelial cells may not allow nanoparticles to extravasate from the capillaries of many organs, recent research highlights that nanoparticles may be transported across endothelia through active mechanisms. Sindwani et al studied mechanisms of gold nanoparticles entering solid tumors and found that up to 97% of nanoparticles enter tumors through an active transcytosis process rather than enhanced permeability of the endothelial barriers.[32]

If nanoparticles can enter tissues by crossing endothelial barriers, there are still several hurdles to acting in the target cell. Nanoparticles must diffuse through the extracellular matrix within the tissue, often very slowly, to enter the cell type of interest.[34] Uptake into many cell types is not trivial as well, nanoparticle internalization depends on the cell type, the cell's state, as well as the mechanism of uptake.[35] Finally, within the cell, nanoparticles are often taken up into cell compartments that prevent their desired mechanism of action. Nanoparticles are often taken into compartments of the cell called endosomes, which need to be escaped for the nucleic acid cargo to act in the cytoplasm. If nanoparticles are not effective in escaping endosomes, they will be trafficked through endo-lysosomal pathways, where decreased pH and degradative conditions in the lysosome will degrade and eliminate the nanoparticles.[36] Escape from cell compartments often determines the median effective concentration (EC_{50}) of nanoparticles in cellular assays, as the rate-limiting step in functions such as siRNA binding to mRNA or mRNA being expressed within the cytoplasm of cells is the RNA being released into the cytoplasm. A small portion of nanoparticles escape the endosomes of cells. Gilleron, et al found using lipid nanoparticles that less than 2% of the encapsulated siRNA escaped endosomes.[37] Together,

nanoparticle design for clinical therapeutics and diagnostics needs to address both larger-scale *in vivo* barriers such as major organs and the circulatory system as well as small-scale barriers within cells and their compartments. Structure-distribution and structure-function studies illuminate how characteristics of materials interact with these barriers.

1.2 Spherical Nucleic Acids change the interactions of nucleic acids with cells

Spherical Nucleic Acids (SNAs) are a unique form of nucleic acids first explored more than 20 years ago. This form of nucleic acid is defined by a dense, outward arrangement of an oligonucleotide around a nanoparticle core. The first SNA structures were derived from thiol-capped oligonucleotides densely arranged around a gold nanoparticle (AuNP) core.[38] These nanoparticles exhibited reversible sequence-dependent aggregation caused by hybridization of a complimentary linker strand. This property indicated that SNA structures retained sequence recognition ability conferred by the DNA bond even when fixed to a nanoparticle surface on one end.

Since the advent of the SNA structure, many different oligonucleotide sequences and nanoparticle core structures have been used to form these architectures. Some of the most highly used structures for delivery of nucleic acids have been based on AuNPs,[39–42] poly-lactic-co-glycolic acid (PLGA) nanoparticles,[43] and liposomes.[44–48] Besides the ability to polyvalently bind complementary nucleic acids and other targets, a powerful advantage of these structures is that the properties mediated by the unique SNA architecture are largely retained between different nanoparticle core structures.

While the nanoparticle core structures can vary, the general synthesis procedure is also generalized between structures. The synthesis involves generally two components:1.) a

nanoparticle core presenting conjugation sites or a reactive surface and 2.) a modified oligonucleotide sequence containing a linker designed to react with the nanoparticle core. Oligonucleotide sequences used to form SNAs have included DNA,[38] siRNA,[40] DNA:RNA hybrids,[49] dsDNA sequences designed for detection,[50] and aptamers.[51] While oligonucleotide structures may be single-stranded, double-stranded, or contain secondary structures, SNA synthesis uses a generalizable oligonucleotide design containing three general regions: 1.) the functional part of the sequence, 2.) a spacer region, and 3.) a linker adding chemistry used to anchor the DNA to the nanoparticle surface.[52] There are many possible oligonucleotide and nanoparticle core designs that may be used to form SNAs. Insights on structure-function

relationships inform how SNAs may be used to address biological barriers in the body for more effective delivery.

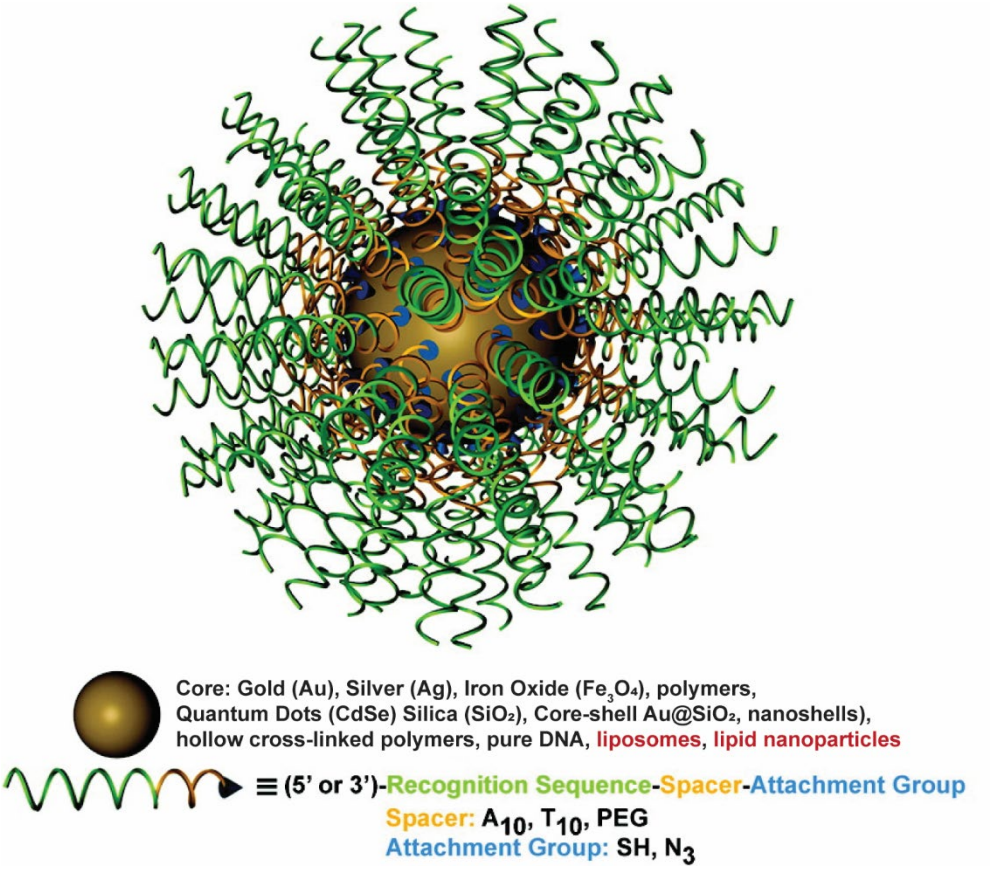

Figure 1.1 *SNA synthesis method is generalizable between nanoparticle core structures.* SNAs are typically formed from spherical nanoparticle cores which react with modified oligonucleotide (DNA, RNA or DNA:RNA hybrid) sequences to present DNA in an outward, radial fashion. Oligonucleotide sequences are typically comprised of three different regions, (from outward facing end to core-facing end): a recognition or functional sequence, a spacer region, and an attachment group. These include, but are not limited to, those sequences listed above. This figure is adapted from ref[52], Copyright 2012 the American Chemical Society.

1.2 Structure-function relationships of SNAs interacting with cells and tissues

Due to their structure, nucleic acids have poor delivery properties when delivered without a carrier. The high mass (> 10 kDa) and negative charge of DNA and RNA does not allow for transport across biological barriers in the body, entry into cells, or escape from cell compartments. While commercially available transfection reagents Dharmafect™, Lipofectamine™, and others are useful for screening the function of different nucleic acids, these reagents are limited by acute cytotoxicity at higher doses.[53] The dense three-dimensional arrangement of SNAs changes the interactions of nucleic acids with cells, inhibiting degradation by nucleases, increasing uptake into many different cell types, and allowing SNAs to cross biological barriers.

1.2.1 *Decreased nuclease degration*

SNA architectures increase the half-life of nucleic acids in serum by preventing degradation of the oligonucleotides by nucleases. With AuNP-based SNAs (AuSNAs), the SNA structure with the highest density of DNA on its surface, the degradation rate of ssDNA by DNase I is 4.3-fold lower than an identical DNA sequence in linear form (Figure 1.2A).[54] In addition, with siRNA-based AuSNAs, different patterns of serum nuclease activity are detected compared to the linear form. This research suggests that fixing an oligonucleotide sequence to a nanoparticle core alters the local environment and access of serum nucleases to hydrolyze RNA sequences.[55] In addition, sequence modifications that are common to linear oligonucleotides, such as 2'-*O*-methylated bases (2'-OMe), improve RNA stability on SNAs, where 2'-OMe bases increased half-life in serum by 10-fold.[55]

1.2.2 *Rapid uptake into many cell types*

DNA and RNA sequences do not readily enter cells without modifications. The cell membrane of most cells is negatively charged and impermeable to high mass nucleic acids. Because commercially available transfection reagents are not safe to use therapeutically, other modifications have been pursued to increase the cellular uptake of nucleic acids. These modifications are mostly aimed at conjugating the oligonucleotides to a hydrophobic moiety that will increase the bioavailability and receptor-mediated uptake of the sequence. siRNA conjugation to cholesterol increases bioavailability in hepatocytes and jejunum and allows for therapeutic gene silencing in those organs.[56] Modifications with amino sugars such as N-Acetylgalactosamine (GalNAc) increase receptor mediated uptake into hepatocytes.[57] This strategy leverages endogenous lipid trafficking mechanisms to allow for uptake of the sequence through the LDL receptor, which is expressed by hepatocytes.

SNA structures enhance uptake of DNA and RNA sequences compared to the linear nucleic acid *via* scavenger-receptor mediated endocytosis (Figure 1.2B).[58] SNAs rapidly enter over 50 cell types *in vitro* by engaging with Class A scavenger receptors (SR-A) in a lipid raft, caveolin-dependent manner. Many different cell types express scavenger receptors,[59] which bind negatively charged polymers. Thus, SNAs represent a strategy to use charge density of radially oriented nucleic acids for increased cellular uptake.

1.2.3 *Sequence-dependent cellular uptake and protein corona formation*

While scavenger receptors largely dictate SNAs' uptake into cells, the DNA sequence presented on the surface of SNAs also dictates intracellular delivery. AuSNAs functionalized with G-quadruplex ($(GGT)_{10}$) forming DNA sequences exhibit greater uptake into many cell types than those functionalized with poly(T) or poly(A) DNA sequences (Figure 1.2C).[60] The

delivery enhancement of G-quadruplex containing SNAs (compared to poly(T) SNAs) is greater in cells expressing SR-A at high levels. This may be because G-rich oligonucleotides are high-affinity ligands of scavenger receptors.[61] In addition, G-quadruplex secondary structures exhibit enhanced stability when presented in the SNA architecture. G-rich DNA sequences presented on SNAs exhibit a ~15ºC increase in melting temperature compared to linear DNA sequences.[62]

The DNA sequence which comprises the SNA dictates what proteins adsorb to the surface of the nanoparticles in addition to their affinity for SR-A. While differences in uptake are observed when comparing G-Rich and poly(T) SNAs, there are also significant differences in the proteins which comprise the protein corona on the surface of each. After incubation in serum, G-rich SNAs have 4-times as many proteins adsorbed to the surface of the SNA compared to poly(T) SNAs (Figure 1.2D).[62] In addition, while there is a greater quantity of proteins adsorbed in the case of the G-rich SNA, there is a difference in what types of proteins are present on the surface. Some proteins are part of foreign material recognition and clearance pathways in the body which may change the distribution of the SNAs. G-rich SNAs adsorb proteins that are part of complement pathways,[63] which contribute to the clearance of nanoparticles.[64] Complementary cellular uptake studies revealed that complement protein adsorption was associated with greater uptake into macrophage cells, which are present in high amounts in the liver and spleen and may represent a mechanistic explanation for differences in distribution after injecting SNAs.

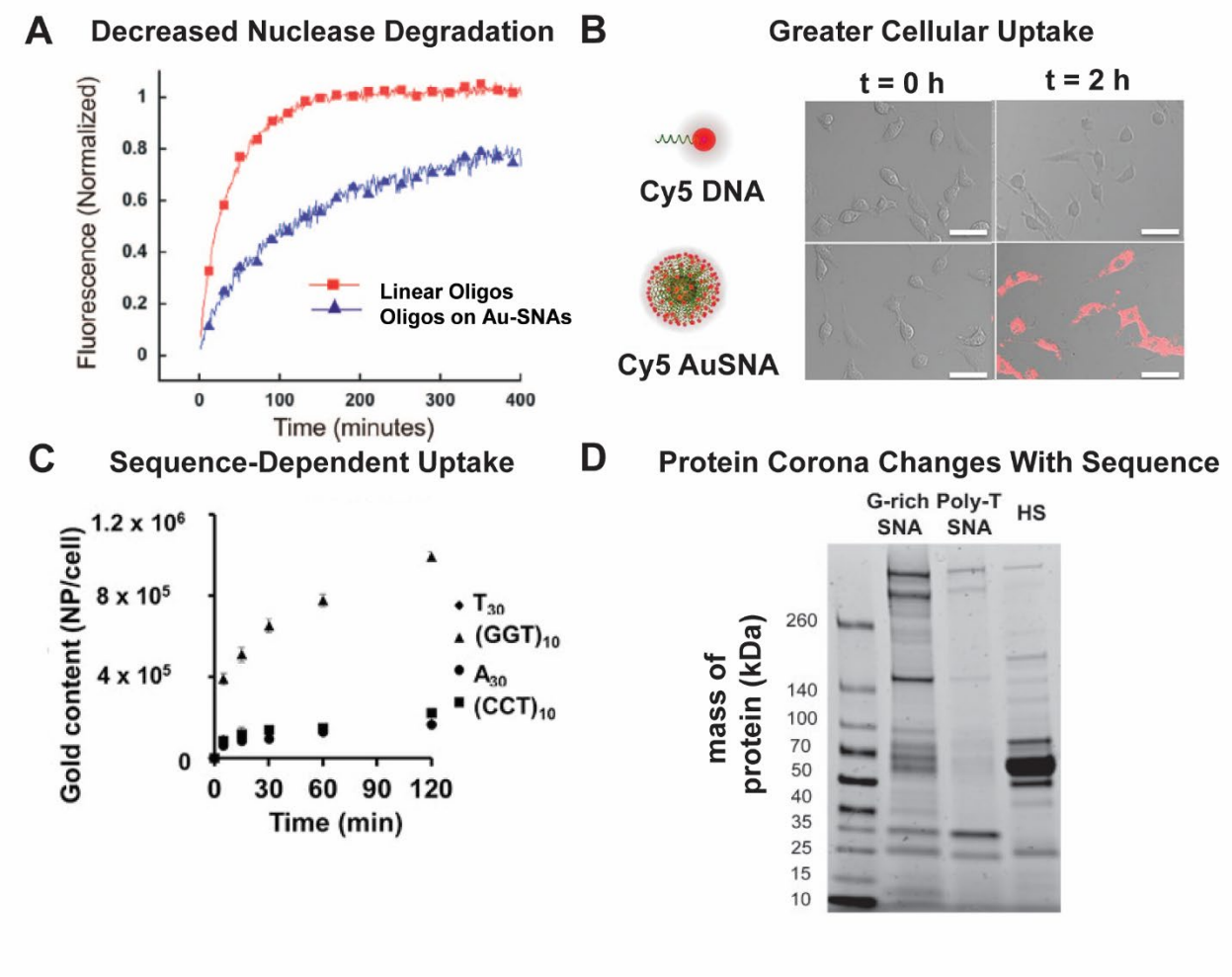

Figure 1.2 *Properties of SNAs when interacting with cells.* (A) DNA presented in an SNA architecture is degraded at a slower rate than the equivalent linear sequence. Modified with permission from ref[54], Copyright 2009 American Chemical Society. (B) DNA presented in the SNA architecture rapidly enters cells. Modified with permission from ref[65] reprinted with permission of AAAS. (C) SNAs functionalized with a G-rich sequence $(GGT)_{10}$ enter cells in greater amounts than those with T-rich, A-rich, or C-rich sequences. (HaCaT cells). Modified with permission from ref[60], Copyright 2015 John C. Wiley and Sons, Inc. (D) G-rich SNAs contain a greater number of adsorbed proteins per nanoparticle after incubation in human serum

(HS) than Poly(T) SNAs. Adapted with permission from ref[62], Copyright 2014 John C. Wiley and Sons, Inc.

1.2.4 *SNAs alter biodistribution of both the nucleic acids and associated nanoparticle*

The biodistribution of SNAs after systemic administration has been studied in wild-type mice. SNA architecture alters the distribution of both the DNA sequence and the associated nanoparticle. In addition, as hypothesized from differences in protein corona, there are sequence-dependent effects on biodistribution of SNAs. G-rich SNAs accumulate more than 20% more in the liver after 8 h and 24 h circulation times compared to Poly(T) SNAs.[63] In the spleen, G-rich SNAs accumulate in 3% greater amounts after 8 h (Figure 1.3A). With SNAs comprised of a protein core, the protein's circulation time increases with DNA conjugated to its surface versus the bare protein, while retaining activity in cells (Figure 1.3B).[66]

SNAs' distribution in tumour models has also been characterized. The pharmacokinetic profile of AuSNAs functionalized with siRNA has been characterized in models of glioblastoma multiforme (GBM). The half-life of SNA distribution was 0.98 min. and the half-life of elimination was 500 min.[40] In mice bearing GBM tumors, the highest degree of SNA distribution in terms of nanoparticles per gram of tissue was in the liver and spleen. Approximately one tenth of the nanoparticle per gram of tissue amount was present in the brain tumor (Figure 1.3C).

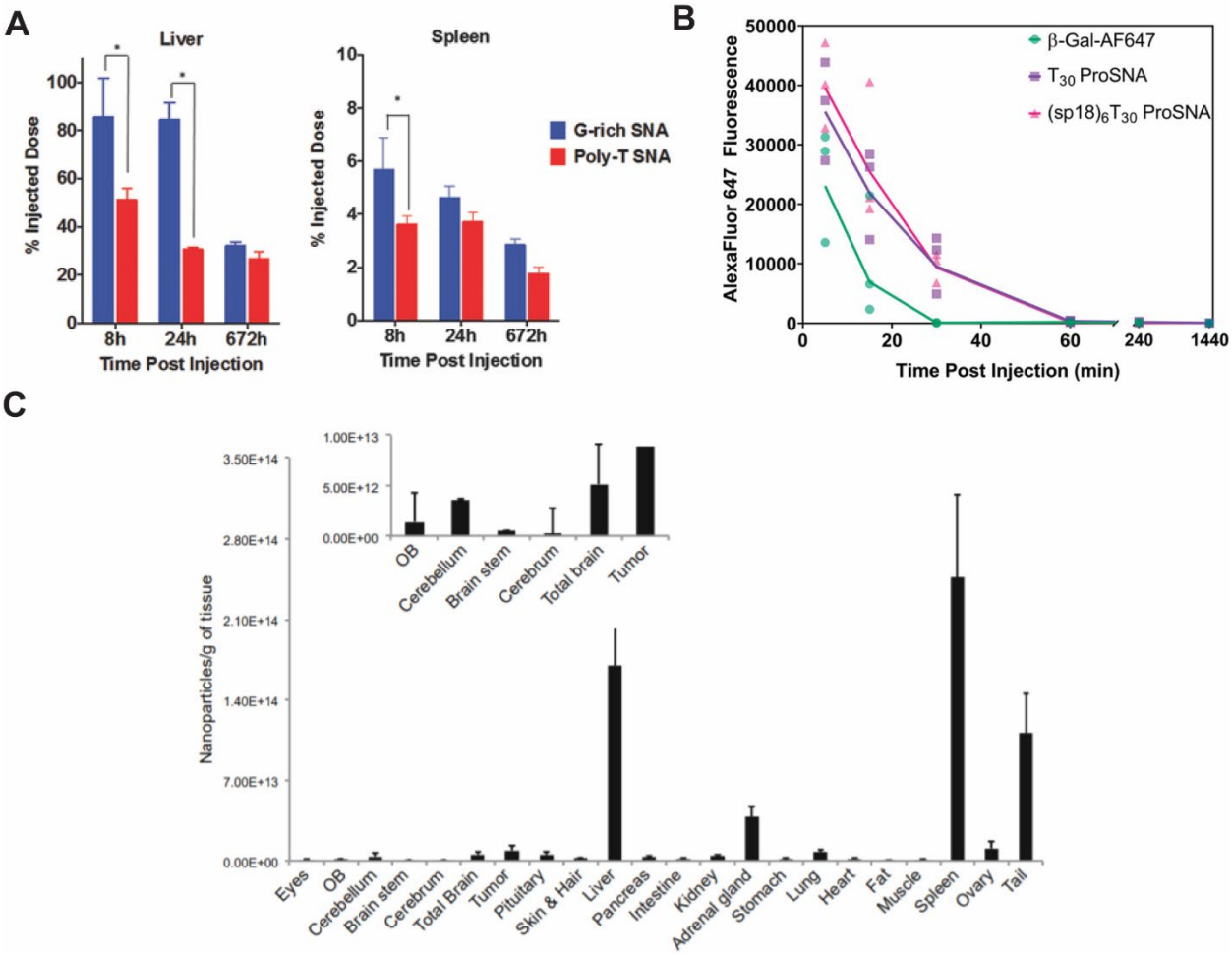

Figure 1.3 *Biodistribution of different SNA conjugates.* (A) G-rich AuSNAs exhibit greater delivery to the liver at 8h and 24h post-injection in the liver as well as 8h after injection in the spleen compared to Poly(T) SNAs. Adapted from ref[63], Copyright 2019 John C. Wiley and Sons. (B) Protein SNAs (ProSNAs) formed from β-Galactosidase conjugated to AlexaFluour 647 (β-Gal-AF647) circulate longer than the bare protein in mice. Adapted from ref[66], Copyright 2020 American Chemical Society. (C) Distribution of AuSNAs functionalized with siRNA in mice bearing GBM tumors. Adapted from ref[40], reprinted with permission of AAAS.

1.2.5 *SNAs are able to cross important biological barriers*

Assessing distribution of SNAs informs potential targets for therapeutics. However, to inform future design of SNAs, interactions with important biological barriers must be assessed. In the same study, SNA delivery to brain tumors was imaged using silver stained organ sections.[40] SNAs appear to accumulate in both tumor and normal brain tissue. SNAs for targeting GBM demonstrate the utility of receptor-mediated cellular uptake for nucleic acid delivery. In a 3-D culture model of cells that form the blood-brain barrier, SNAs are able to use receptor mediated transcytosis to cross brain microvasculature endothelial cells to enter astrocytes (Figure 1.4).[40] This transport is also inhibited by Poly I treatment, indicating that scavenger receptors contribute to the receptor-mediated endocytosis of SNAs into brain tumors.

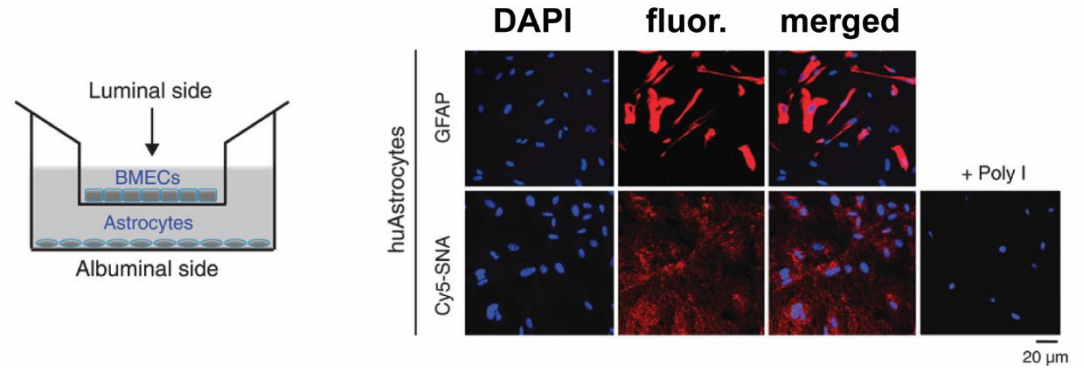

Figure 1.4 *SNAs* cross endothelial cell monolayers *via receptor-mediated transcytosis.* In a noncontact coculture model of the blood-brain barrier, SNAs are able to enter and cross BMECS, the endothelial cells in capillaries in the brain, via receptor-mediated transcytosis to enter astrocytes at the bottom of a transwell plate. Poly I inhibition of scavenger receptors suggests this is an active transport mechanism related to scavenger-receptor mediated uptake of SNAs. Adapted from ref[40] reprinted with permission from AAAS.

Another important barrier that SNAs have addressed is crossing the epidermal barrier of the skin. Topical delivery presents a local delivery method to address the over 200 skin-related disorders with a genetic basis.[67] SNA structures delivered within a common moisturizer are able to enter the epidermis of both wild-type mice and human skin samples and deliver siRNA sequences designed to knock down a driver of skin disorders.[68,69] The local delivery of SNAs also increased safety of the therapeutics, as no inflammatory cytokine activation was detected, and very little SNAs were detected in internal organs.[68] While the initial studies of SNAs for topical delivery of siRNA were based on AuSNAs, the utility of this approach has expanded to more biodegradable LSNAs. LSNAs delivering ASOs targeting TGF-β1 were able to silence its expression in models of wound healing.[70] The gene silencing effect was sufficient to decrease abnormal scar formation and improve scar histology. The use of multiple nanoparticle cores and nucleic acid types to deliver DNA and RNA across important biological barriers exemplifies that SNAs' unique transport properties across cells and in circulation can be used for a diverse set of therapeutic applications.

1.3 Structure-dependent delivery of DNA and RNA for therapeutics and diagnostics

The modular nature of SNA structures and their facile synthesis allows for use of different nucleic acid types based on application. The nanoparticle core serves the purposes of: 1.) presenting a scaffold for functionalizing a nucleic acid, 2.) adds chemical and physical properties to the conjugates including additional functionality and control over drug release. Typically, the nucleic acids are used for targeting of the nanoparticle core and function depending on application. In addition to nucleic acids, SNAs have been designed to incorporate, cleavage sites[71], antibodies[72], small molecules[73], and aptamers[51,74].

1.3.1 *Gene regulation using AuSNAs and LSNAs*

Spherical nucleic acids functionalized with ASOs and siRNA have been used for gene regulation applications. AuSNAs have demonstrated effective delivery of both ASOs and siRNA sequences in GBM tumors.[40,41,75] This function indicates that AuSNAs, which are 13 nm in diameter, are able to effectively penetrate the blood-brain barrier, enter the target cells, and bind mRNAs and miRNAs. AuSNAs are also effectively able to deliver nucleic acids into the skin, delivering siRNA to assist diabetic wound healing[69] and decrease inflammation[68].

The long-term fate of inorganic nanoparticles in the body remains a safety concern, as their lack of degradation and clearance may pose an issue when systemically administered, as opposed to local delivery.[76] As favor has shifted towards more biodegradable nanoparticle structures, so has the focus of SNA-based therapeutics. LSNA structures have also been developed for ASO delivery (Figure 1.5).[45,70,77] In these degradable nanoparticles, the ASOs are conjugated to a lipid or sterol on the surface of a liposome to form LSNAs. It is hypothesized that the LSNA enters a cell, degrades to release the ASO conjugates, and the ASO conjugates subsequently bind to the target mRNA.[45] LSNAs exhibit gene silencing activity at micromolar concentrations by DNA.[45,77] While this is promising for using LSNAs as non-toxic delivery agents in some applications, especially those using local delivery methods, this order of activity is not likely effective for systemically administered nanoparticles.

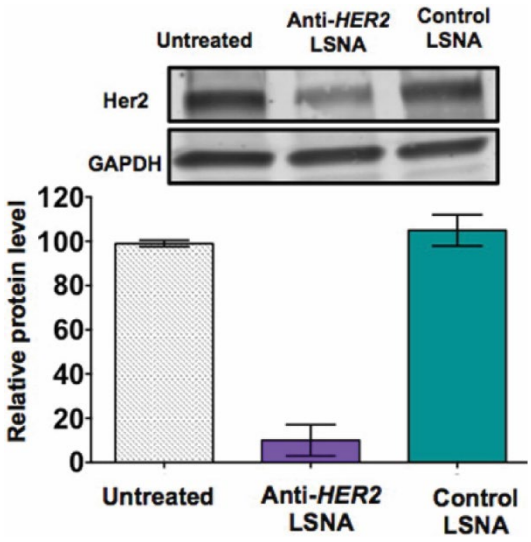

Figure 1.5 *LSNAs effectively delivery ASOs attached to the liposome surface.* LSNAs constructed by attaching ASOs targeting the HER2 gene in SKOV-3 cells. 1 uM concentration is required to achieve this ~ 90% protein silencing effect. Adapted from ref[77], Copyright 2016 American Chemical Society.

1.3.2 *mRNA detection using NanoFlares*

SNAs are able to bind complimentary DNA and RNA sequences with high affinity and cooperativity. This property is especially useful for detection of contents within live cells. Combined with the fluorescence-quenching ability of AuNPs, SNA probes called Nano-flares have been developed for the detection of mRNA in live cells.[50] In this system, a sequence complimentary to the target mRNA is functionalized to a gold nanoparticle surface. Hybridized to this sequence is a short "flare" strand complimentary to the targeting strand containing a fluorophore. In this state, the fluorescence is "off" because the flare strand is close enough to the gold nanoparticle core to quench its fluorescence. If the nanoparticle enters cells, escapes cell compartments, and binds complimentary mRNA in the cytosol, the mRNA binding will displace the flare strand, as it contains greater complementarity to the sequence found on the SNA. This

turns the signal from “off” to “on” and mRNA expression can be measured using fluorescence. This fluorescence turn-on system has allowed for the creation of many different sets of probes. These include multiplexed NanoFlares[42] and aptamer NanoFlares[74] which turn on in response to an aptamer binding to an analyte.

A limitation of the original Nano-flare design[50] is that the fluorophore-quencher system can give a false positive signal if the probes are somehow desorbed from the nanoparticle surface or they are degraded by nucleases. A recent approach to addressing these limitations has been to combine the SNA architecture with forced intercalation (FIT) probes and aptamers which use a viscosensitive dye to turn on in response to binding of the complimentary sequence.[51,78] This design simplifies fluorophore-quencher systems into one DNA or RNA sequence containing the FIT dye. Thus far, this approach has been used on the surface of protein-based SNAs (ProSNAs) to create multifunctional probes (Figure 1.6). In this case, a glucose oxidase protein core can be used to detect glucose, while the FIT probe conjugated to the protein can be used to measure pH. The cellular uptake property conferred to the protein by the DNA on its surface combined with careful probe design illustrates that SNA architectures can use both their delivery properties and the binding dynamics of DNA to create effective probes.

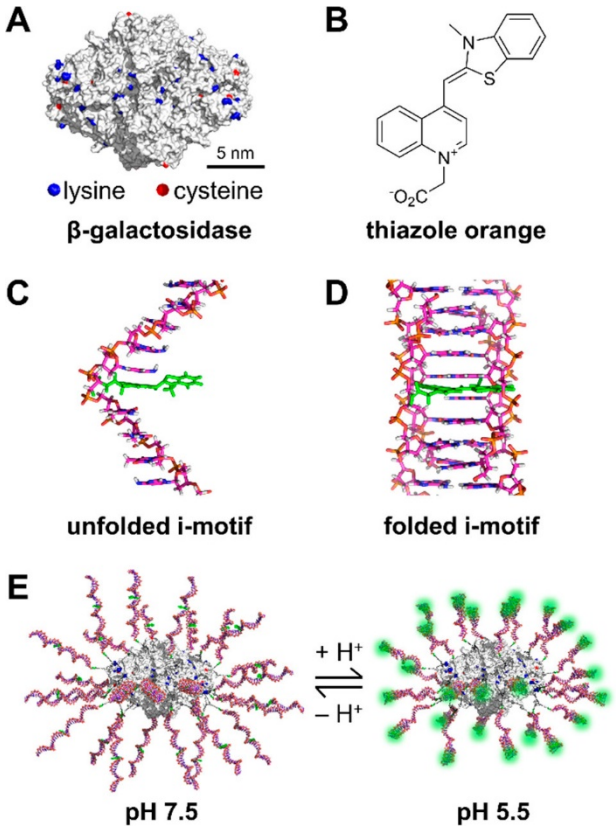

Figure 1.6 *Protein SNAs demonstrate a strategy to use both the nanoparticle core and DNA shell for targeting, detection.* (A) structure of β-galactosidase protein. (B) Structure of thiazole orange dye used as the forced intercalation (FIT) dye. (C) Structures of i-motif DNA sequence unfolded at pH 7.5 and (D) folded at pH 5.5. Folding of the aptamer causes fluorescence turn-on of the thiazole orange dye. (E) Demonstration of Protein SNA probe comprised of a protein core and modified i-motif DNA which can be used for dual detection using the protein to detect the substrate of the enzyme and the DNA sequence to detect another analyte, in this case pH. Adapted from ref[51], Copyright 2020 the American Chemical Society.

1.3.3 *Immune system modulation using LSNAs*

A greater level of control of DNA delivery afforded by SNAs has opened avenues to use DNA delivery to modulate the immune system. Multiple toll-like receptors (TLRs), receptors of

the innate immune system, respond to binding of nucleic acids. SNAs can effectively enter cells and display multiple ligands for these receptors simultaneously and have been used to deliver both immunostimulatory and inhibitory DNA and RNA sequences.[46,47,79] Key advances have occurred when the modularity of lipid-based SNA structures has been leveraged to create more effective therapeutics and vaccines. Skakuj et al demonstrated that, by controlling the release kinetics of an antigen using DNA linker chemistry, LSNA structures could be engineered to enhance T-cell activation.[80]

Further studies have evaluated LSNA structures as potential cancer vaccines. Yamankurt et al demonstrate that the high parameter design space of LSNAs can be explored to find patterns involving the adjuvant, antigen, and nanoparticle components of the vaccines.[81] With a relatively small portion of the design space, high-throughput screening design combined with predictor analysis can find features which significantly increase LSNA function. Evaluating structure-function relationships has also augmented LSNA vaccine function in aggressive breast cancer tumor models. LSNAs with encapsulated oxidized tumor lysate inhibit tumor growth and increased mouse survival in models of triple-negative breast cancer (TNBC).[82] LSNAs also exhibit stability-dependent function as vaccines. By increasing the melting temperature of the lipids which comprise the liposome core, the nanoparticle stability can be increased. Callmann et al found that more stable LSNA structures exhibited greater anti-tumor efficacy as vaccines in a 4T1 TNBC model.[83] In the case of vaccine structures, LSNAs demonstrate that highly modular nanoparticle structures should be effectively optimized and screened to define the parameters needed for therapeutic activity.

1.4 Lipid nanoparticles for cytosolic delivery of DNA and RNA

1.4.1 *Lipid nanoparticles*

Lipid nanoparticles (LNPs) are a highly modular class of biodegradable nanoparticle that can efficiently encapsulate nucleic acids of a variety of sizes. LNPs leverage endogenous lipid trafficking pathways for effective intracellular delivery.[57] Advances in synthetic lipid design as well as screening of multiple particle structures have enabled siRNA and mRNA delivery at clinically relevant concentrations. LNP formulations are used in multiple FDA approved therapeutics where siRNA is the active drug.[8]

LNPs are typically multicomponent nanoparticles formed through an ethanol emulsion method, wherein multiple lipid and sterol components are dissolved in ethanol and the nucleic acids to be encapsulated are dissolved in a low pH buffer.[84] Following, the aqueous buffer solution of nucleic acids is rapidly mixed with the hydrophobic materials dissolved in ethanol at a fixed volume ratio. Here, the low pH buffer causes a lipid to become positively charged, driving efficient encapsulation of the nucleic acids.

The LNP core is typically comprised of four classes of components: a sterol, a phospholipid, a lipid-PEG, and an ionizable lipid. A sterol, which fits in gaps between lipids and increases their melting temperature, stabilizes the nanoparticles and may promote fusion of the LNP with compartments inside the cell.[85,86] The phospholipid component supports the structure and may aid endosomal escape and alter the tissue targeting of the LNP.[87,88] Lipid-PEGs coat the nanoparticle surface due to their amphiphilic nature and prevent nanoparticle clearance and aggregation.[89] The fourth component of the lipid nanoparticle, the ionizable lipid has been the subject of great inquiry. Ionizable lipids are used to both drive encapsulation of the nucleic acids as well as assist the nanoparticle in escaping from cell compartments.[90–92] Keys to finding an

effective ionizable structure have been screening many different structures,[92] assessing how the pKa of structures affects potency,[91] and using both natural and unnatural lipid head group structures for targeting.[93]

1.4.2 *High-throughput screening methods to optimize nanoparticle structures*

With many different possible LNP structures comprised of four or more components, screening methods are necessary to determine relationships between structures and activity in the desired application. Statistical methods to reduce the number of screening experiments needed to find the main effects of each factor and the first-order interactions are often useful. Design of Experiment (DoE) methodologies such as definitive screening designs and fractional factorials are useful methods to reduce the number of screening experiments to first find the parameters of a library which are significant and then expand to find their main effects and interactions.[94] Kauffmann et al demonstrate that DoE can be used to optimize a LNP structure designed to silence Factor VII expression in the liver of mice.[16] The DoE-based optimization process led to faster screening of hit nanoparticle structures as well as insight into the significant parameters. The study found that key parts of the optimal formulation were the phospholipid used and the ionizable lipid:mRNA mass ratio.

1.4.3 *Evaluating lipid nanoparticles in vivo in high throughput*

While cellular assays can be engineered for higher throughput evaluation of nanoparticle structures using fluorescence or luminescence measurements, *in vivo* evaluation of many different nanoparticles simultaneously is necessary to evaluate how nanoparticles behave after systemic administration. Methods using fluorescence measurements have been used to benchmark activity of one nanoparticle or a pool of nanoparticles at a time. Constituently expressing GFP mice can be used to evaluate LNPs carrying siGFP.[95] Mice expressing

fluorophores downstream from floxed STOP sites can be used to evaluate function of Cre mRNA respectively using fluorescence turn-on.[15]

Some promising techniques for evaluating nanoparticles' distribution and function in high throughput combine a function readout with multiplexed detection of each nanoparticle. DNA barcoded nanoparticles use DNA sequences for multiplexed detection of a pool of nanoparticles injected into one mouse.[96] LNPs are made separately containing DNA sequences with identical universal primer sites and different 8 nucleotide DNA barcode near the center. After isolating cell types that are potential targets for the LNP using FACS, the DNA is sequenced and the relative amount of each nanoparticle in each cell type can be calculated. When this method is combined with a functional readout like one of the aforementioned fluorescence-based methods, function and distribution can be read out in a multiplexed fashion.[93,95] These methods have allowed researchers to screen over 100 nanoparticles simultaneously in mice for functional RNA delivery.[93]

1.4.4 *mRNA delivery and genome editing using lipid nanoparticles*

mRNA delivery enables a plethora of therapeutic LNP delivery that were not previously conceived using shorter DNA and RNA sequences. As mRNA sequences, theoretically, may code for any protein's sequence, mRNA delivery may replace mutated genes, replace missing genes, and express genome and base editors within cells. LNPs have been explored for all of these purposes using mRNA delivery. Proof-of-concept experiments show that LNPs can be used to replace knocked out enzymes in mouse models.[97,98] LNPs with encapsulated mRNA coding for a Cas enzyme and a single guide RNA sequence (sgRNA) have been used to demonstrate genome editing capability.[15,99] Many genetic diseases are caused by one incorrect base in the sequence of a gene. In this case, delivery of mRNA coding for a base editor is a useful and safe

option for treatment. Musunuru et al demonstrate long-lasting and safe base editing of the gene PCSK9 in non-human primates, which causes a lasting decrease in LDL cholesterol.[100] These data exemplify the promise of delivering LNPs containing base editors as a one-shot curative therapy for genetic diseases.

1.4.5 *Note on the importance of targeted delivery of mRNA*

One of the primary safety concerns of *in vivo* genome and base editing is its off-target effects in other organs, cells, and parts of the genome that are not intended. Base editors, for example, have shown high degrees of off target effects in the RNA and DNA of cells in which they act.[12,13,101] Much of the off-target effects in the genome and transcriptome are consequence of the editor enzyme and guide RNA sequence. With nanocarriers, however, approaches to decrease effects in off-target cells and organs are possible with mRNA delivery. In contrast to delivering the base editor and guide RNA ribonucleoprotein complex, delivery of mRNA coding for a genome editing enzyme is safer due to the more transient exposure to the enzyme.[14] Recently, researchers have identified LNP structures with tissue-specific tropism due to the addition of a charged lipid, termed a SORT lipid, to existing formulations (Figure 1.7).[15] The authors demonstrate that the tissue-specific tropism of the mRNA expression they observe is also specific when using Cas9 mRNA and sgRNA. While further work is required to determine the mechanism of tissue-specific mRNA delivery, genome editing specific to cells in one organ is an important step to easing safety concerns with these medicines.

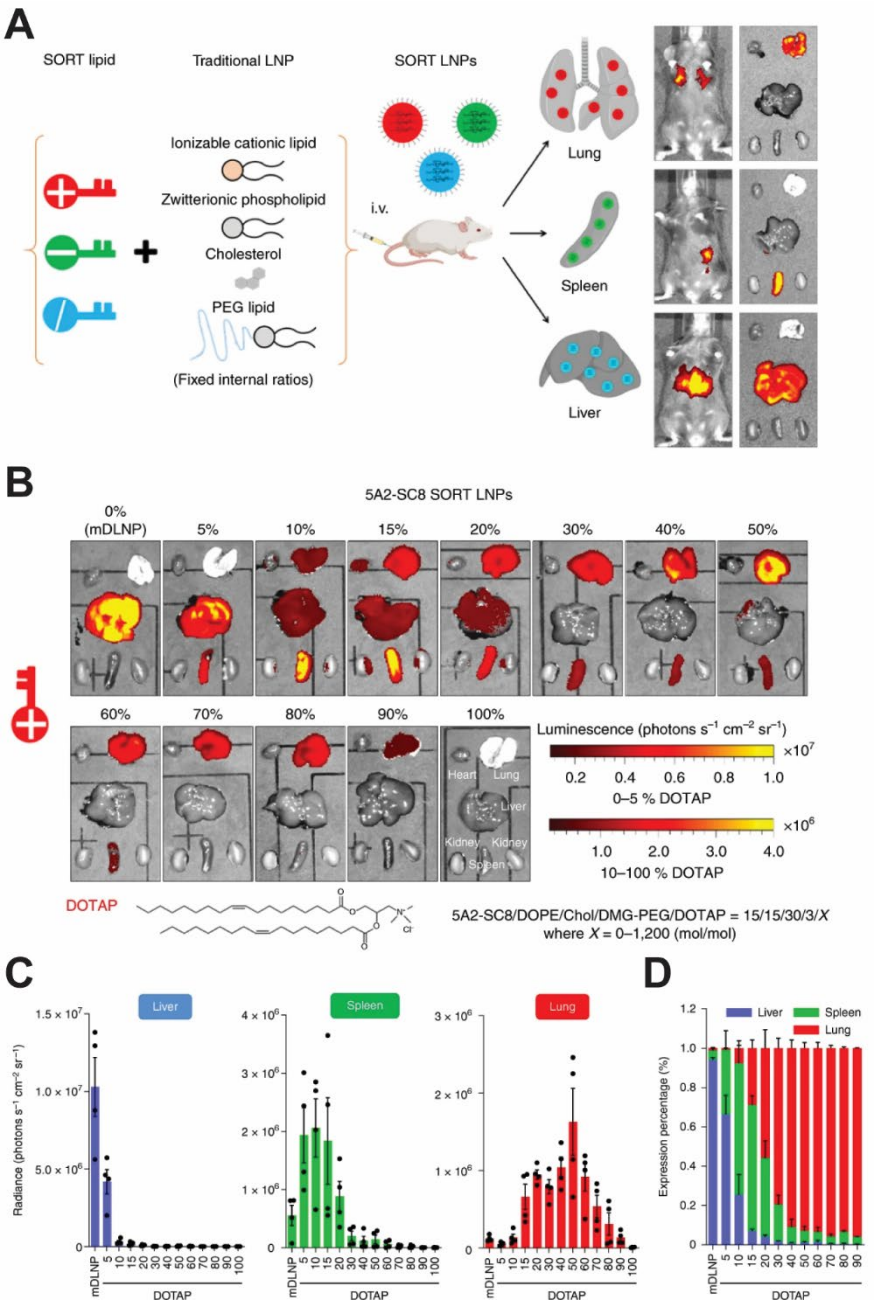

Figure 1.7 *SORT nanoparticle strategy used to target mRNA expression from LNPs to specific organs.* (A) Additional components (SORT molecules) added to existing LNP formulations change tissue tropism using luciferase mRNA expression as a model system. (B) Liver to spleen to lung shift of luciferase mRNA expression in LNPs as a function of percent DOTAP SORT

lipid added. (C) Shift in quantity of luciferase expression graphed as percentage of SORT lipid. (D) Expression of luciferase expressed as a relative percentage between liver, spleen, and lung. Copyright 2020, the authors of ref[15], under exclusive license to Springer Nature Limited.

1.5 Introduction to dissertation topics

1.5.1 *Structure-dependent biodistribution of liposomal spherical nucleic acids*

Liposome-based SNA structures are a more modular and degradable version of the AuSNAs that were the first constructs tested in mice. Following the advent of the approach of using hydrophobic modifications to DNA sequences to form SNAs on liposomal templates, Meckes et al observed that the release rate of oligos from the liposome core can be tuned by changing the hydrophobicity of the anchor.[48] While this anchor chemistry affects cellular internalization and activity in cellular assays, it is important to determine stability's impact on delivery *in vivo*. In chapter two, we evaluated the structure-dependence of distribution of two LSNA constructs, one using DNA with a cholesterol anchor and another using a more hydrophobic diacyl lipid anchor. In wild-type mice, we administer the constructs systemically and evaluate the distribution of both the liposome core of the SNA and the DNA independently. This analysis is performed on three different levels: whole tissues, tissue sections, and individual cell populations. This multi-organ analysis into the distribution of LSNA structures is one of the most detailed looks into how modular SNA structures can be tuned for delivery to particular organs and cells.

1.5.3 *Lipid nanoparticle spherical nucleic acids for intracellular DNA and RNA delivery*

In chapter two, we demonstrate that lipid-based SNA structures can be tuned for enhanced DNA delivery to target organs. The LSNA structure has been used therapeutically for modulating the immune system,[47] as a vaccine,[82,102] and as a gene regulating agent.[45] However,

the LSNA structure suffers from two major limitations. First, the oligonucleotides to be delivered must be amenable to a hydrophobic modification in order to be functionalized to the surface of the liposome. Second, liposomes which are comprised of only one lipid do not contain any components which significantly augment the escape of the oligonucleotides from cell compartments. This increases the concentration needed to achieve therapeutic effect. As mentioned in chapter 1.6, lipid nanoparticles present an opportunity to encapsulate many different nucleic acid structures as well as achieve effective cytosolic delivery. In chapter three, a strategy used to combine the delivery advantages of SNAs with the function of LNPs is presented. Lipid nanoparticle SNAs (LNP-SNAs) are optimized using a DoE-based methodology in order to best incorporate DNA modifications to LNPs. Following, the effectiveness of DNA-mediated LNP targeting is demonstrated in wild-type mice. In addition, the sequence-dependence of this effect is explored by comparing and contrasting Poly(T) and G-rich LNP-SNA structures.

1.5.1 *Lipid nanoparticle spherical nucleic acids for intracellular DNA and RNA delivery*

In chapter three, we investigated an approach to use DNA to target LNPs in mice by forming LNP-SNAs. While we observed some organ-specific mRNA expression in G-rich LNP-SNAs, the cause of this effect was still to be determined. The work of many other groups has ascertained that cells of the mononuclear phagocyte system (MPS), mainly present in the liver and spleen, determine the clearance of most nanoparticles.[28,103] While mRNA expression was not observed in the liver by G-Rich LNP-SNAs, we sought to evaluate which cells in the liver and spleen were sequestering this nanoparticles. Using multiplexed DNA barcoding, multiple structures were pooled together to evaluate the effects of LNP-SNA structure on distribution. In chapter three, we demonstrated that LNP-SNA structures could be used to target mRNA

expression to the spleen. However, this effect was not quantified on a cell population level. In this chapter, we will analyze the mRNA expression levels of LNPs and the equivalent LNP-SNAs in individual cell populations in the spleen and liver

CHAPTER TWO

2 LIPOSOMAL SPHERICAL NUCLEIC ACIDS WITH TUNABLE BIODISTRIBUTION

Portions of this chapter reprinted (adapted) with permission from: Ferrer, J. R.*; **Sinegra, A. J.***; Ivancic, D.; Yeap, X. Y.; Qiu, L.; Wang, J. J.; Zhang, Z. J.; Wertheim, J. A.; Mirkin, C. A. *ACS Nano* **2020**, *14* (2), 1682–1693. Copyright 2020, American Chemical Society.
* = equal contribution

2.1 Summary

Spherical nucleic acids (SNAs) are a class of nanomaterials with a structure defined by a radial distribution of densely packed, short DNA or RNA sequences around a nanoparticle core. This structure allows SNAs to rapidly enter mammalian cells, protects the displayed oligonucleotides from nuclease degradation, and enables co-delivery of other drug cargoes. Here, we investigate the biodistribution of liposomal spherical nucleic acid (LSNA) conjugates, SNA architectures formed from liposome templates and DNA modified with hydrophobic end groups (tails). We compared linear DNA with two types of LSNAs that differ only by the affinity of the modified DNA sequence for the liposome template. We use single-stranded DNA (ssDNA) terminated with either a low-affinity cholesterol tail (CHOL-LSNA) or a high-affinity diacylglycerol lipid tail (DPPE-LSNA). Both LSNA formulations, independent of DNA conjugation, reduce the inflammatory cytokine response to intravenously administered DNA. The difference in the affinity for the liposome template significantly affects DNA biodistribution. DNA from CHOL-LSNAs accumulates in greater amounts in the lungs than DNA from DPPE-LSNAs. In contrast, DNA from DPPE-LSNAs exhibits greater accumulation in the kidneys. Flow cytometry and fluorescence microscopy of tissue sections indicate that different cell populations — immune and non-immune — sequester the DNA depending upon the chemical makeup of the LSNA. Taken together, these data suggest that the chemical structure of the LSNAs represents an opportunity to direct the biodistribution of nucleic acids to major tissues outside of the liver.

2.2 Introduction

Nucleic acid therapeutics have tremendous potential, but their widespread use has been limited largely due to challenges with effective delivery. Delivery of unmodified, linear

oligonucleotides results in rapid clearance, nuclease-mediated degradation, and poor internalization by cells.[104–106] Spherical Nucleic Acids (SNAs) are a class of nucleic acids comprised of a dense shell of radially-oriented oligonucleotides surrounding a nanoparticle core. This architecture allows SNAs to overcome many of the limitations associated with delivery of linear oligonucleotides. SNA architectures rapidly enter over 50 different cell types,[52,65] resist nuclease degradation,[54,107] and transcytose across different biological barriers, including the skin,[108] blood-brain barrier, and blood-tumor barrier.[109,110]

There are a number of factors, such as nanoparticle size, shape, and surface charge, which affect the bioavailability of systemically administered nanomedicines.[111–113] This includes their interaction with serum proteins, mechanism of cellular entry, and clearance from the body.[114] Previously, we determined that gold-based SNAs (Au SNAs) primarily distribute to the liver and spleen with minor changes due to varying the presented DNA sequence or backfilling the SNA surface with PEG.[63,109] This follows the pattern of many nanoparticles,[115–122] which are cleared by the cells of the mononuclear phagocyte system (MPS) located primarily in organs such as the liver, spleen, and bone marrow.[31,123] Because the Au SNAs are not extensively used clinically,[124] we sought to explore the more modular and clinically relevant liposomal LSNA [125–127] in order to exploit structural changes to direct DNA biodistribution.

The highly modular LSNA architecture enables modification of both the nanoparticle core and surface chemistry. With LSNA architectures, the affinity of the DNA shell to the liposome template can be modified to control overall nanostructure stability and the release rate of oligonucleotides from the liposome core. For example, increasing the hydrophobicity of the 3' tail of the DNA sequence by changing it from a cholesterol group to a C16 diacyl lipid anchor

(DPPE)[128–130] increases the affinity of the DNA shell for the liposome template. In serum-containing media, this modification increases the half-life of DNA attachment to the LSNA's lipid bilayer by greater than 20-fold.[131] This increased stability leads to greater cellular uptake and potency with respect to innate immune receptor stimulation.[81,131,132] These observations highlight how LSNA stability may dictate interactions with immune cell populations *in vivo* as well as the tissues and cell populations to which the LSNAs distribute. To determine these *in vivo* structure-function relationships, we synthesized LSNAs with either cholesterol- or lipid-anchored DNA and measured the immune response, tissue distribution, and cellular level distribution of each LSNA construct in immune-competent mice. The results highlight the advantages of LSNA architectures over linear DNA and the importance of LSNA stability in tuning the delivery of systemically administered oligonucleotides to target difficult-to-reach tissues.

2.3 Results and Discussion

2.3.1 Synthesis and characterization of dual fluorophore-labeled LSNAs.

The biodistribution profiles of intravenously injected LSNAs were studied in healthy, *wild-type* C57Bl/6 mice using a Cyanine 5 (Cy5) fluorophore-labeled, phosphorothioate backbone single-stranded DNA (ssDNA) sequence. Liposomes onto which the DNA was functionalized were labeled with 10% TAMRA-PC (**Table 1.1**, **Table 1.2**).

Table 2.1 DNA Sequences used in each formulation

Formulation	**DNA Sequence (5'-3')**
Linear DNA	TCC ATG AGC TTC CTG AGC TT Cy5[a] (spacer 18)[b] (spacer 18)[b]
CHOL-LSNA	TCC ATG AGC TTC CTG AGC TT Cy5[a] (spacer 18)[b] (spacer 18)[b] - Cholesterol TEG[c]
DPPE-LSNA	TCC ATG AGC TTC CTG AGC TT Cy5[a] (spacer 18)[b] (spacer 18)[b] - DBCO dT[d]

[a] Cy5 = 1-[3-(4-monomethoxytrityloxy)propyl]-1'-[3-[(2-cyanoethyl)-(N,N-diisopropylphosphoramidityl]propyl]-3,3,3',3'-tetramethylindodicarbocyanine chloride phosphoramidite
[b] Spacer 18 = 18-O-Dimethoxytritylhexaethyleneglycol,1-[(2-cyanoethyl)-(N,N-diisopropyl)]- phosphoramidite
[c] Cholesterol TEG = 1-Dimethoxytrityloxy-3-O-(N-cholesteryl-3-aminopropyl)-triethyleneglycol-glyceryl-2-O-succinoyl-long chain alkylamino-CPG
[d]DBCO-dT = 5'-Dimethoxytrityl-5-[(6-oxo-6-(dibenzo[b,f]azacyclooct-4-yn-1-yl)-capramido-N-hex-6-yl)-3-acrylimido]-2'-deoxyUridine,3'-[(2-cyanoethyl)-(N,N-diisopropyl)]-phosphoramidite

Table 2.2 LSNA formulations used in each condition

Sample Name	**Liposome Composition**	**DNA Sequence**
Mix	100% DOPC	5'-ODN 2138[a]-(Spacer 18) (Spacer 18)-3'
CHOL-LSNA	100% DOPC	5'-ODN 2138[a]-(Spacer 18) (Spacer 18)-Cholesterol TEG-3'
DPPE-LSNA	95% DOPC, 5% Azidocaproyl-PE	5'-ODN 2138[a]-(Spacer 18) (Spacer 18)-DBCO dT-3'

[a]ODN 2138 = 5'-TCC ATG AGC TTC CTG AGC TT-3'

The DNA used to synthesize cholesterol-tail LSNAs (CHOL-LSNAs) was terminated with cholesterol, while the DNA used to synthesize DPPE-tail LSNAs (DPPE-LSNAs) was terminated with a dibenzocyclooctyne-modified thymidine nucleobase (DBCO-dT) (Figure 2.1A). The sequence used was ODN 2138, a sequence designed as a GpC non-immunogenic control to the CpG-containing TLR9 agonist, ODN 1826.[133,134] LSNAs were synthesized by first forming a 50 nm diameter small unilamellar vesicle (SUV) template comprised of 100% 1,2-dioleyl-*sn*-glycero-3-phosphocholine (DOPC). For DPPE LSNAs, DOPC SUVs were modified with 5% (mol/mol) azide-capped 1,2-dipalmitoyl-*sn*-glycero-3-phosphoethanolamine (DPPE-Azide) (Figure 2.1B). Following SUV formation, DNA sequences and liposome templates were mixed and shaken overnight at room temperature in 20 mM HEPES-buffered saline. This facilitated cholesterol-terminated DNA insertion into the SUV bilayer, forming CHOL-LSNAs, as well as the copper-free click reaction of DBCO-terminated DNA with DPPE-Azide lipids on the SUV surface, forming DPPE-LSNAs. The liposome size and spherical architecture were confirmed using dynamic light scattering and TEM (Figure 2.2, Figure 2.3). Using UV-VIS

spectroscopy to measure DNA concentration and ICP-OES to quantify phosphorus content, we determined the number of DNA strands per LSNA. The mixing ratio of cholesterol-tailed DNA to lipids that results in the maximum number of DNA strands per liposome was determined to be approximately 15.4 μM DNA to 1 mM lipids (Figure 2.4). The DNA loading into each respective formulation is comparable at this reaction stoichiometry, as the average number of strands per liposome was 123 ± 28 for the CHOL-LSNA and 96 ± 18 for the DPPE-LSNA. As a control, we used a mixture (Mix) of linear DNA with no hydrophobic tail (Table 2.1, Table 2.2) with the same number of liposomes, such that the Mix contains the same ssDNA sequence, but cannot form LSNAs.

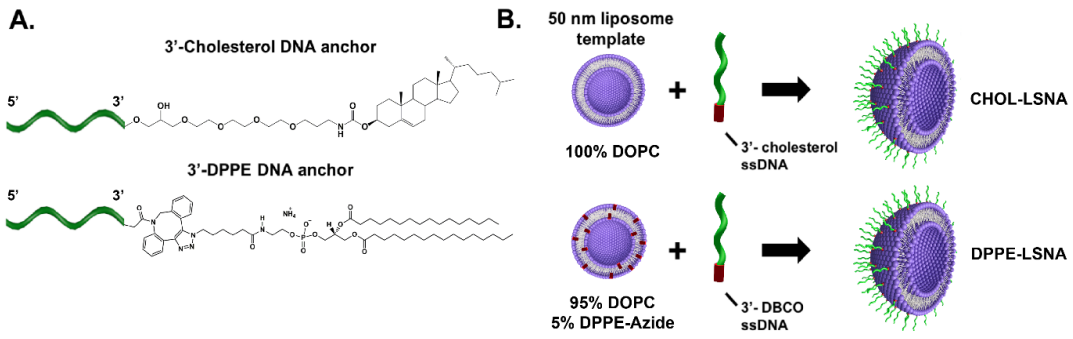

Figure 2.1 *Oligonucleotide components used to synthesize each LSNA.* (A) Structures of 3' DNA tails that anchor DNA to each liposome template. (B) Each DNA sequence is reacted with either 50 nm liposomes comprised of (top) 100% DOPC or (bottom) 95% DOPC/5% DPPE-Azide (mol/mol) to form each respective LSNA.

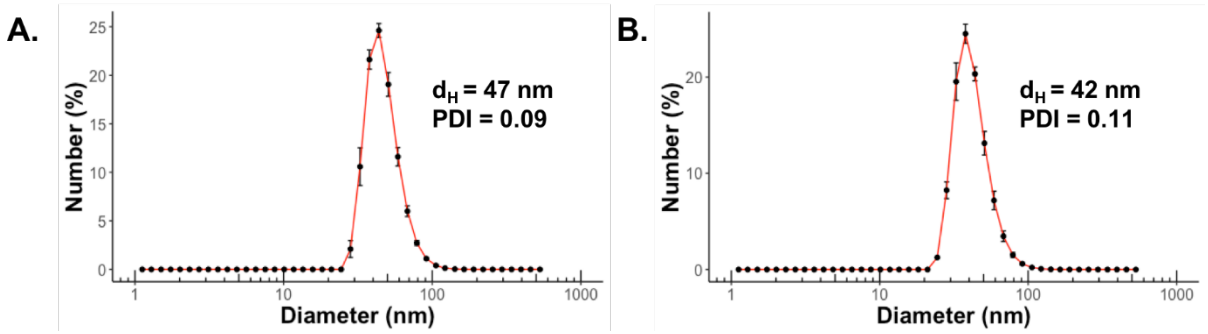

Figure 2.2 *Distribution of liposome template sizes as measured by DLS.* **(**A) Cholesterol-tail LSNA template, (B) Lipid-tail LSNA template. Error bars represent standard error between DLS measurements (N = 5).

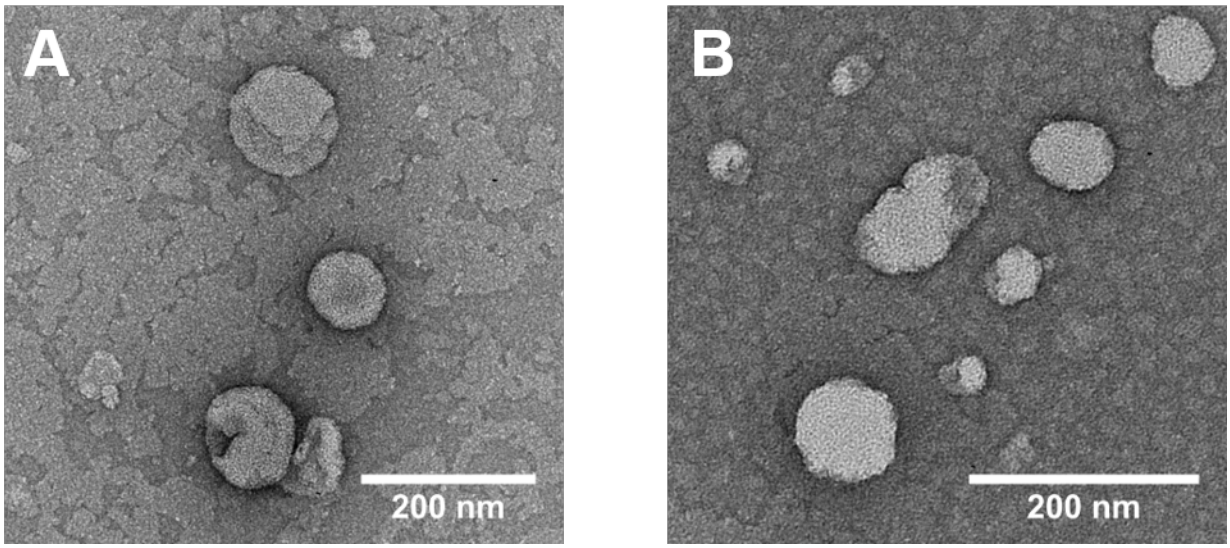

Figure 2.3 *TEM Images of LSNAs.* LSNAs were negative stained with 2% uranyl acetate and imaged on TEM grids comprised of a carbon film on a 300 mesh copper grid. TEM images of (A) CHOL-LSNAs and (B) DPPE-LSNAs.

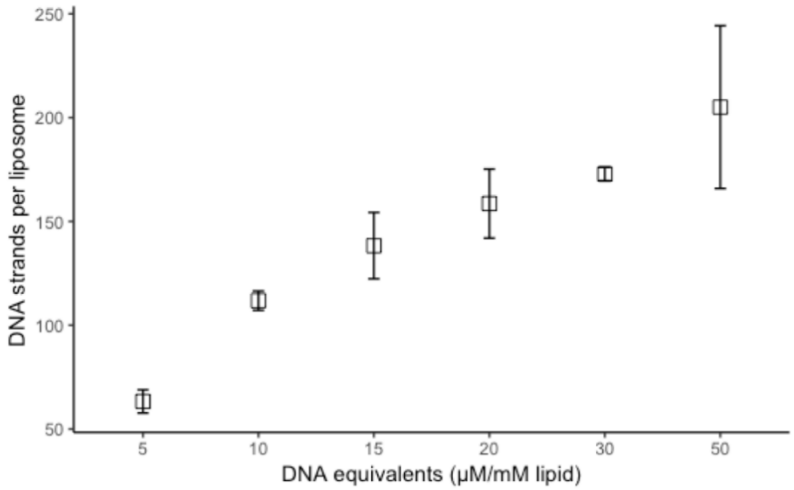

Figure 2.4 *Loading of Cholesterol-tail DNA into 50 nm DOPC liposomes***.** Cholesterol-tail DNA strands per liposome were assessed as a function of the number of DNA equivalents reacted with the liposome template. After mixing cholesterol-tail DNA with the liposome template overnight at room temperature, LSNAs were purified from free DNA using a Sepharose CL-4B column. DNA was quantified by dissociating each liposome in 0.1% sodium dodecyl sulfate and measuring the 260 nm absorbance of DNA. Total phosphorus content was assessed using ICP-OES. Error bars represent standard error, N = 3.

2.3.2 LSNAs elicit a reduced cytokine response compared to equivalent linear DNA sequences.

Systemically administered linear oligonucleotides often lead to off-target effects, such as non-specific cytokine production and stimulation of inflammatory pathways.[135–137] To quantify the difference between linear DNA and LSNA structures in this context, we measured the production of various cytokines in the serum after intravenous administration of LSNAs into

C57/Bl6 mice. At 30 minutes post injection, linear DNA increased production of the pro-inflammatory cytokine MCP-1 by 2.46-fold over CHOL-LSNAs and 1.80-fold over DPPE-LSNAs. Linear DNA also induced IFNγ production when it was not detected in LSNA treated mice (Figure 2.2A). This suggested a more severe acute inflammatory response to linear DNA than for the equivalent dose of LSNAs. IL-6 and TNF production were also increased in linear DNA treated mice compared to LSNA formulations, but changes were not statistically significant. Enhanced production of anti-inflammatory cytokine IL-10 was also observed in response to linear DNA compared to untreated mice (Figure 2.2A).

By 24 hours, most cytokines produced in response to linear DNA and LSNAs returned to basal levels, with IL-6 and TNF not detected. The only exception was MCP-1, which showed elevated levels due to linear DNA, 2.39-fold enhancement over CHOL-LSNAs and 2.71-fold over DPPE-LSNAs (Figure 2.5B). These changes in cytokine levels suggest that the LSNA architectures studied herein are inherently less inflammatory than linear DNA *in vivo,* an observation we previously described *in vitro.*[138] Because the inflammatory cytokines MCP-1 and IFNγ are known to recruit and activate cells of the MPS,[139,140] the difference in production of these cytokines in response to each form of DNA (linear or LSNA) is likely linked to differences in trafficking and sequestration of each of these architectures after injection.

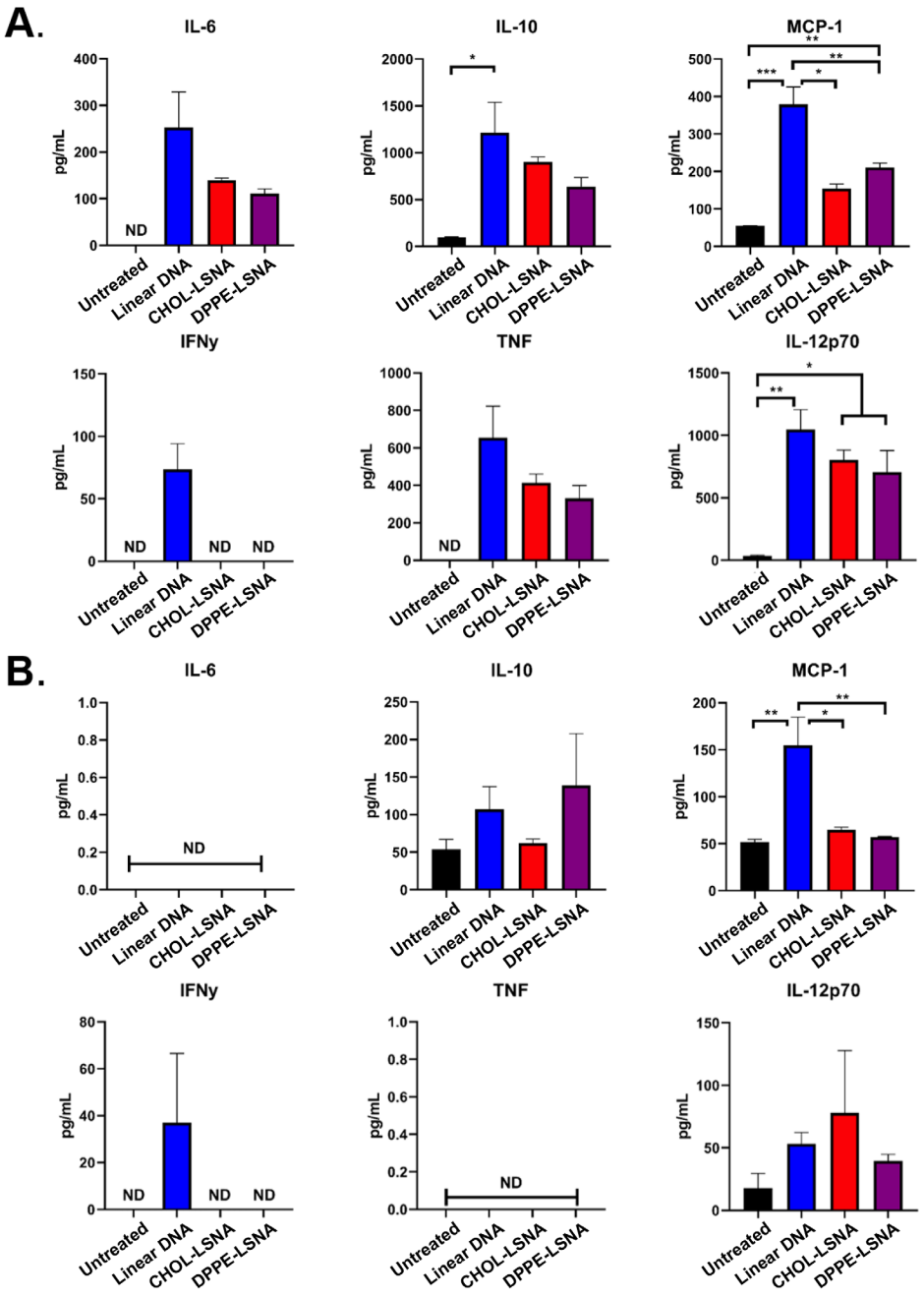

Figure 2.5 *Effect of linear oligonucleotides and LSNAs on cytokine production.* Cytokines were measured following intravenous administration of linear DNA, CHOL-LSNAs, or DPPE-LSNAs at (A) 30 minutes and (B) 24 hours post injection in C57/Bl6 mice. (ND = not detectable;

Statistical significance was calculated by one-way ANOVA with Tukey's post hoc test *P<0.05, **P<0.01, ***P<0.005, error bars represent standard error, N=3).

2.3.3 Organ level distribution of LSNAs is structure dependent.

To evaluate the tissue level distribution of administered DNA, mice received a peripheral intravenous (IV) injection of either LSNA structure or a control mixture (Mix) of the same amount of Cy5-DNA and TAMRA-PC labeled liposomes (Table 2.2). After 30 minutes or 24 hours of circulation, organs were recovered and analyzed. Using the spectral unmixing function on the IVIS instrument, fluorescence of the 10% TAMRA-PC liposomes was separated from that of the Cy5-tagged DNA. When comparing all organs at 30 minutes, the greatest fluorescence from both DNA and the liposome cores of LSNAs came from the liver, kidneys, and spleen (Figure 2.6A, Figure 2.7, Figure 2.8, Figure 2.9). However, when each organ was imaged separately, more significant differences were apparent. For most organs examined, except the small intestine and pancreas, DNA derived from either the CHOL-LSNA or DPPE-LSNA had greater tissue accumulation relative to linear DNA. In the liver and serum, twice as much DNA fluorescence was observed with LSNA-treated mice than linear DNA. The LSNA core fluorescence was at a comparable ratio, with both LSNAs exhibiting 1.5 to 2-fold enhancement in the liver and greater than 50-fold enhancement in the serum. There was a skewing towards CHOL-LSNA trafficking to the lungs and lymph nodes, where we observed five-fold and three-fold increased Cy5-DNA fluorescence compared to linear DNA (Figure 2.6B, Figure 2.8). Compared to DPPE-LSNAs, DNA from CHOL-LSNAs accumulated in the lungs by greater than two-fold. The liposome core fluorescence was also 2-fold greater with CHOL-LSNAs, which suggested that the cholesterol-DNA may not be released from the liposome core before lung

accumulation (Figure 2.6B). In contrast, DNA from DPPE-LSNAs trafficked in greater amounts to the heart, brain, and kidneys (Figure 2.6B, Figure 2.8, Figure 2.10). Most notably, DPPE-LSNAs exhibit nearly 2-fold enhanced Cy5-DNA fluorescence in the kidneys compared to the Mix and CHOL-LSNAs, but show no TAMRA fluorescence enhancement (Figure 2.6B, Figure 2.9). This suggests that the enhanced kidney delivery may be due to DNA dissociation from DPPE-LSNAs prior to kidney accumulation.

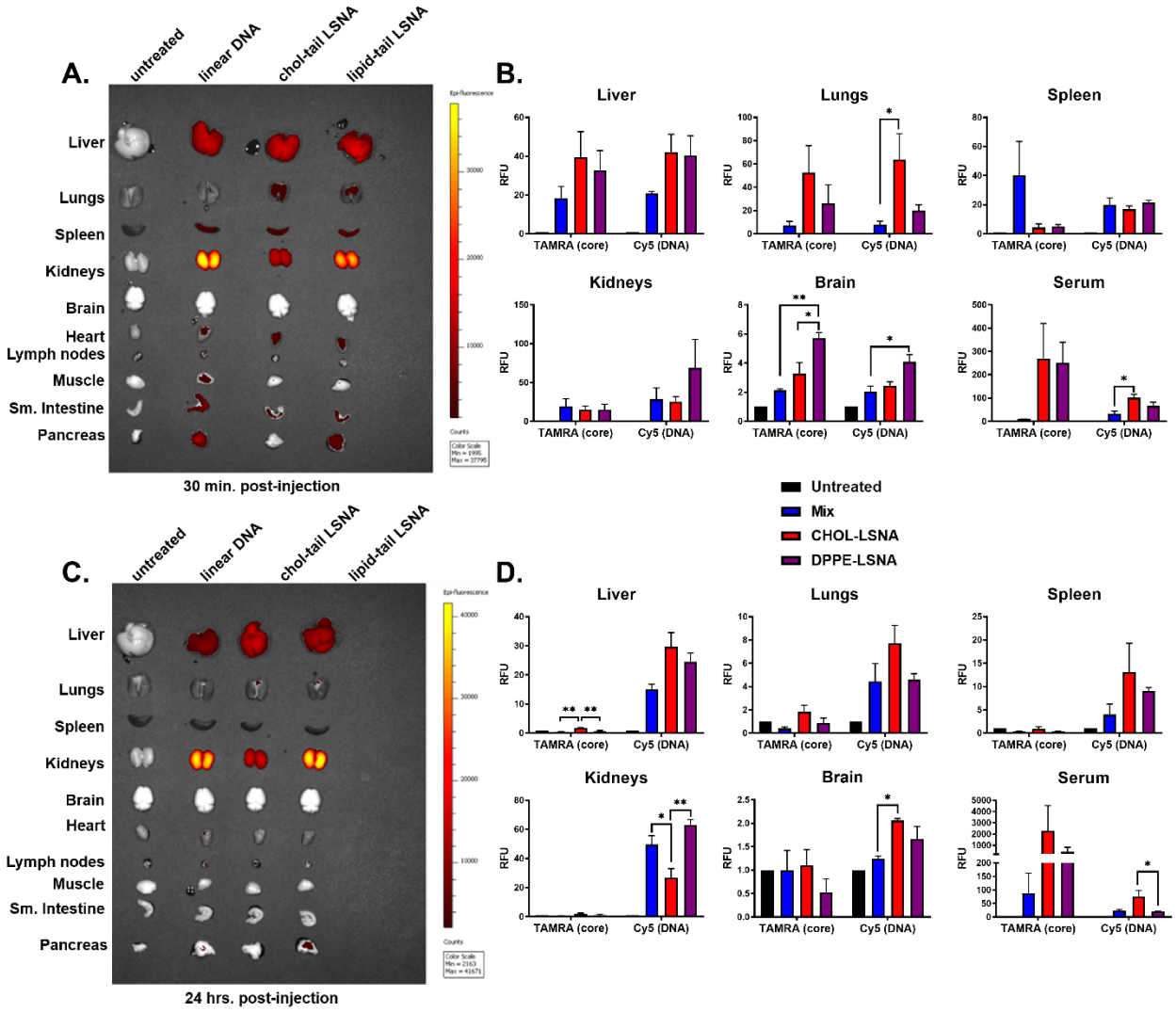

Figure 2.6 *Whole organ analysis of DNA trafficking.* Following IV injection of LSNAs, organs were harvested at (A, B) 30 minutes and (C, D) 24 hours and imaged *ex vivo*. TAMRA-PC (liposome) and Cy5 (DNA) fluorescence were separated using the spectral unmixing function of the IVIS instrument. Relative tissue level distribution normalized to untreated mice was assessed by imaging all organs simultaneously (A, C). Individual organs were imaged, and the relative fluorescence was calculated at (B) 30 minutes and (D) 24 hours. (N = 3-5; Statistical significance

was calculated by one-way ANOVA with Tukey's post hoc test. *P<0.05, **P<0.01, error bars represent standard error).

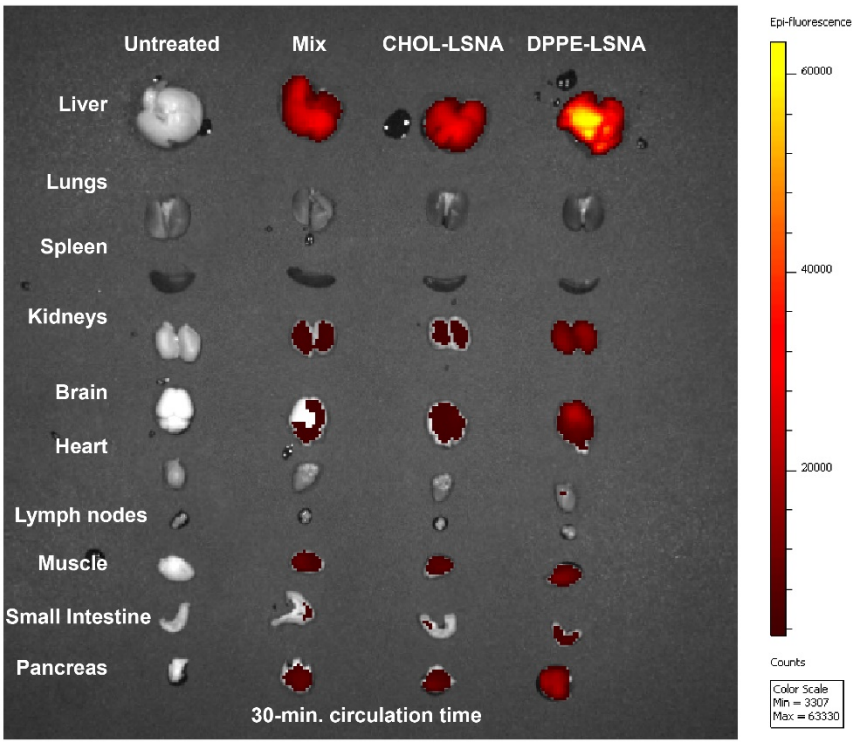

Figure 2.7 *Distribution of TAMRA-labeled liposomes after 30-min. circulation time*. Scale reports fluorescence from each organ in photons/s.

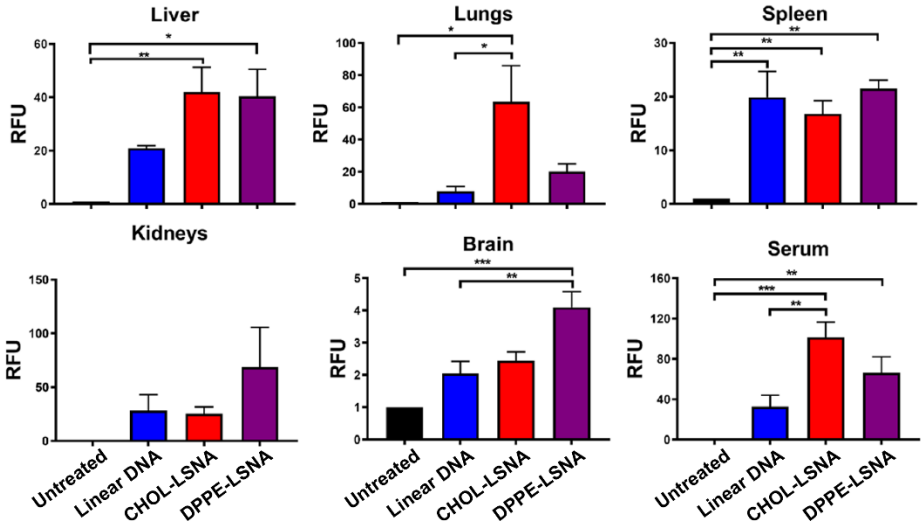

Figure 2.8 *Cy5 DNA distribution after 30 min circulation time.* Individual organs were imaged using an *in vivo* imaging system (IVIS), and the relative fluorescence was calculated compared to untreated animals (statistical significance was calculated by one-way ANOVA with Tukey's *post hoc* test *P<0.05, **P<0.01, ***P<0.005, error bars represent standard error).

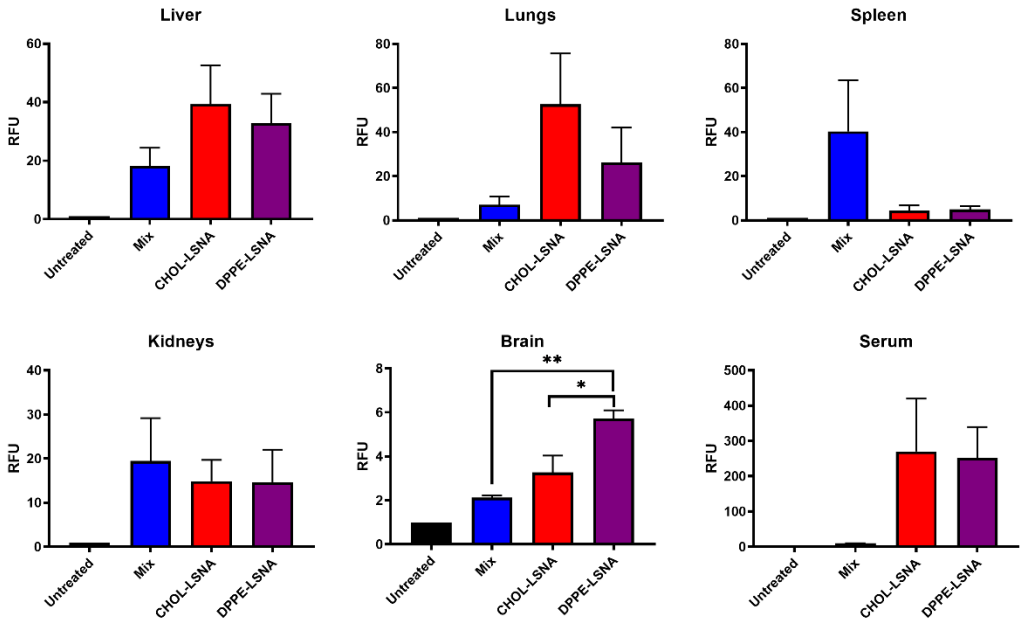

Figure 2.9 *TAMRA-labeled liposome distribution after 30 min circulation time.* Individual organs were imaged using an *in vivo* imaging system (IVIS), and the relative fluorescence was calculated compared to untreated animals (statistical significance was calculated by one-way ANOVA with Tukey's *post hoc* test *P<0.05, **P<0.01, error bars represent standard error).

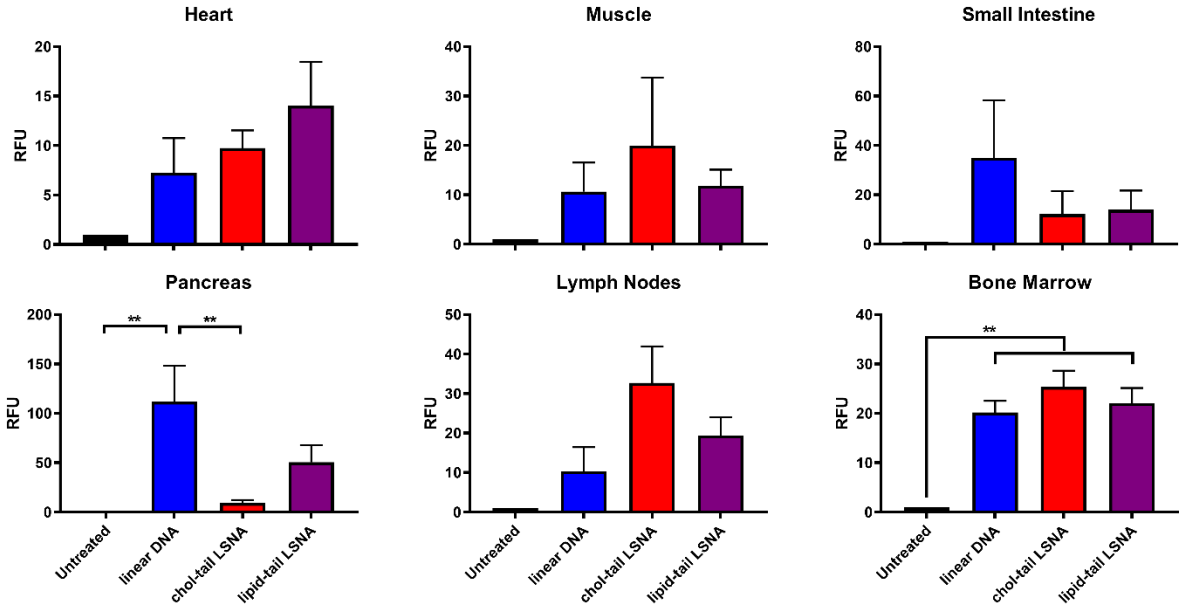

Figure 2.10 *IVIS analysis of Cy5 DNA distribution in major organs 30 min post injection.* Individual organs were imaged using an in vivo imaging system (IVIS), and the relative fluorescence was calculated compared to untreated animals (statistical significance was calculated by one-way ANOVA with Tukey's post hoc test *P<0.05, **P<0.01, error bars represent standard error).

Similarly, at 24 hours, the liver and kidneys exhibited the overall highest DNA accumulation (Figure 2.6C, Figure 2.11). Both LSNAs exhibited higher liposome core fluorescence than the Mix in the serum but had little Cy5-DNA fluorescence at this timepoint. The highest serum DNA signal was from CHOL-LSNAs (Figure 2.6D). In the liver, both LSNAs continued to show higher Cy5 fluorescence compared to linear DNA (Figure 2.6D). Cy5-DNA fluorescence from CHOL-LSNAs remained higher than linear and DPPE-LSNAs in the lungs

and lymph nodes (Figure 2.6D, Figure 2.13), and also had the highest accumulation in the brain and bone marrow. CHOL-LSNA-treated mice exhibited the highest TAMRA liposome fluorescence in the liver and lungs at this timepoint (Figure 2.6D, Figure 2.12). DPPE-LSNAs continued to deliver the most DNA to the kidneys, with nearly 3-fold Cy5 fluorescence relative to CHOL-LSNAs (Figure 2.6D, Figure 2.11). Akin to the 30-minute timepoint, there was little TAMRA-PC fluorescence in the kidneys from DPPE-LSNAs, suggesting Cy5-DNA release before accumulation. Linear DNA accumulation, which was higher in the pancreas and small intestine at 30 minutes (Figure 2.10), was not significantly different from either LSNA in these organs at 24 hours (Figure 2.11).

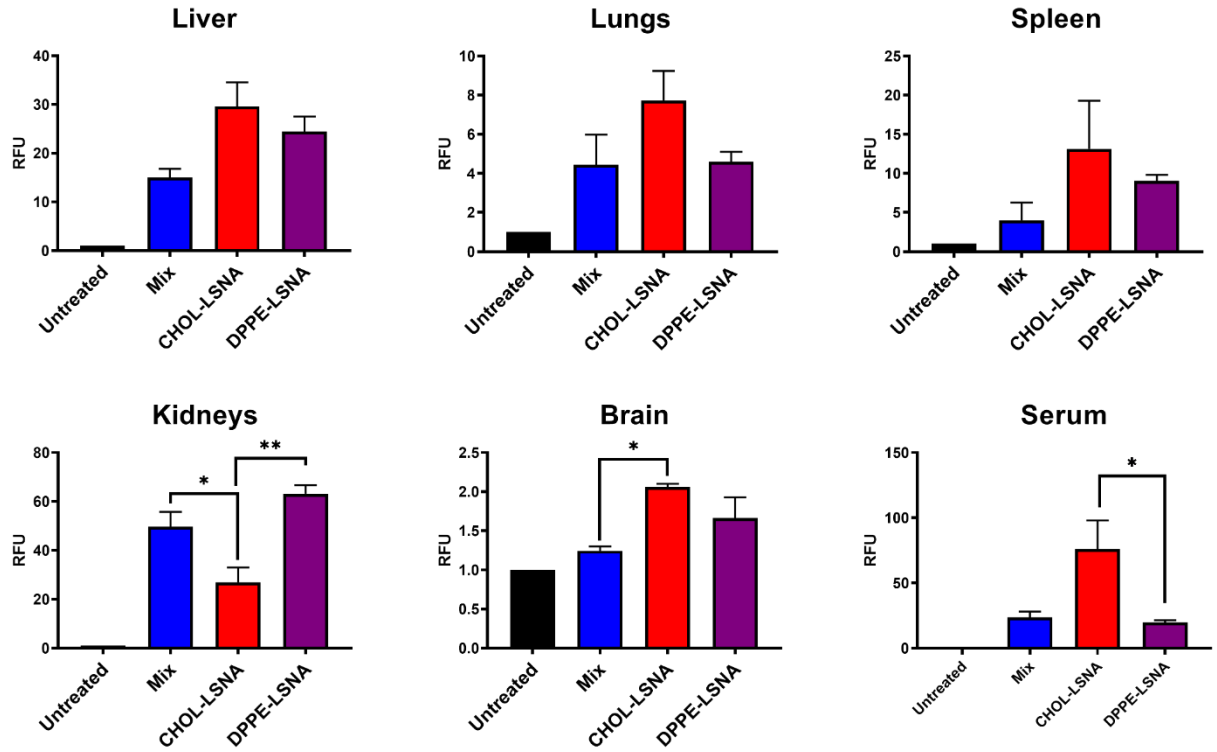

Figure 2.11 *Cy5 DNA distribution after 24 h circulation time.* Individual organs were imaged using an *in vivo* imaging system (IVIS), and the relative fluorescence was calculated compared

to untreated animals (statistical significance was calculated by one-way ANOVA with Tukey's *post hoc* test *P<0.05, **P<0.01, error bars represent standard error, N = 3-5).

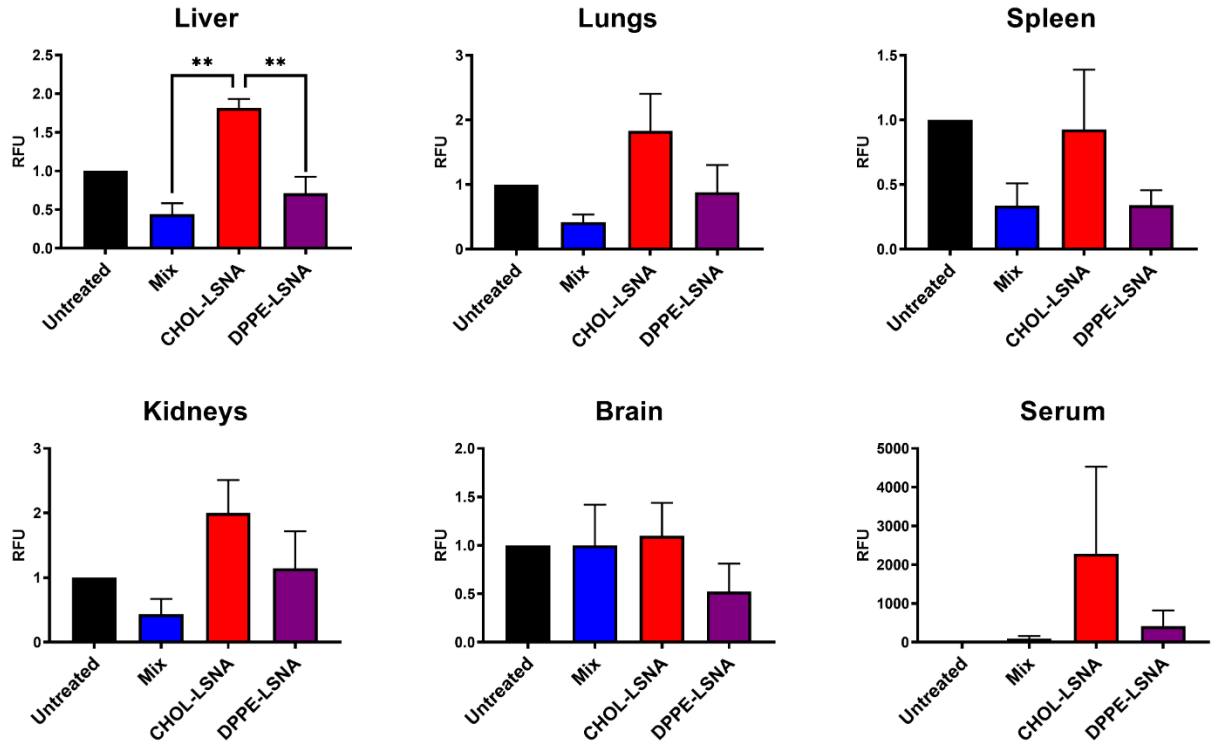

Figure 2.12 *TAMRA-labeled liposome distribution after 24 h circulation time.* Individual organs were imaged using an *in vivo* imaging system (IVIS), and the relative fluorescence was calculated compared to untreated animals (statistical significance was calculated by one-way ANOVA with Tukey's *post hoc* test **P<0.01, error bars represent standard error N = 3-5).

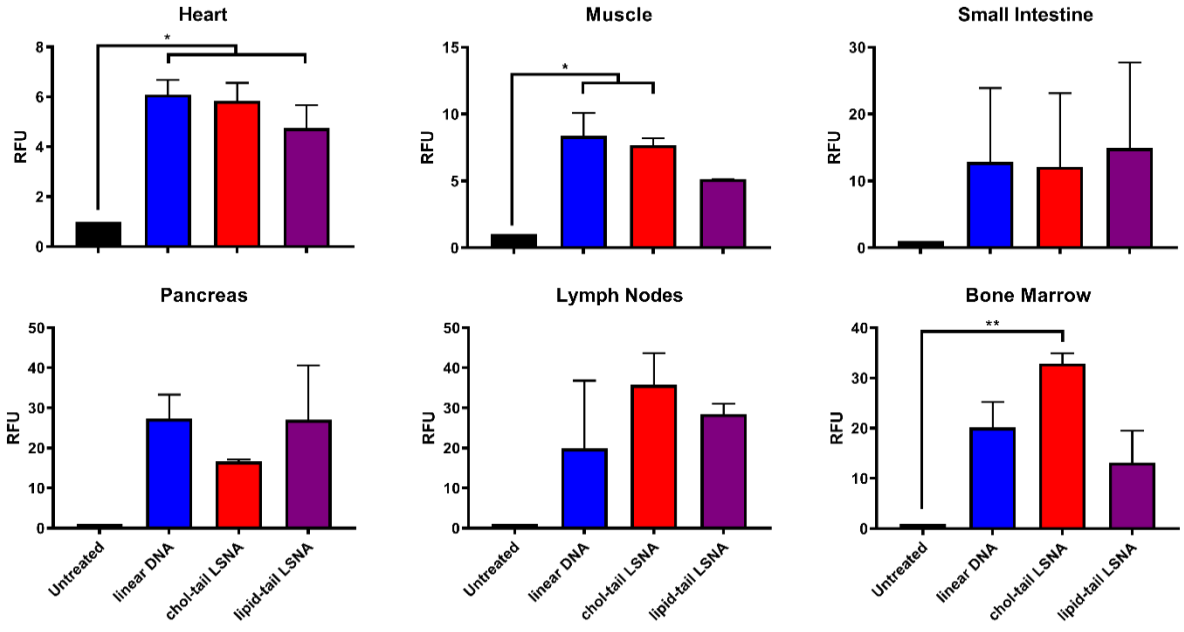

Figure 2.13 *IVIS analysis of Cy5-DNA distribution in other major organs 24 hrs. post injection.* Individual organs were imaged using an in vivo imaging system (IVIS), and the relative fluorescence was calculated compared to untreated animals (statistical significance was calculated by one-way ANOVA with Tukey's post hoc test *P<0.05, **P<0.01, error bars represent standard error, N = 3-5) .

To further probe tissue-level distribution and the colocalization of both labeled LSNA components, we imaged cryosectioned tissues from mice injected with both dual fluorophore-labeled LSNAs and the Mix control. In agreement with the IVIS data, livers from animals treated with either LSNA had greater levels of Cy5 fluorescence at both time points (Figure 2.18A, E). Although LSNAs accumulate in the liver in greater total amounts, the location of linear DNA

and both LSNAs appears similar within our organ sections (Figure 2.18A, E, and Figure 2.14), suggesting that DNA from LSNAs and linear DNA may be sequestered by similar cell types. This was confirmed by flow cytometry (Figure 2.20A). For the lungs, the highest fluorescence was observed in the case of the CHOL-LSNA, both at 30 minutes (Figure 2.18B) and 24 hours (Figure 2.18F), also consistent with IVIS imaging (Figure 2.6B, D).

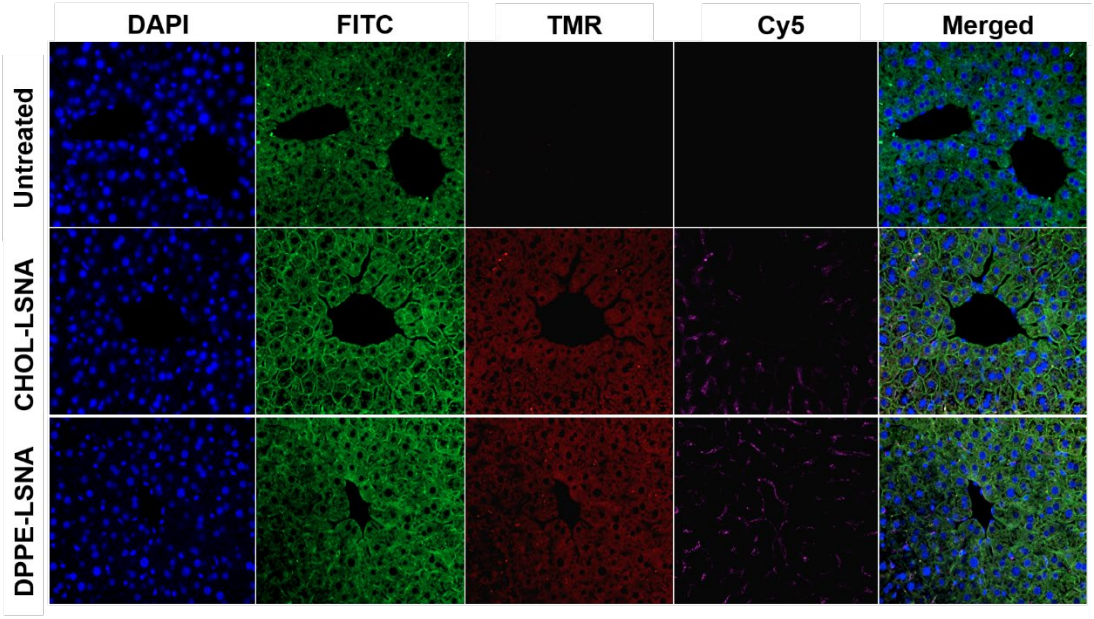

Figure 2.14 *TAMRA (TMR)-PC liposomes and Cy5-DNA within liver cryosections.* The distribution of Cy5-labeled DNA and TAMRA-labeled liposomes 30 minutes post injection (blue = DAPI (nuclear stain), green = phalloidin (actin filament stain), red = TMR (TAMRA-PC), magenta = Cy5-DNA, taken at 40X magnification).

While IVIS imaging of whole organs cannot distinguish the location of both fluorophore-labeled components within tissues, cryosections indicated that the liposome and DNA of CHOL-LSNAs were colocalized within lung tissue (Figure 2.15). This confirmed that the cholesterol-tail DNA

is not released from CHOL-LSNAs before lung accumulation. The spleen showed a high level of linear DNA accumulation in what appears to be a blood vessel at 30 minutes (Figure 2.18C). In contrast, the spleens from LSNA-treated animals exhibited more evenly distributed fluorescence throughout the organ (Figure 2.18C, Figure 2.15).

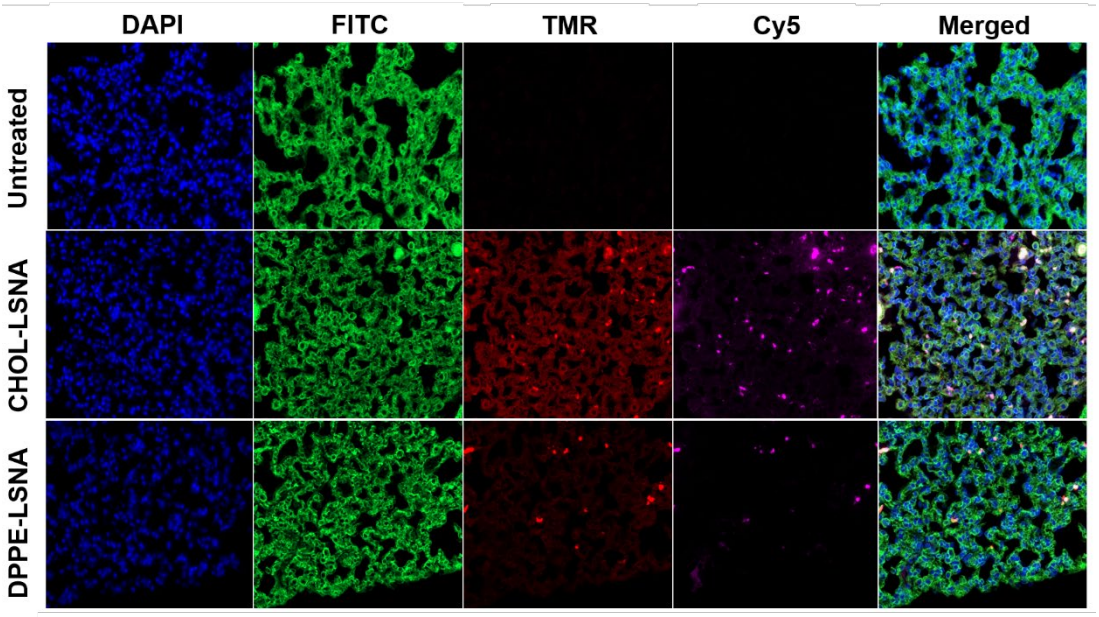

Figure 2.15 *TAMRA (TMR)-PC liposomes and Cy5-DNA within lung cryosections.* The distribution of Cy5-labeled DNA and TAMRA-labeled liposomes 30 minutes post injection (blue = DAPI (nuclear stain), green = phalloidin (actin filament stain), red = TMR (TAMRA-PC), magenta = Cy5-DNA, taken at 40X magnification).

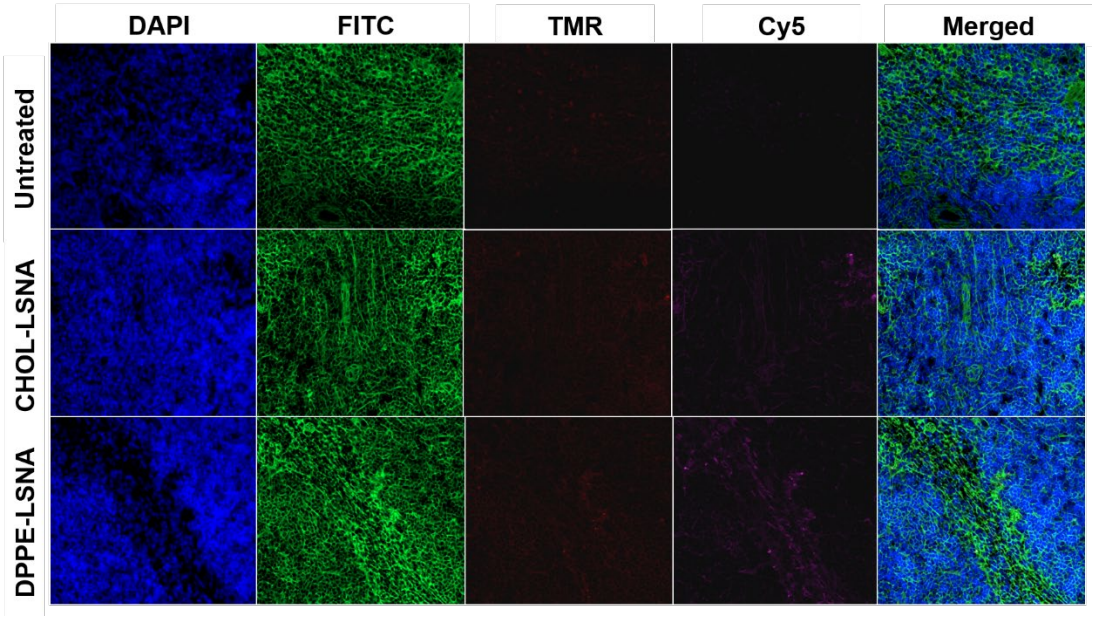

Figure 2.16 *TAMRA (TMR)-PC liposomes and Cy5-DNA within spleen cryosections.* The distribution of Cy5-labeled DNA and TAMRA-labeled liposomes 30 minutes post injection (blue = DAPI (nuclear stain), green = phalloidin (actin filament stain), red = TMR (TAMRA-PC), magenta = Cy5-DNA, taken at 40X magnification).

At 24 hours, this evenly distributed fluorescence signal remained in the spleens from animals treated with DPPE-LSNAs and was not observed in spleens from animals treated with linear DNA (Figure 2.18G). The tubules of the kidney showed very high Cy5 signals for both linear DNA- and DPPE-LSNA-treated animals compared to animals treated with CHOL-LSNAs, 30 minutes (Figure 2.18D) and 24 hours (Figure 2.18H) post injection, consistent with the IVIS data. While it is not surprising that linear DNA is observed in the tubules, accumulation of DNA from DPPE-LSNAs in these structures was surprising. The 50 nm diameter of the DPPE-LSNAs is large compared to glomerular capillary pores, the largest of which have radii of approximately 80 Å.[26,27] Thus, DPPE-LSNAs cannot be filtered if the LSNA is intact. We hypothesize that

DNA derived from DPPE-LSNAs dissociates from the liposome template in the glomerulus, leaving lipid-tail DNA alone to pass through the glomerular fenestrations. To confirm that the DNA was released, we checked for colocalization of the liposomes and DNA of DPPE-LSNAs in the cryosections. We observed high Cy5-DNA signal in the kidneys, but little TAMRA fluorescence above the untreated background, suggesting that the DNA must have been released from DPPE-LSNAs prior to accumulation within the tubules (Figure 2.16).

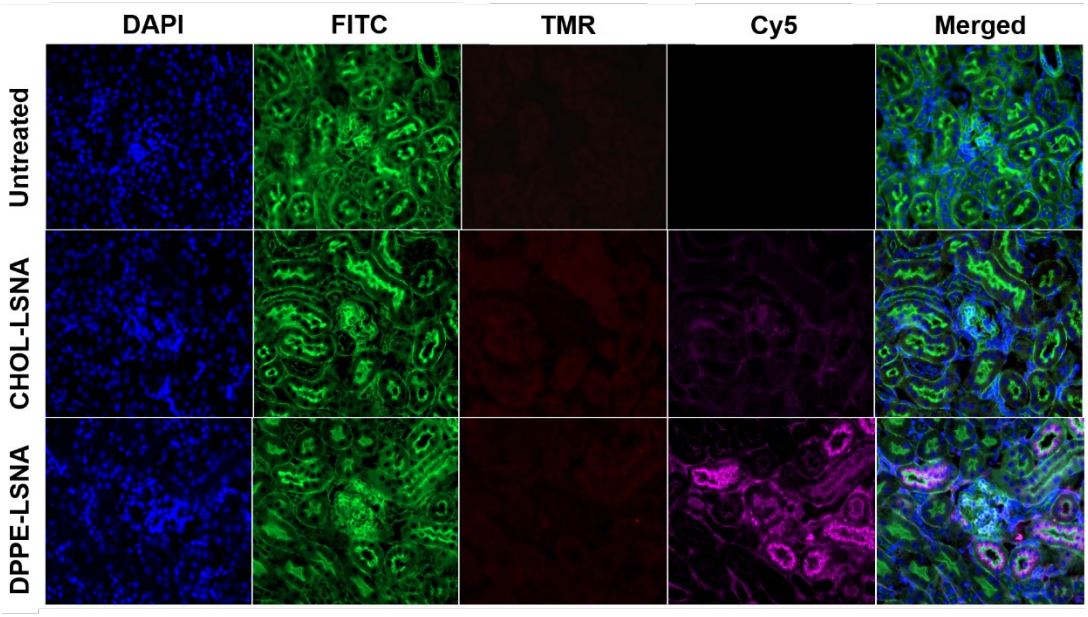

Figure 2.17 *TAMRA (TMR)-PC liposomes and Cy5-DNA within kidney cryosections*. The distribution of Cy5-labeled DNA and TAMRA-labeled liposomes 30 minutes post injection (blue = DAPI (nuclear stain), green = phalloidin (actin filament stain), red = TMR (TAMRA-PC), magenta = Cy5-DNA, taken at 40X magnification).

This is a finding specific to LSNAs, as significant accumulation of other SNAs in the kidneys has not been previously observed. We reported previously that Au SNAs exhibit the greatest

accumulation in the liver and spleen[109] with very little accumulation in the kidneys. In contrast, LSNAs exhibited greatest DNA accumulation in four different organs: the liver, lungs, spleen, and kidneys. This suggests that the more dynamic nature of LSNAs compared to Au SNAs may play a role in their *in vivo* bioavailability. We also observed DNA trafficking from LSNAs in small intestines, lymph nodes, and pancreas, suggesting that there may be other possible tissue targets for future LSNA therapeutic development (Figure 2.9, Figure 2.10).

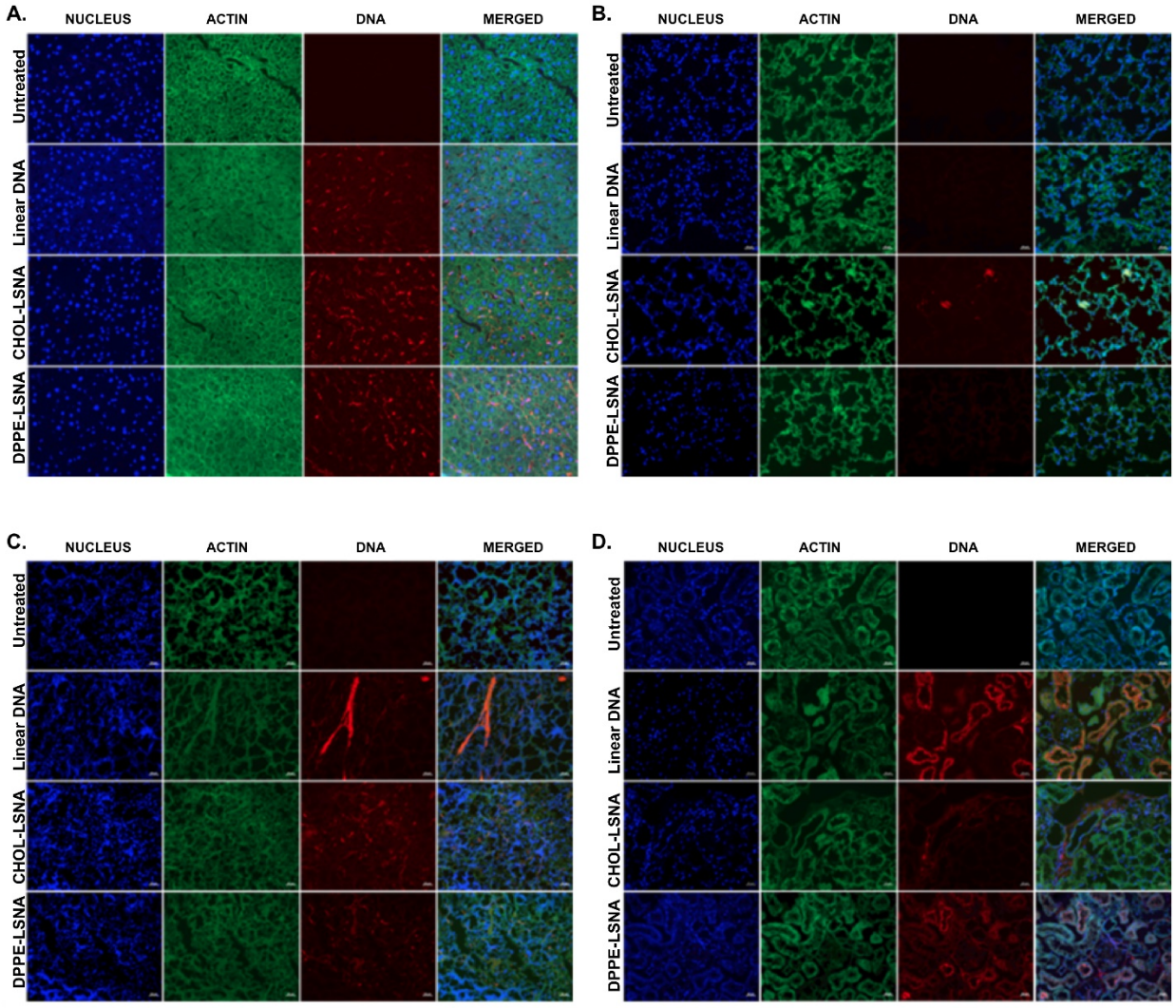

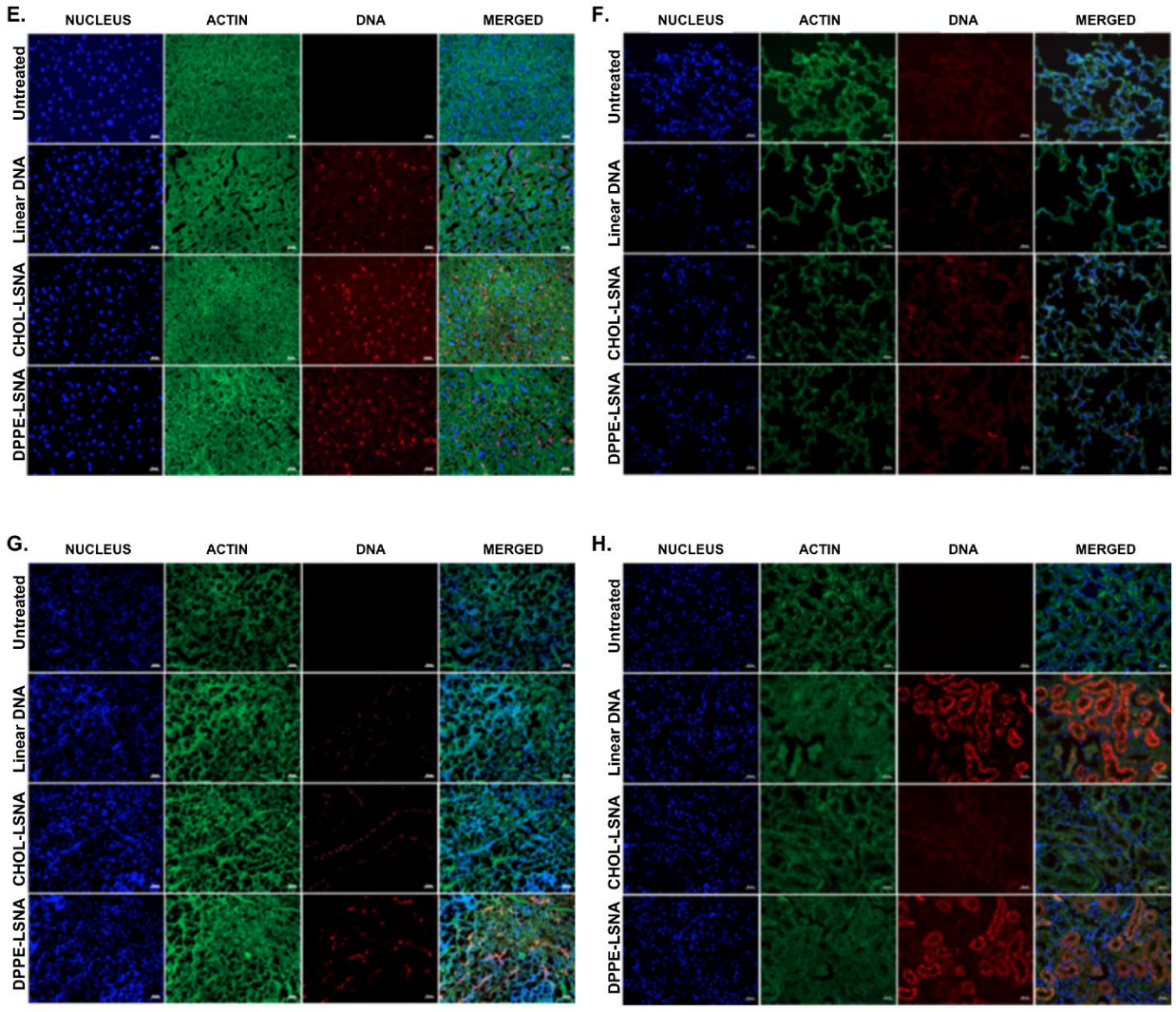

Figure 2.18 *Distribution of Cy5-labeled DNA within tissues.* The distribution of Cy5-labeled linear DNA, CHOL-LSNAs, and DPPE-LSNAs in the liver, lungs, spleen, and kidneys at (A-D) 30 minutes and (E-H) 24 hours post injection. (blue = DAPI (nuclear stain), green = phalloidin (actin filament stain), red = Cy5-DNA, taken at 40X magnification, scale bar = 20 μm).

2.3.4 LSNA architecture and DNA attachment chemistry alter cellular trafficking of DNA within major organs.

After examining macroscopic differences in DNA distribution between each architecture using IVIS and fluorescence microscopy, we determined structure-distribution relationships on

the cell population level. We developed two flow cytometry panels, one for staining immune cells and another for non-immune cells, which would capture the majority of cell types present in each organ. Within the immune cell panel, single cell suspensions derived from each organ were stained for a general immune cell marker (CD45), T cells (CD3), B Cells (CD19), neutrophils (CD11b), dendritic cells (CD11c), and macrophages (CD68). The non-immune cell panel included the general immune cell marker (CD45), to exclude those cells that stained positively, as well as markers for epithelial cells (EPCAM), endothelial cells (CD31), fibroblasts (CD140a), and blood-derived stem cells (CD34). The general gating strategy used is depicted in Figure 2.19.

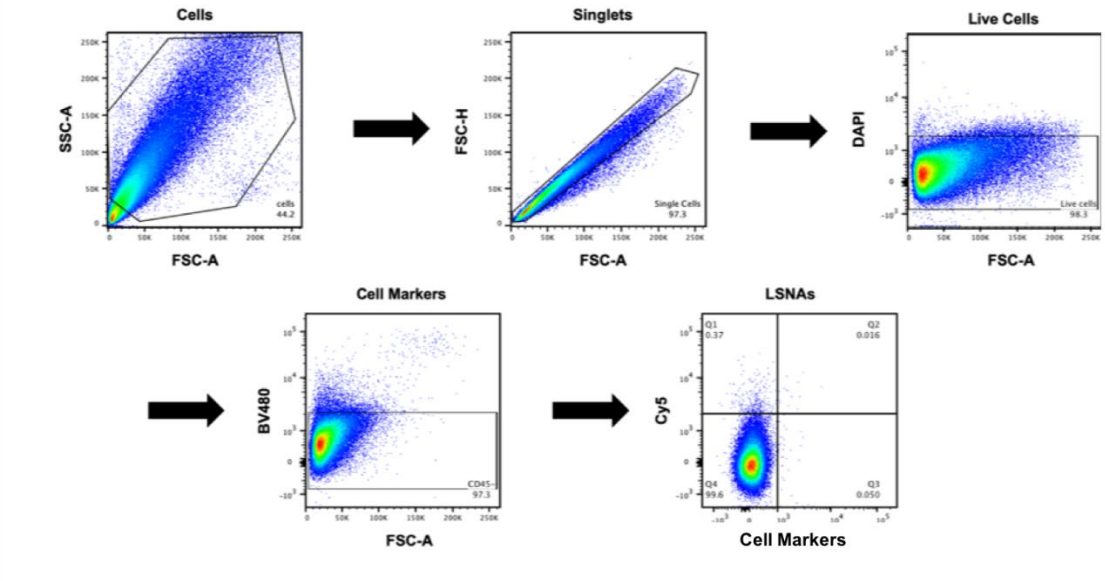

Figure 2.19 *Gating strategy for flow cytometry data.* The above gating strategy was used to assess the cellular level distribution of DNA in different tissues. Single-cell suspensions from processed tissues were gated for single cells, live cells, classes of cell markers (immune or non-immune using CD45), and then individual cell markers. Following this, we report the percent of

each cell type positive for each cell marker can be assessed as well as the median fluorescence intensity of the cell type positive for DNA.

At the 30-minute time point (after injection of labeled linear DNA or LSNA), there was very little difference between groups in the total number of cells from the liver (Figure 2.20A), spleen (Figure 2.20C), and kidneys (Figure 2.20D) that tested positive for the Cy5-DNA. However, an investigation of specific cell types within the spleen and kidneys revealed differences in the total amount of DNA being delivered to cells by each respective construct. In the spleen, there was a trend for higher accumulation of DNA from the DPPE-LSNA in the non-immune cells, particularly in epithelial cells (Figure 2.20C), and higher accumulation of DNA from CHOL-LSNA in CD11b+ immune cells. The kidney showed higher linear DNA accumulation in non-immune cells, but no difference between groups in immune cells. This was an expected outcome because the count of total immune cells (CD45+ cells) in the kidney was very low (< 1% of cell counts). The most significant difference at 30 minutes for total Cy5 positive cells was observed in the lungs (Figure 2.20B), where CHOL-LSNAs showed the highest DNA accumulation, which is consistent with IVIS and fluorescence imaging results. In particular, DNA from CHOL-LSNAs was preferentially trafficked to the non-immune cells of the lungs, and there was no significant difference between CHOL- and DPPE-LSNAs in immune cells, though the total DNA fluorescence from both LSNAs in immune cells was higher than linear DNA.

At the later time point, the trend for total Cy5 accumulation in each organ remained the same, with the liver, spleen, and kidney showing no significant difference between groups and the lungs showing higher CHOL-LSNA delivery. However, there were differences in the total

DNA in specific cell types. In the liver at 24 hours (Figure 2.20E), both CHOL- and DPPE-LSNAs exhibited higher fluorescence in non-immune cells, which suggested that LSNA architecture is responsible for enhanced DNA delivery to the liver. Noticeably, in the immune cells within the liver, CHOL-LSNAs showed higher delivery to T cells, but all three treatments were less distinguishable in B cells, neutrophils, dendritic cells, and macrophages. In the spleen (Figure 2.20G), the same trend was observed in non-immune cells as at 30 minutes. In contrast, immune cells sequestered DNA from DPPE-LSNAs in greater amounts in CD11b+ cells than DNA from CHOL-LSNAs. A slight preference of CHOL-LSNA DNA trafficking to CD11c+ and CD68+ cells at 24 hours was also observed. In the kidney (Figure 2.20H), there was a dramatic reduction in the trafficking or accumulation of DNA from CHOL-LSNAs in all non-immune and CD19+ immune cells. Whereas linear DNA showed the highest accumulation at 30 minutes, DPPE-LSNAs exhibited the highest fluorescence intensities from most cell types at 24 hours. Specifically, fibroblasts, epithelial cells, and T cells showed very high lipid-tail association. Finally, in the lungs (Figure 2.20F), CHOL-LSNAs exhibited higher Cy5 fluorescence intensity than linear DNA in all cell types, with a preference for the trafficking of DNA from CHOL-LSNAs to immune cells.

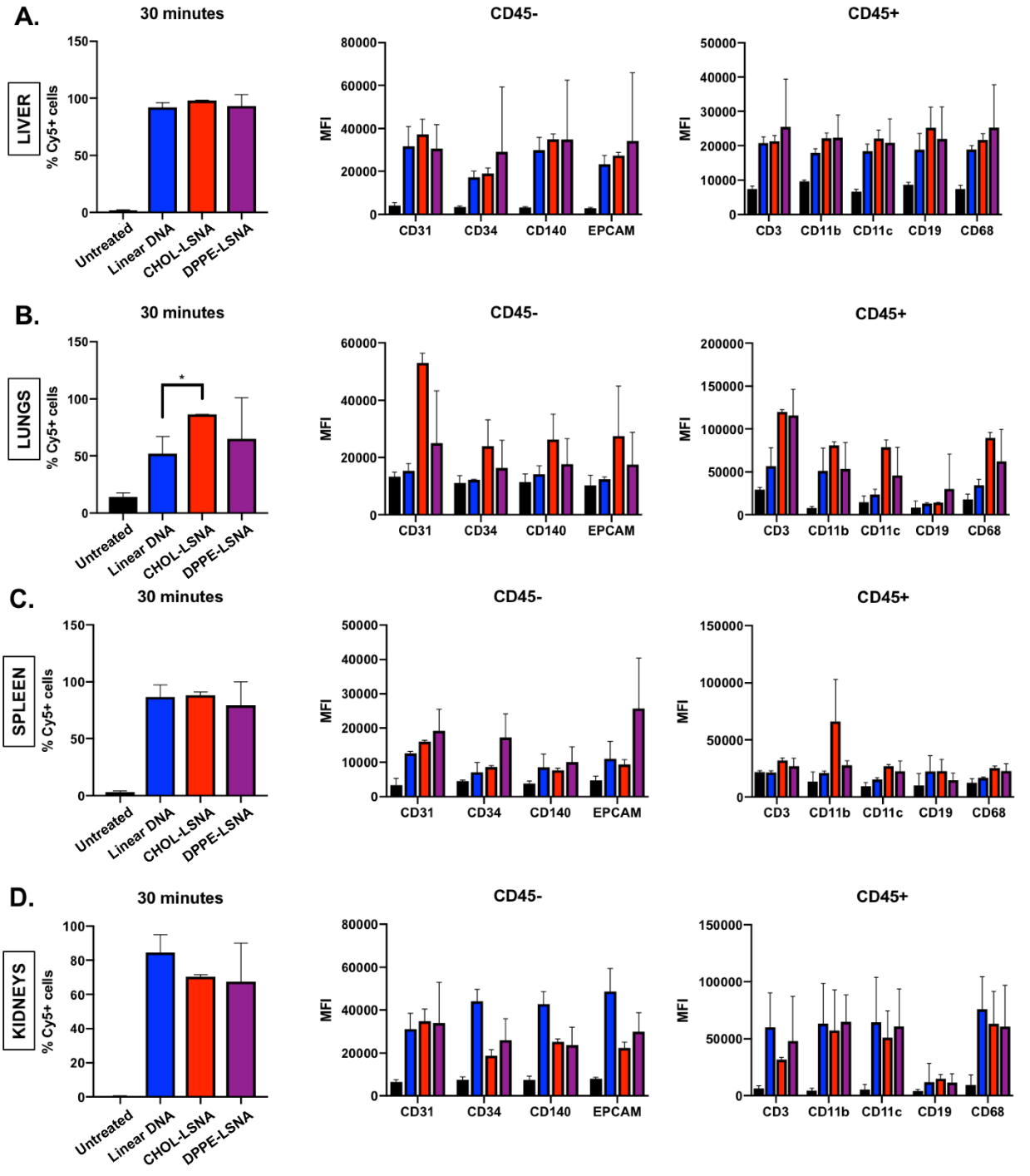
A.
30 minutes
LIVER
% Cy5+ cells
Untreated
Linear DNA
CHOL-LSNA
DPPE-LSNA
CD45-
MFI
CD31
CD34
CD140
EPCAM
CD45+
CD3
CD11b
CD11c
CD19
CD68
B.
LUNGS
C.
SPLEEN
D.
KIDNEYS

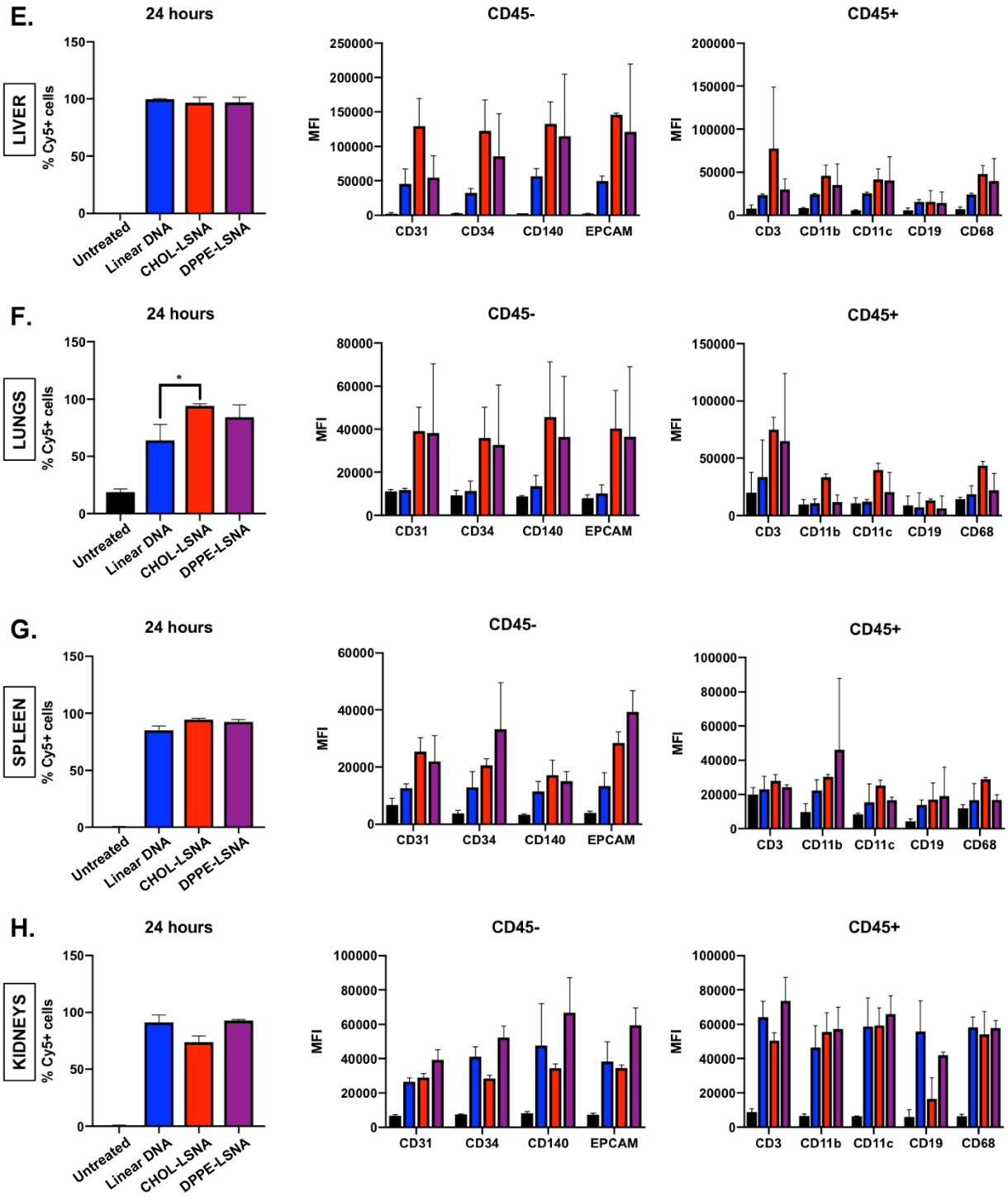

Figure 2.20 *Analysis of cellular distribution using flow cytometry.* Flow cytometry was used to assess the total accumulation of Cy5-DNA in immune and non-immune cells from linear DNA

and LSNAs in the liver, lungs, spleen, and kidneys at (A-D) 30 minutes and (E-H) 24 hours. (N = 3; Statistical significance comparing percent Cy5+ cells was calculated by one-way ANOVA with Tukey's post hoc test; *P<0.05, error bars represent standard deviation).

2.4 Conclusions

In summary, the results from this study suggest that LSNAs are not immediately cleared from circulation and that they may be used to direct nucleic acids to cells and organs outside of those rich in cells of the mononuclear phagocyte system (MPS). This is an important finding, as the MPS is a major hurdle in the delivery of nanoparticle-based therapeutics,[28,30,141] but understanding how structure dictates where LSNAs (or the nucleic acids that comprise SNAs) accumulate upon intravenous administration allows for the rational design of targeted LSNA therapeutics. This insight broadens the scope of the clinical indications that could benefit from LSNA therapies.

We show that the architecture of LSNAs offers a delivery advantage over linear DNA, as the DNA derived from LSNAs is observed in greater quantity in most tissues and circulation after 30 minutes and 24 hours post injection. Distribution differences between linear DNA and LSNAs are likely due to a decreased inflammatory cytokine response and a different clearance mechanism. The SNA architecture's ability to enhance nucleic acid transport across barriers within the body and uptake into many cell types may also drive these distribution differences.

In addition, we have shown that the affinity of DNA to its liposome template affects the distribution of LSNAs *in vivo*. This is a particularly important design consideration for therapeutic LSNA development. CHOL-LSNAs show high DNA trafficking to the lungs, which could lead to therapeutic development for indications such as chronic obstructive pulmonary

disease, pulmonary fibrosis, or lung cancer. DPPE-LSNAs show high DNA accumulation in the kidneys at the time points examined, which could be beneficial for treating glomerular diseases. These LSNAs also exhibit high accumulation in the spleen, indicating potential as cancer vaccines. The dense DNA shell on LSNAs also changes the tissue-level distribution of the liposome core. The CHOL-LSNA architecture enhanced the delivery of the liposome core to the liver and lungs, while the DPPE-LSNA architecture significantly increased the delivery of liposomes to the brain. As the liposome components of LSNAs can be loaded with other drug cargos, LSNAs have the potential to co-deliver drugs and nucleic acids to several major organs. We envision that the readily-tailorable distribution we describe in this article will inform further applications of this technology, especially in targets where structure dictates significant delivery enhancement.

2.5 Materials and Methods

2.5.1 Synthesis and characterization of LSNAs

DNA oligonucleotides were synthesized using automated solid support phosphoramidite synthesis (model: MM12, BioAutomation, Inc.). The sequence used, ODN 2138, has been previously shown to be non-immunogenic in linear and SNA form[47]. The free strand non-targeting (ODN 2138) sequence is 5'-TCCATGAGCTTCCTGAGCTT-Cy5-(spacer18)-(spacer18)-3'. On the nanoparticle, the non-targeting (ODN 2138) sequence is 5'-TCCATGAGCTTCCTGAGCTT-Cy5-(spacer18)-(spacer18)-cholesterol-3'. The DBCO-modified non-targeting (ODN 2138) sequence is 5'-TCCATGAGCTTCCTGAGCTT-Cy5-(spacer18)-(spacer18)-DBCOdT-3'. All oligonucleotides were synthesized with a phosphorothioate (PS) backbone. Sequences were purified by high-pressure liquid chromatography (HPLC, Agilent Technologies) and characterized using matrix assisted laser

desorption ionization-time of flight (MALDI-ToF, Bruker Autoflex III).1,2-dioleoyl-*sn*-glycero-3-phosphocholine (DOPC), 1,2-dipalmitoyl-sn-glycero-3-phosphoethanolamine-N-(6-azidohexanoyl) ammonium salt (Azido-Cap PE), and 1-palmitoyl-2-(dipyrromethene boron difluoride)undecanoyl-sn-glycero-3-phosphocholine (Topfluor® TMR-PC) all purchased from Avanti Polar Lipids, Inc. were dissolved in chloroform and prepared into a lipid film. The solvent was evaporated under nitrogen, and trace chloroform was removed under vacuum for several hours. Following this, the lipid film was rehydrated in a buffer containing 20 mM HEPES and 150 mM NaCl (pH 7.4) and freeze-thaw cycled several times. The solution was then extruded through polycarbonate membranes of increasingly smaller pore size (100 nm, 80 nm, 50 nm) until the resulting small unilamellar vesicles were monodisperse with a hydrodynamic radius of ~50 nm as ascertained by dynamic light scattering (DLS) (Malvern Instruments). The concentration of lipids was determined *via* elemental analysis using inductively-coupled plasma optical emission spectrometry (ICP-OES, Thermo Fischer Scientific). DNA loading to each nanoparticle was determined by measuring the DNA absorbance at 260 nm of LSNAs dissociated in 0.1% sodium dodecyl sulfate using a UV-VIS spectrophotometer and measuring total phosphorus concentration using ICP-OES.

Based on analysis of maximum cholesterol DNA loading on 50 nm liposomes shown in Figure 2.3, 1.3 mM of total lipids were mixed with 20 μM cholesterol- or DBCO-terminated DNA for 3-4 hours at 37 °C under constant agitation. The hydrodynamic radius and polydispersity were measured by DLS.

2.5.2 TEM of LSNAs

LSNA samples were negative stained with 2% (w/v) uranyl acetate. LSNAs were drop cast on TEM grids containing a carbon film on 300 copper mesh (Ted Pella, Inc.). After 30

seconds, the liquid was wicked away using filter paper and the sample was rinsed twice with 20 mM HEPES containing 150 mM NaCl to remove particles not adhered to the grid. Subsequently, uranyl acetate stain solution was dropped onto the grid, removed 4 times using filter paper, and the grid was air dried. A JEOL 1230 TEM (JEOL, Ltd.) was used for imaging.

2.5.3 Animal handling

Male mice (C57Bl/6) in the age range of 8-12 weeks were obtained from The Jackson Laboratory and maintained in conventional housing. All animals used were handled according to methods and procedures approved by the Institutional Animal Care and Use Committee at Northwestern University. Briefly, mice were given a single bolus injection of 50 μM linear DNA or LSNAs *via* peripheral intravenous injection. At pre-determined periods of time, mice were anesthetized using a 1:1 mixture of ketamine:xylazine, and blood was collected *via* cardiac puncture. Organs were cleared of blood by transcardial perfusion with 1X phosphate buffered saline (PBS).

2.5.4 Evaluation of cytokine production

Once blood was removed *via* cardiac puncture, it was allowed to clot on ice. Samples were centrifuged at a minimum of 400 g for 5 minutes. The supernatant was isolated, immediately frozen, and stored until analysis. The amounts of IL-6, IL-10, IL-12p70, MCP-1, TNF, and IFNy were measured using a flow-cytometry based multiplexing assay (CBA Mouse Inflammation Kit, BD Biosciences) on a FACSymphony flow cytometer (Becton Dickinson), and data was visualized using FlowJo (version 10.5.3, FlowJo LLC).

2.5.5 Organ harvest for IVIS imaging

Organs for imaging were harvested, fixed in 10% neutral buffered formalin overnight, then stored in 1X PBS until imaging using an *In Vivo* Imaging System (IVIS, Perkin Elmer). An

excitation wavelength of 535 nm and an emission wavelength of 580 was used to visualize TAMRA-labeled lipids, and an excitation wavelength of 640 nm and an emission wavelength of 680 nm was used to quantify the relative fluorescence of the Cy5-labeled DNA. One-way ANOVA was used to calculate significance between groups.

2.5.6 Fluorescence imaging

Following IVIS imaging, the same organs were placed in 15-30% sucrose at 4°C until the organs sunk to the bottom of the vial. Tissues were then embedded in a glycol/resin mixture (Tissue-Tek® O.C.T.) and snap frozen using liquid nitrogen. Tissues were cryosectioned to 5 μm slices and placed on glass slides. The slides were stained with fluorescein-phalloidin and mounted with an antifade mountant containing 4′,6-diamidino-2-phenylindole (DAPI) (Thermo Fisher Scientific) and imaged using an inverted microscope (Zeiss Axio 7 inverted microscope with AxioCam 506 mono).

2.5.7 Flow cytometry

Organs for flow cytometry were harvested, minced, and incubated in an enzymatic digestion mixture (collagenase with DNaseI, with or without elastase) for 30 minutes at 37°C. Once digested, organs were sieved through a 70 μm cell strainer and centrifuged. Red blood cell lysis was performed as necessary (Gibco). Single cells were washed with 1X PBS/2% bovine serum albumin (BSA) and stored on ice. Cells were stained for immune (CD45, CD3, CD19, CD11b, CD11c, CD68) and non-immune (EPCAM, CD31, CD140a, CD34) markers (Becton Dickinson, BioLegend) as well as with a fixable live/dead stain (Thermo Fisher Scientific). Cells were fixed in neutral buffered formalin after staining. Analysis of DNA association was done using a FACSymphony flow cytometer (Becton Dickinson), and data was visualized using

FlowJo (version 10.5.3, FlowJo LLC). One-way ANOVA was used to calculate significance between treatment groups.

2.5.8 Statistical analysis

All results are expressed as the mean ± SE or mean ± SD and number of biological replicates (N) as noted in the figure captions. Outliers were removed using the ROUT method with a false discovery rate (Q) of 1%. IVIS data of whole organ fluorescence of the Cy5-DNA and TAMRA liposomes are normalized to the untreated organs, hence all bar graphs are reported in fold fluorescence enhancement over untreated organs. One-way analysis of variance (ANOVA) was performed and Tukey's post hoc test was used for multiple comparisons when the result was significant ($P<0.05$). In analyzing the flow cytometry data (Figure 2.20), significance tests were applied to the % Cy5 positive cells in each organ, but not to the MFI values, as removing Cy5 negative cells does not retain a normal distribution in the data. All statistical analyses were performed with GraphPad Prism 8.

CHAPTER THREE

3 LIPID NANOPARTICLE SNAS FOR INTRACELLULAR DNA AND RNA DELIVERY

Portions of this chapter reprinted (adapted) with permission from: Sinegra, A J., Evangelopoulos, M.E., Park, J., Huang, Z, Mirkin, C.A. Lipid Nanoparticle Spherical Nucleic Acids for Intracellular DNA and RNA Delivery. *Nano Letters*. **2021**. https://doi.org/10.1021/acs.nanolett.1c01973

3.1 Summary

Lipid nanoparticle SNAs (LNP-SNAs) have been synthesized for the delivery of DNA and RNA to targets in the cytoplasm of cells. Both the composition of the LNP core and surface-presented DNA sequences contribute to LNP-SNA activity. G-rich sequences enhance activity of LNP-SNAs compared to T-rich sequences. In the LNP core, increased cholesterol content leads to greater activity. Optimized LNP-SNA candidates reduce the siRNA concentration required to silence mRNA by two orders of magnitude compared to liposome-based SNAs. In addition, the LNP-SNA architectures alter biodistribution and efficacy profiles in mice. For example, mRNA within LNP-SNAs injected intravenously is primarily expressed in the spleen, while mRNA-encapsulated by LNPs (no DNA on surface) was expressed primarily in the liver with a relatively small amount in the spleen. These data show that the activity and biodistribution of LNP-SNAs architectures are different from conventional liposomal SNAs and therefore potentially can be used to target tissues.

3.2 Introduction

Effective delivery at clinically relevant doses is a challenge limiting the implementation of DNA and RNA therapeutics. Nucleic acids can be used in gene silencing,[3,142–144] genome editing,[9–11] gene replacement,[18,19] immune system modulation,[20–22] and theranostics.[23–25] While significant progress has been made in each of these areas, therapy development often requires extensive modification of both the encapsulated DNA or RNA sequence and its carrier to prevent nuclease degradation and enhance tissue and cellular uptake. The spherical nucleic acid (SNA) addresses some of the challenges of nucleic acid delivery without the need for extensive sequence modifications. In these structures, the oligonucleotides, DNA or RNA, are radially oriented around a spherical nanoparticle template. This dense three-dimensional arrangement improves DNA and RNA delivery by increasing nuclease resistance and accumulation in many cell types, through scavenger receptor engagement.[58] In cellular assays, the SNA architecture increases the degradation half-life and cellular uptake in a sequence-dependent manner.[52,63,65] SNA structures generated using modular nanoparticle cores such as liposomes can be tuned for greater tissue-specific delivery. For instance, in wild-type mice, SNAs distribute based on the DNA sequence's affinity for the liposome core. Here, the hydrophobicity of the sterol or lipid anchoring the DNA sequences to the nanoparticle surface determines the amount of SNAs that will be delivered to the liver, spleen, or lungs.[40,63,145] SNAs also enhance the function of the nucleic acids compared to their equivalent linear form. ASOs formulated into liposome-based SNAs enter cells and inhibit gene expression at micromolar concentrations.[44,45] Consequently, SNAs delivering both DNA and RNA are showing promising results in the clinic.[41,125,127]

While clinically relevant activity is one requirement, nanocarriers must achieve sufficient delivery to the target while avoiding potentially harmful effect in other organs. Thus, a structure

that can control distribution and enhance activity of the nucleic acids is needed. SNA architectures based on nanoparticles used for escape from cellular compartments may increase potency while retaining the SNA structure-dependent biodistribution properties. Lipid nanoparticles (LNPs) are a modular class of nanoparticle that can effectively encapsulate many types of nucleic acids and rely on endogenous lipid trafficking pathways for delivery.[89] Advances in LNP chemistry enable siRNA and mRNA delivery at therapeutically relevant concentrations. For this reason, LNPs are the nanocarriers used in a variety of FDA approved RNA therapeutics.[146] Although SNA architectures based upon LNP cores have the potential to deliver encapsulated nucleic acid at relevant concentrations as well as enhance tissue retention and sequence-specific targeting, they have yet to be synthesized and studied. To synergize the advantages of both LNPs and SNAs, a large parameter space of both LNP nanoparticle cores and DNA sequences must be explored. This requires an efficient optimization process as well as benchmarking LNP-SNA activity with that of previously studied SNAs and bare LNPs that have no surface conjugated DNA. Finally, to assess the potential of LNP-SNAs as genetic medicines, it is necessary to determine how adding conjugated DNA to the surface of LNP-SNAs alters activity and targeting ability in mice after intravenous injection.

Here, we report a strategy that employs Design of Experiment (DoE) methodologies[94] such as definitive screening designs and fractional factorials to generate SNAs from LNP structures (LNP-SNAs). This approach hastens the discovery of optimal LNP-SNA formulations by reducing the number of conditions required to assess the effects of each factor and the two-factor effects. Large-scale experiments at the initial stages of LNP-SNA development are time- and material-prohibitive. For screening purposes, we synthesized LNP-SNAs with a 45 base-pair

(bp) DNA sequence designed to bind cyclic GMP-AMP synthase (cGAS), activating the cytosolic cGAS-STING pathway. This pathway, while a useful proof-of-concept for DNA delivery to bind cytosolic proteins, is also therapeutically relevant.[147,148] STING activation in the tumor microenvironment leads to significant regression of solid tumors. Doubled-stranded (ds) DNA binding to cGAS leads to activation of transcription factors such as IRF3.[149–151] Thus, with a cell line engineered to secrete luciferase as a result of IRF3 induction, we can use luminescence as an output for DNA delivery.

3.3 Results and Discussion

3.3.1 LNP-SNA Synthesis and Library A Screening Using a Definitive Screening Design

LNPs were synthesized using the ethanol dilution method,[84] where the aqueous phase containing the nucleic acids (DNA or RNA) in 10 mM citrate buffer (pH 4) was mixed with the ethanol phase containing the various lipids, including an ionizable lipid (Figure 3.1A, 1B), phospholipid, lipid-PEG, and cholesterol (Figure 3.1C). The phospholipid is designed to support the structure and may aid in endosomal escape.[88,152] The cholesterol enhances LNP stability and promotes the fusion of LNPs with biological membranes.[86,153] The ionizable lipids are positively charged at endosomal pH, which aids in cytosolic delivery and nucleic acid loading.[89,92,152,154,155] Lipid-PEGs are used to prevent nanoparticle aggregation and increase blood circulation times.[89] Lipid-PEG(2000)-maleimides coat the surface of our LNPs and provide a conjugation site for sulfhydryl-terminated DNA. In Library A, we used 1,2-dioleoyl-*sn*-glycero-3-phosphocholine (DOPC) as the phospholipid. In addition, we tested two different commercially available ionizable lipids, 1,2-dioleoyl-3-dimethylammonium-propane (18:1 DAP) and dilinoleylmethyl-4-dimethylaminobutyrate (DLin-MC3-DMA) (Figure 3.1B), and three different lipid-PEG(2000)-

maleimides which differed in the length of the lipid's diacyl tail (Figure 3.1C). Six different molar ratios of these components were used (Table S1).

Table 3.1 *List of LNP-SNA formulations used*

Lib_#	Phospholipid	ionizable lipid	lipid-PEG	surface DNA	% phospholipid	% chol.	% ionizable lipid	% lipid-PEG	EE (%)	size (nm)	sd (nm)
A_1	DOPC	DLin-MC3	C18	T21	10	35	50	5	82	159	79
A_2	DOPC	18:1 DAP	C14	T21	24	25	50	1	84	279	107
A_3	DOPC	DLin-MC3	C18	T21	20	25	50	5	67	227	81
A_4	DOPC	18:1 DAP	C14	T21	14	35	50	1	85	221	105
A_5	DOPC	18:1 DAP	C18	T21	12.5	35	50	2.5	86	203	85
A_6	DOPC	DLin-MC3	C14	T21	22.5	25	50	2.5	74	246	91
A_7	DOPC	DLin-MC3	C16	T21	12.5	35	50	2.5	78	195	87
A_8	DOPC	18:1 DAP	C16	T21	22.5	25	50	2.5	83	190	91
A_9	DOPC	DLin-MC3	C14	T21	10	35	50	5	56	236	71
A_10	DOPC	18:1 DAP	C18	T21	24	25	50	1	88	277	91
A_11	DOPC	DLin-MC3	C16	T21	22.5	25	50	2.5	71	222	71
A_12	DOPC	18:1 DAP	C16	T21	12.5	35	50	2.5	87	178	83
A_13	DOPC	18:1 DAP	C16	T21	20	25	50	5	85	231	81
A_14	DOPC	DLin-MC3	C16	T21	14	35	50	1	79	227	60
A_15	DOPC	18:1 DAP	C16	T21	10	35	50	5	83	187	84
A_16	DOPC	DLin-MC3	C16	T21	24	25	50	1	71	229	69
A_17	DOPC	18:1 DAP	C14	T21	24	25	50	1	83	209	81
A_18	DOPC	DLin-MC3	C18	T21	10	35	50	5	80	144	79
B_1	DSPC	DLin-MC3	C16	GGT7	12.5	35	50	2.5	100	194	80
B_2	DSPC	DLin-MC3	C16	GGT7	12.5	35	50	2.5	103	197	73
B_3	DOPE	DLin-MC3	C14	GGT7	22.5	25	50	2.5	77	220	77
B_4	DOPE	DLin-MC3	C14	GGT7	22.5	25	50	2.5	84	217	76
B_5	DOPC	DLin-MC3	C16	T21	1.5	45	50	3.5	95	202	73
B_6	DOPC	DLin-MC3	C16	T21	1.5	45	50	3.5	97	184	76
B_7	DOPE	DLin-MC3	C16	GGT7	21.5	25	50	3.5	94	194	66
B_8	DSPC	DLin-MC3	C14	T21	22.5	25	50	2.5	93	274	82
B_9	DOPE	DLin-MC3	C16	GGT7	13.5	35	50	1.5	98	218	78
B_10	DSPC	DLin-MC3	C16	GGT7	23.5	25	50	1.5	101	317	94
B_11	DOPE	DLin-MC3	C14	T21	12.5	35	50	2.5	86	232	75
B_12	DOPC	DLin-MC3	C14	GGT7	1.5	45	50	3.5	91	233	79
B_13	DOPE	DLin-MC3	C16	T21	3.5	45	50	1.5	98	194	71
B_14	DOPC	DLin-MC3	C16	GGT7	22.5	25	50	2.5	99	225	82
B_15	DSPC	DLin-MC3	C14	T21	3.5	45	50	1.5	92	239	82
B_16	DSPC	DLin-MC3	C14	T21	11.5	35	50	3.5	93	242	77
B_17	DSPC	DLin-MC3	C14	GGT7	2.5	45	50	2.5	75	276	70
B_18	DOPE	DLin-MC3	C14	T21	23.5	25	50	1.5	72	303	70
B_19	DOPE	DLin-MC3	C14	GGT7	3.5	45	50	1.5	73	229	93
B_20	DOPC	DLin-MC3	C14	GGT7	12.5	35	50	2.5	76	231	89
B_21	DOPC	DLin-MC3	C16	GGT7	11.5	35	50	3.5	79	210	76
B_22	DSPC	DLin-MC3	C16	T21	2.5	45	50	2.5	79	229	79
B_23	DOPC	DLin-MC3	C14	T21	21.5	25	50	3.5	75	220	76
B_24	DSPC	DLin-MC3	C14	GGT7	13.5	35	50	1.5	80	239	81
B_25	DOPC	DLin-MC3	C16	T21	23.5	25	50	1.5	80	240	95
B_26	DSPC	DLin-MC3	C16	GGT7	1.5	45	50	3.5	76	237	83
B_27	DOPE	DLin-MC3	C14	T21	1.5	45	50	3.5	74	266	91
B_28	DSPC	DLin-MC3	C16	T21	11.5	35	50	3.5	72	243	83
B_29	DOPE	DLin-MC3	C14	GGT7	11.5	35	50	3.5	72	270	84
B_30	DOPC	DLin-MC3	C14	T21	2.5	45	50	2.5	76	295	84
B_31	DOPE	DLin-MC3	C16	T21	22.5	25	50	2.5	74	223	79
B_32	DOPC	DLin-MC3	C14	T21	13.5	35	50	1.5	77	277	90
B_33	DOPC	DLin-MC3	C16	GGT7	3.5	45	50	1.5	79	187	72
B_34	DOPE	DLin-MC3	C16	GGT7	2.5	45	50	2.5	76	214	81
B_35	DSPC	DLin-MC3	C14	GGT7	21.5	25	50	3.5	79	206	72
B_36	DOPC	DLin-MC3	C16	T21	12.5	35	50	2.5	80	232	73
B_37	DOPC	DLin-MC3	C14	GGT7	23.5	25	50	1.5	81	203	76
C_1	DOPC	DLin-MC3	C16	GGT7	2.5	45	50	2.5	85	212	88
C_2	DOPC	DLin-MC3	C16	GGT7	1.5	45	50	3.5	90	167	106
C_3	DSPC	DLin-MC3	C16	GGT7	3.5	45	50	1.5	86	147	99
C_4	DOPE	DLin-MC3	C16	GGT7	3.5	45	50	1.5	87	102	62

Following dialysis against PBS, the diameter of the LNPs was characterized by nanoparticle tracking analysis (NTA), and their encapsulation efficiency was determined using a fluorescence-based assay (Table 3.1). The LNP-SNAs in Library A had a median hydrodynamic diameter of 221 nm (Figure 3.3D) and median encapsulation efficiency of 82% (Figure 3.3E). To form SNAs from the LNPs, the LNPs were mixed with 3'-sulfhydryl terminated DNA to facilitate conjugation to the surface-presented lipid-PEG(2000)-maleimides (Table 3.2).

Table 3.2. *DNA sequences used*

Formulation	**DNA Sequence (5'-3')**
T21 SNA	TTTTTTTTTTTTTTTTTTTT -SH[a]
(GGT)7 SNA	GGT GGT GGT GGT GGT GGT GGT GGT-SH[a]

[a] Synthesized using Dithiol Serinol CpG (Glen Research), subsequently reduced using 100 mM DTT in 20 mM Tris HCl pH 8.3-8.5 for 30 min and desalted on a NAP-10 column (Cytiva).

LNP-SNA formation was confirmed by agarose gel electrophoresis (Figure 3.1). In Library A, we used a poly(T) DNA sequence (T21-SH) as it does not form secondary structures. To confirm that the outer DNA sequence used to form LNP-SNA structures does not cause background cGAS-STING pathway activation, we transfected each DNA sequence used in screening experiments. Only the 45 bp dsDNA sequence specific for cGAS recognition resulted in detectable IRF3 induction (Figure 3.2, Figure 3.3).

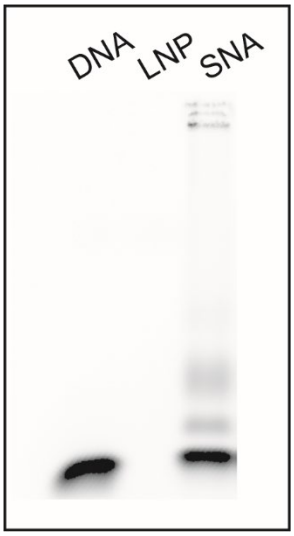

Figure 3.1 *Agarose gel to confirm surface DNA conjugation* 1% agarose gel run in TAE buffer to confirm conjugation of T21 DNA to LNPs after 2 h shaking at RT. One equivalent of a T21-SH DNA sequence labeled with Cy5.5 was added to formulation B-35, which contains 3.5% C14-PEG(2000)-Maleimides. Presence of bands at higher MW than free Cy5.5 DNA (Lane 1), indicates that they are conjugated to the lipid-PEG.

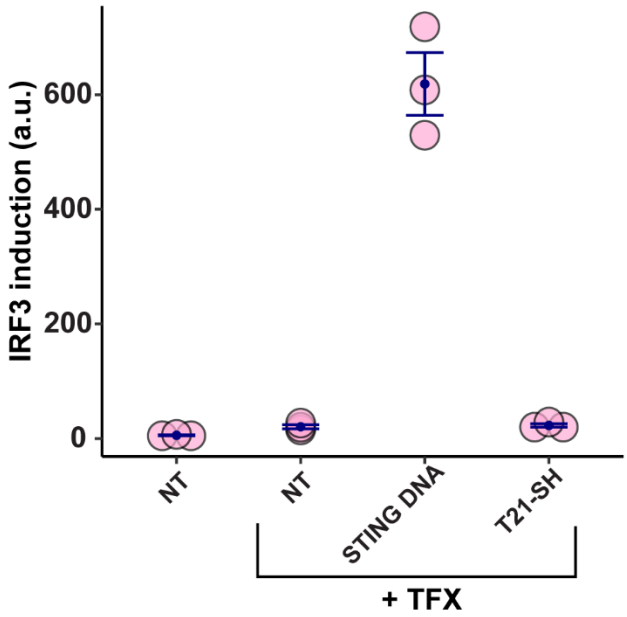

Figure 3.2 *DNA sequence controls for Library A screening.*

IRF3 induction of DNA sequences used in Library A measured after 24 h. Sequences were transfected with Lipofectamine 2000™ according to manufacturer's protocol. (TFX = with transfection; NT = not treated.)

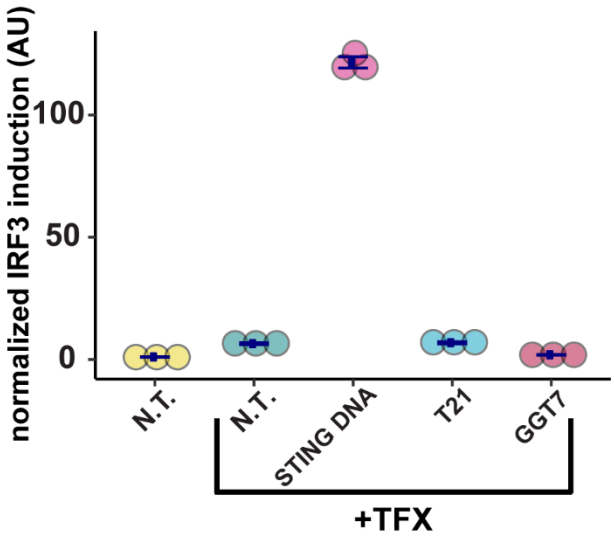

Figure 3.3 *Sequence controls used in Library B screening*

IRF3 induction of DNA sequences used in Library B measured after 24 h. Sequences were transfected with Lipofectamine 2000™ according to manufacturer's protocol. (TFX = with transfection; NT = not treated.)

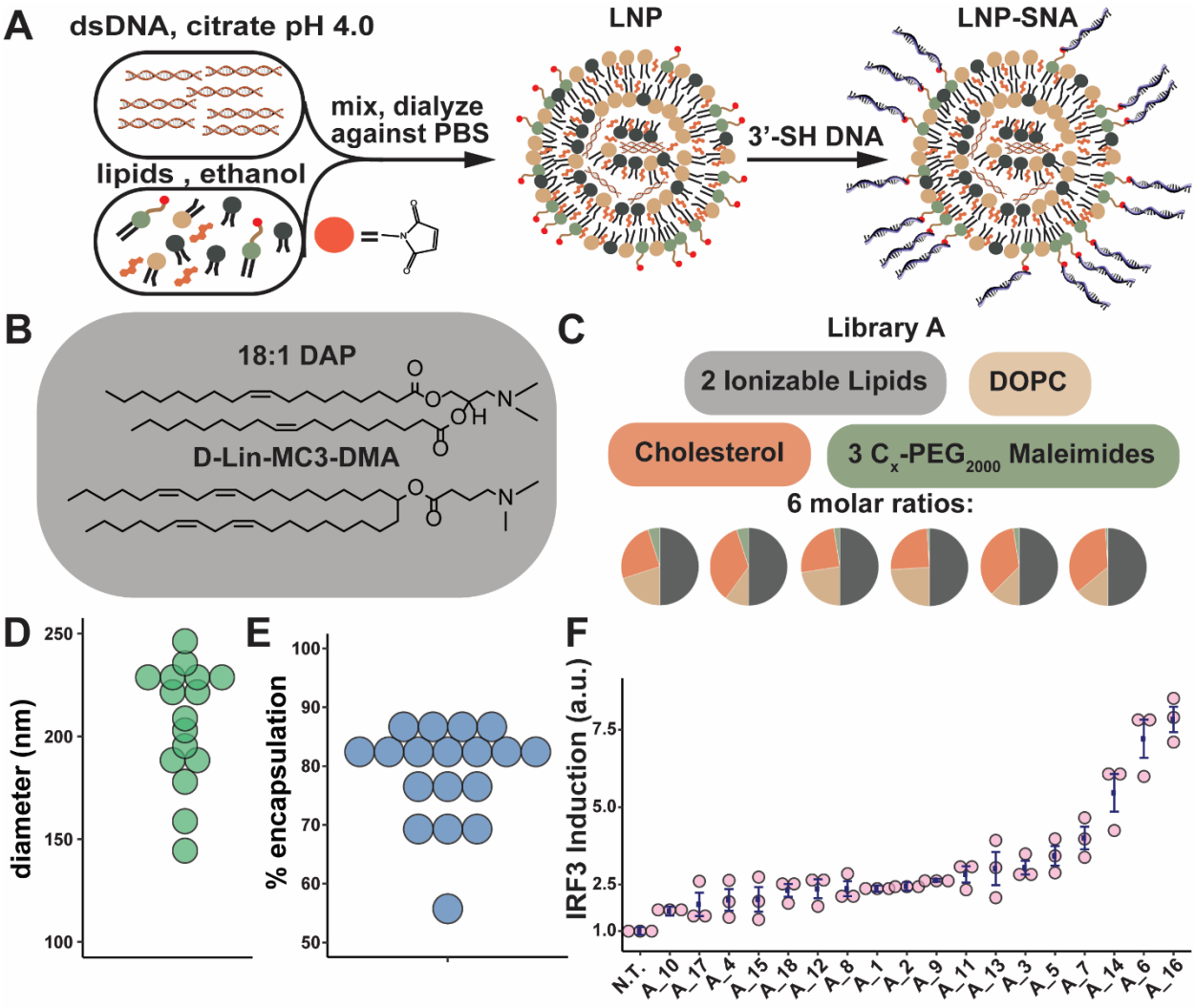

Figure 3.4 *Characterization of LNP-SNA Library A.* (A) Synthesis of LNP-SNAs. LNPs loaded with nucleic acids are formed *via* the ethanol dilution method. DNA or mRNA dissolved in a pH 4.0 citrate buffer is mixed with lipids and cholesterol in ethanol. Next, the LNPs, which contain lipid-PEG-maleimides (red circles), are mixed with 3'-SH DNA (blue) overnight at RT resulting in LNP-SNAs. (B) Ionizable lipids used in Library A. (C) Library A components are mixed at 6 different molar ratios and resulting LNPs are functionalized with a T21 DNA sequence. (D) Diameter of LNP-SNAs in Library A. (E) Encapsulation efficiency of LNP-SNAs in Library A.

(F) IRF3 induction of each formulation in Raw 264.7-Lucia™ ISG cells treated for 24 h with 100 nM DNA (N.T. = not treated, error bars represent s.e.m., n = 3 biologically independent replicates).

To estimate both the main effects of each parameter as well as second-order effects between parameters, we employed a definitive screening design.[94] This ensures that: (1) the main effects are not confounded with 2-factor effects, (2) we can detect nonlinear correlations, and (3) we can eliminate unimportant formulation parameters for following screening experiments. The IRF3 induction screen of Library A yielded five LNP-SNAs that significantly activated the cGAS-STING pathway ($p < 0.05$ compared to untreated (N.T.), Figure 3.4F). These five LNP-SNAs contained either C14 or C16 lipid-PEGs, 1-2.5% lipid-PEGs, and DLin-MC3-DMA as the ionizable lipid. These compositions are similar to those found in the LNP literature, where lower lipid-PEG mol% and shorter diacyl tails on lipid-PEGs often lead to greater activity.[93,95] Additionally, DLin-MC3-DMA, one of the most frequently used lipids in clinical trials, is known to be effective for delivery of siRNA and mRNA.[15,155] From these findings, we eliminated unimportant compositions including the 18:1 DAP ionizable lipid and the C18 lipid-PEG and expanded the design space around the top five LNP-SNA formulations to create a second library.

3.3.2 Library B Screening using a Fractional Factorial Design

In Library B, we investigated two additional phospholipids to test whether the structure of the phospholipid's tail or head group changes LNP-SNA function (Figure 3.4A). 1,2-distearoyl-*sn*-glycero-3-phosphocholine (DSPC), has the same head group as DOPC, but has a saturated lipid tail. 1,2-dioleoyl-*sn*-glycero-3-phosphoethanolamine (DOPE), has a primary amine in its head group instead of the quaternary amine present in phosphatidylcholine. Because

LNPs with shorter lipid-PEG-maleimides exhibited greater IRF3 induction, we limited library B to C14 and C16 maleimide-PEG(2000)-lipids. In addition to the T21-SH sequence, we included a G-rich (GGT × 7 -SH) DNA sequence, which forms a G-quadruplex secondary structure,[62,156] as these structures are known to enhance uptake of SNA structures *via* class A scavenger receptor-mediated endocytosis.[52,62] We hypothesized that increasing the number of LNP-SNAs taken up by cells may lead to greater cytosolic delivery if the same percent of LNP-SNAs escape endosomal compartments. To test the effects of each component as well as their interactions, we designed a resolution IV fractional factorial experiment. The full factorial design contained five factors, three with three levels and two with two levels (3 × 3 × 3 × 2 × 2), or 108 possible LNP-SNA compositions. With a resolution IV fractional factorial experiment, only 37 of the 108 possible LNP-SNAs structures are required to estimate the main effects and two-factor effects.

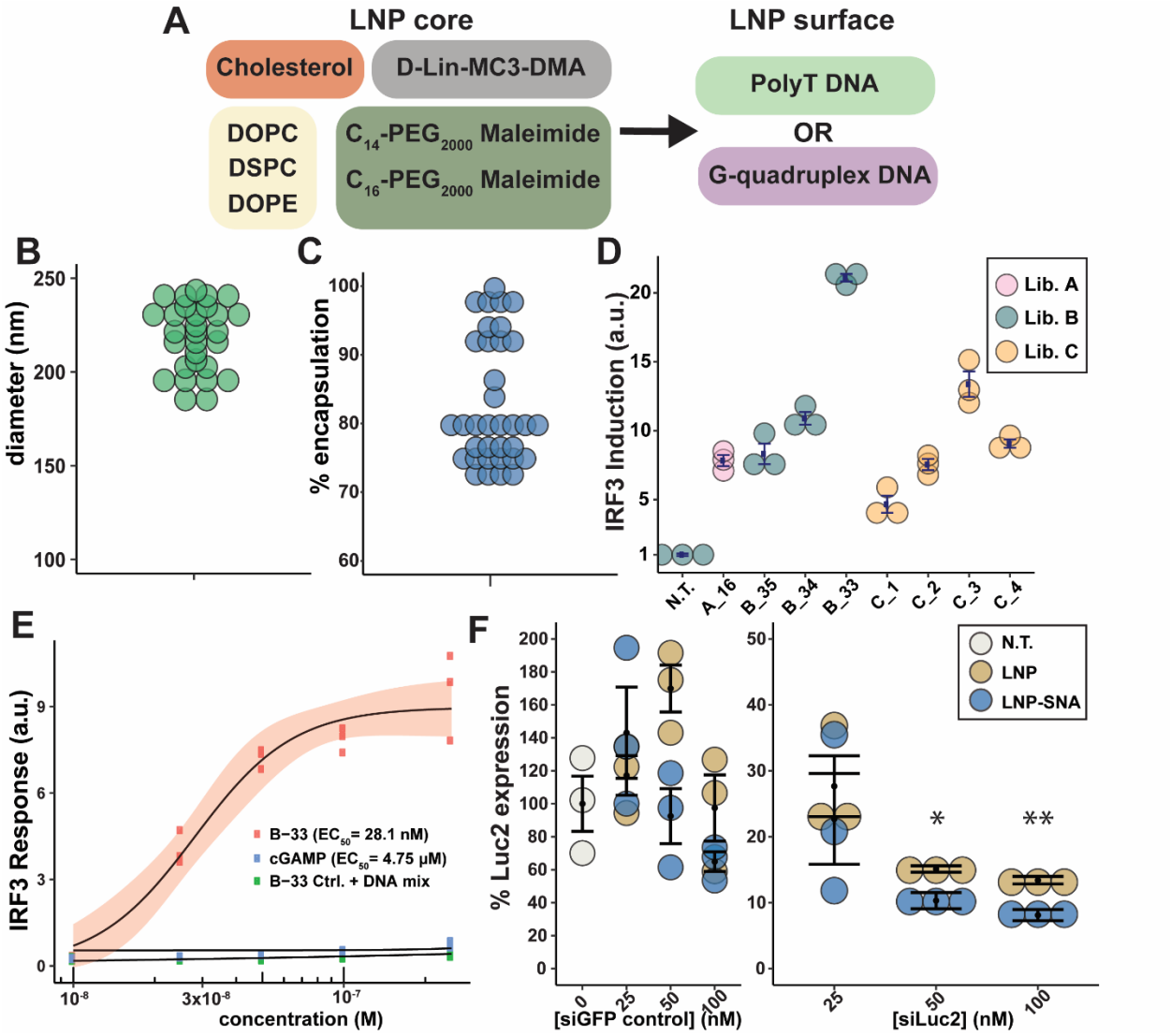

Figure 3.5 *DoE optimization process improves DNA and RNA delivery in vitro*. (A) Core compositions and surface DNA sequences used in Library B. (B) Diameter of Library B LNPs. (C) Encapsulation efficiency of LNP-SNAs in Library B. (D) IRF3 induction measured in RAW 264.7-Lucia™ ISG cell line of candidates in Libraries A, B, and C normalized to untreated samples (error bars represent s.e.m., n = 3 biologically independent replicates). (E) IRF3 induction of B-33 LNP-SNA, 2'3'-cGAMP, and B-33 LNP-SNA mixed with free dsDNA (red ribbon represents 95% C.I., n = 3 biologically independent replicates). (F) U87-Luc2 cells were

treated for 24 h with LNPs or LNP-SNAs encapsulating a siGFP control sequence or a siLuc2 targeting sequence (error bars represent s.e.m., n = 3 biologically independent replicates, one-tailed t-test comparing LNP and LNP-SNA * = $p \leq 0.05$, ** = $p \leq 0.01$).

LNP-SNAs in Library B exhibited a median diameter of 229 nm (Figure 3.5B) and a median encapsulation efficiency of 79 % (Figure 3.5C). As before, transfection was used to ensure that the surface presented G-rich sequence does not activate the cGAS-STING pathway (Figure 3.3). The IRF3 induction of the LNP-SNAs in Library B revealed that the highest-activating nanoparticle is B-33 (Figure 3.6), which contained 45 mol% cholesterol and the G-rich sequence.

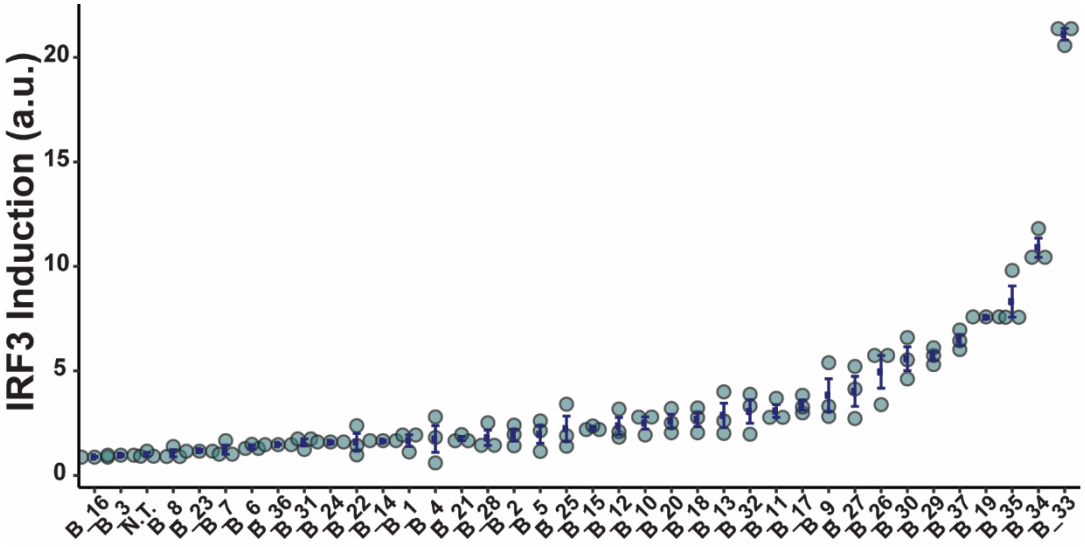

Figure 3.6 *Results of Library B screening*

IRF3 induction of LNP-SNAs used in Library B measured after 24 h. Results normalized to untreated wells. (NT = not treated, n = 3 biologically independent replicates)

To evaluate which factors best predicted LNP-SNA activity, we used a bootstrap forest algorithm (Table 3.3). We found that, from highest to lowest portions: mol% cholesterol, DNA

sequence, and mol% lipid-PEG were the three most important predictors of IRF3 induction (Table 3.4, Figure 3.7). Increasing mol% of cholesterol also had a positive interaction with lower levels of lipid-PEGs and for LNP-SNAs presenting the G-rich DNA sequence (Figure 3.8). The cholesterol may enhance endosomal escape of LNP-SNAs through membrane fusion.[157,158] The second most important predictor of activity in Library B was the outer DNA sequence. Due to its secondary structure, the G-rich DNA sequence increases uptake of the associated nanoparticles in SNA form compared to a poly(T) sequence,[62,66] which may be responsible for this effect. The observed sequence-dependent function of LNP-SNAs bodes well for the future use of different DNA or RNA secondary structures to enhance LNP-SNA function and targeting.

3.3.3 Library C: One-at-a-time design

A limitation of fractional factorial design is that the maximum activity obtained in the screening is a local maximum, not a global maximum. To determine whether B-33 is the global maximum of the design space in Library B, we changed lipid-PEG mol % and the phospholipid factors one-at-a-time and observed whether activity improved. Importantly, neither increased the activity, indicating that B-33 was in fact the maximum of this design (Figure 3.5D). With B-33 identified as the optimal design, we proceeded to benchmark its activity against the free DNA sequence and 2'3'-cGAMP, which activates STING downstream of cGAS and has been explored as a therapeutic. The median effective concentration (EC_{50}) by concentration of DNA of B-33 was 28.1 ± 2.9 nM, compared to 4.75 ± 0.13 μM for 2'3'-cGAMP (Figure 3.5E). As a control for non-specific activation from the delivery vehicle, we compared B-33 to the same formulation with an encapsulated T45 control sequence mixed with free STING dsDNA. We observed no non-specific IRF3 induction from B-33 structures without the encapsulated STING agonist.

Table 3.3 *Predictor Rank in Library B using Bootstrap Forest*

Predictor	Portion		Rank
chol%	0.3539		1
DNA_seq	0.2422		2
PEG%	0.1902		3
Phospholipid	0.1563		4
Peg length	0.0574		5

Table 3.4 *Summary of linear model used in Lib. B Analysis*

Summary of Fit	
RSquare	0.998965
RSquare Adj	0.987577
Root Mean Square Error	0.088216
Mean of Response	0.749427
Observations (or Sum Wgts)	37

Analysis of Variance				
Source	**DF**	**Sum of Squares**	**Mean Square**	**F Ratio**
Model	33	22.527795	0.682660	87.7217
Error	3	0.023346	0.007782	**Prob > F**
C. Total	36	22.551142		0.0017*

Effect Tests					
Source	**Nparm**	**DF**	**Sum of Squares**	**F Ratio**	**Prob > F**
Phospholipid	2	2	1.0969107	70.4764	0.0030*
PEG%	2	2	0.6603282	42.4260	0.0063*
chol%	2	2	4.7502410	305.2025	0.0003*
Peg length	1	1	0.0899112	11.5536	0.0425*
DNA_seq	1	1	1.6965052	218.0006	0.0007*
Phospholipid*PEG%	4	4	5.0465053	162.1187	0.0008*
Phospholipid*chol%	4	4	2.0945087	67.2860	0.0029*
PEG%*chol%	4	4	2.6670092	85.6775	0.0020*
Phospholipid*Peg length	2	2	0.2712912	17.4304	0.0223*
PEG%*Peg length	2	2	0.4875167	31.3229	0.0098*
chol%*Peg length	2	2	0.6619163	42.5281	0.0063*
Phospholipid*DNA_seq	2	2	0.5468453	35.1348	0.0083*
PEG%*DNA_seq	2	2	0.5789667	37.1986	0.0076*
chol%*DNA_seq	2	2	1.3582040	87.2645	0.0022*

Peg length*DNA_seq	1	1	0.1130788	14.5306	0.0317*

Source	LogWorth		PValue
chol%	3.466		0.00034
DNA_seq	3.171		0.00067
Phospholipid*PEG%	3.108		0.00078
PEG%*chol%	2.697		0.00201
chol%*DNA_seq	2.658		0.00220
Phospholipid*chol%	2.541		0.00287
Phospholipid	2.522		0.00301
chol%*Peg length	2.201		0.00629
PEG%	2.200		0.00631
PEG%*DNA_seq	2.117		0.00763
Phospholipid*DNA_seq	2.082		0.00829
PEG%*Peg length	2.010		0.00977
Phospholipid*Peg length	1.652		0.02230
Peg length*DNA_seq	1.498		0.03175
Peg length	1.372		0.04249

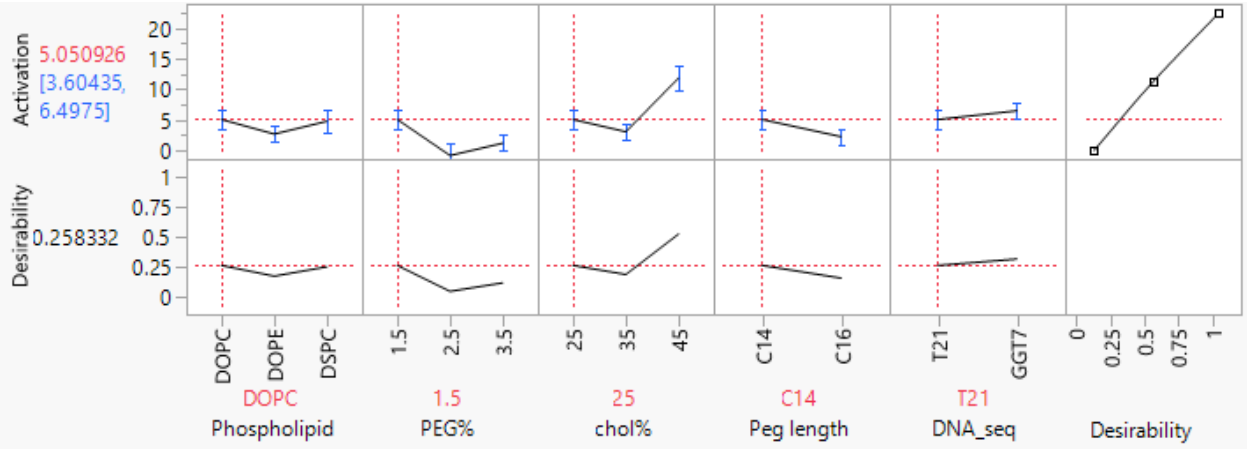

Figure 3.7 *Example main effects and desirability plots for SNAs in Library B.*

Activation (top row) and desirability (bottom row) of LNP-SNAs in Library B as a function of formulation parameters phospholipid, PEG%, cholesterol %, PEG length, and DNA sequence. The plot demonstrates how levels of each factor predict the activation or desirability (highest output of the Library scaled to 1, lowest output scaled to 0). In JMP, the red dashed lines can be moved to change levels of each factor, and the predicted activation is shown in red, along with a 95% confidence interval (blue).

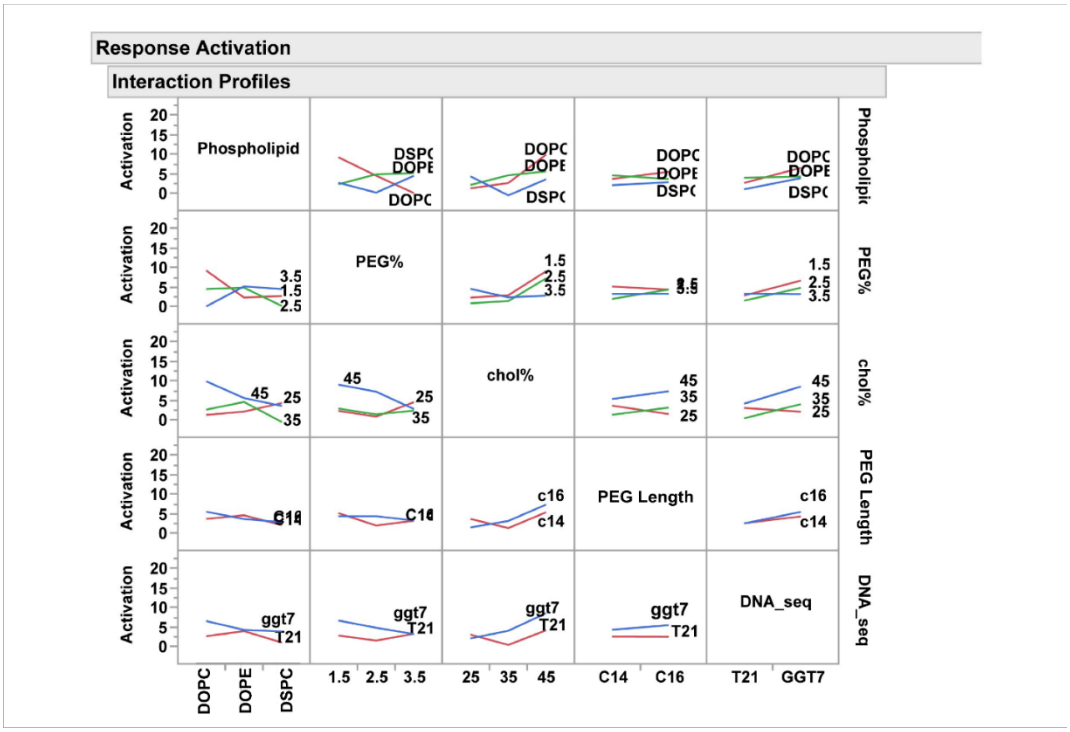

Figure 3.8 *Interaction effects between parameters in library B*

Interaction of each factor's levels (bottom) with another factor (right side). Plot reflects activity (a.u.), on the Y axis, as a function of the interaction between two factor levels in Library B.

3.3.4 siRNA delivery with cGAS-STING pathway induction optimized LNP-SNAs

While the cGAS-STING pathway was a useful screening tool for LNP-SNA optimization, we sought to more thoroughly benchmark nanoparticle activity using gene silencing. We quantified the activity of LNP-SNAs containing siRNA silencing luciferase gene (Luc2) as a model system. One of the benefits of LNPs is that they can effectively encapsulate a variety of nucleic acid cargos, including siRNA, mRNA, and Cas9 mRNA/single guide RNA.[15,159,160] As different sized nucleic acids may package differently within LNPs-SNAs, we performed an initial test using the top five LNP-SNAs from Libraries B and C. The test revealed

that a slightly different structure, B-35 (Table 3.1), silenced Luc2 the most without affecting cell viability (Figure 3.9).

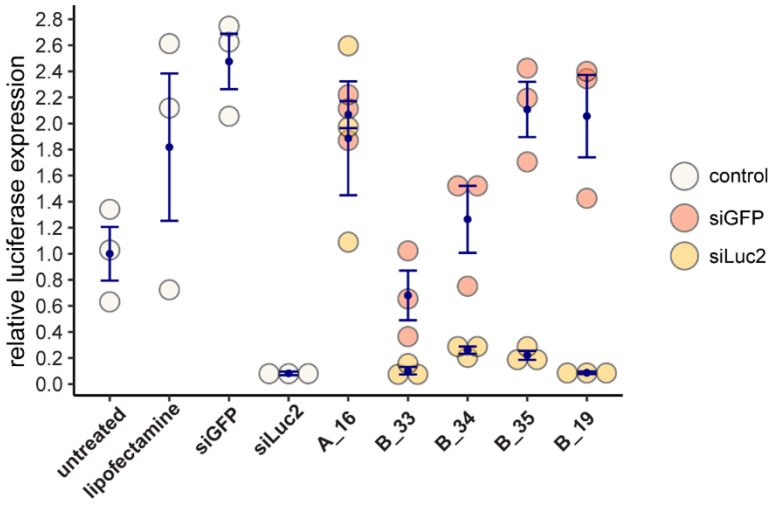

Figure 3.9 Initial Screening of siRNA-containing LNP-SNAs in B16-F10-Luc2 cells

B16-F10-Luc2 cells were treated with either transfected sequence controls (white) or LNP-SNAs formulated with either a control siGFP (orange) or siLuc2 (yellow) targeting sequence at 100 nM concentration for 24 h. (N.T. = not treated)

Therefore, we tested B-35 over a range of concentrations. In a U87-MG-Luc2 cell line, B-35 effectively silenced the constitutive Luc2 expression by up to 92% after 24 h and at a concentration as low as 25 nM (Figure 3.5F). While the surface presented G-rich DNA sequence had a significant effect on cGAS-STING pathway activation versus the poly(T) sequence, we sought to determine whether LNP-SNAs enhance the activity of the equivalent LNP. At the same siRNA treatment concentration, the B-35 LNP-SNA increased gene silencing activity of the equivalent LNP by ~ 5% at 50 nM ($p < 0.05$) and 100 nM ($p < 0.01$) siRNA concentrations (Figure 3.5F).

3.3.5 LNP-SNAs exhibit spleen-specific mRNA expression

Finally, we investigated the ability of these designs to deliver nucleic acids *in vivo*. For this, we used luciferase (Luc) mRNA so that we could detect luciferase protein production after injection of D-luciferin. Since the mRNA sequence is much longer than either the siRNA or the 45-bp STING DNA sequence, it may be packaged differently within LNP-SNA formulations. For this reason, we quantified the mRNA encapsulation efficiencies of the top three LNP-SNA candidates from the cGAS-STING pathway activation screening (B-19, B-33, and B-35). Of the three, B-19 exhibited greatest encapsulation efficiency (Table 3.5) and lowest polydispersity (Figure 3.10), and a zeta potential of -1.46 ± 0.44 mV.

Table 3.5 *mRNA encapsulation efficiency of top LNP-SNA candidates*

Sample	**Encapsulation efficiency (%)**	**Error (± %)**
B-35	46	4
B-34	70	2
B-19	78	3

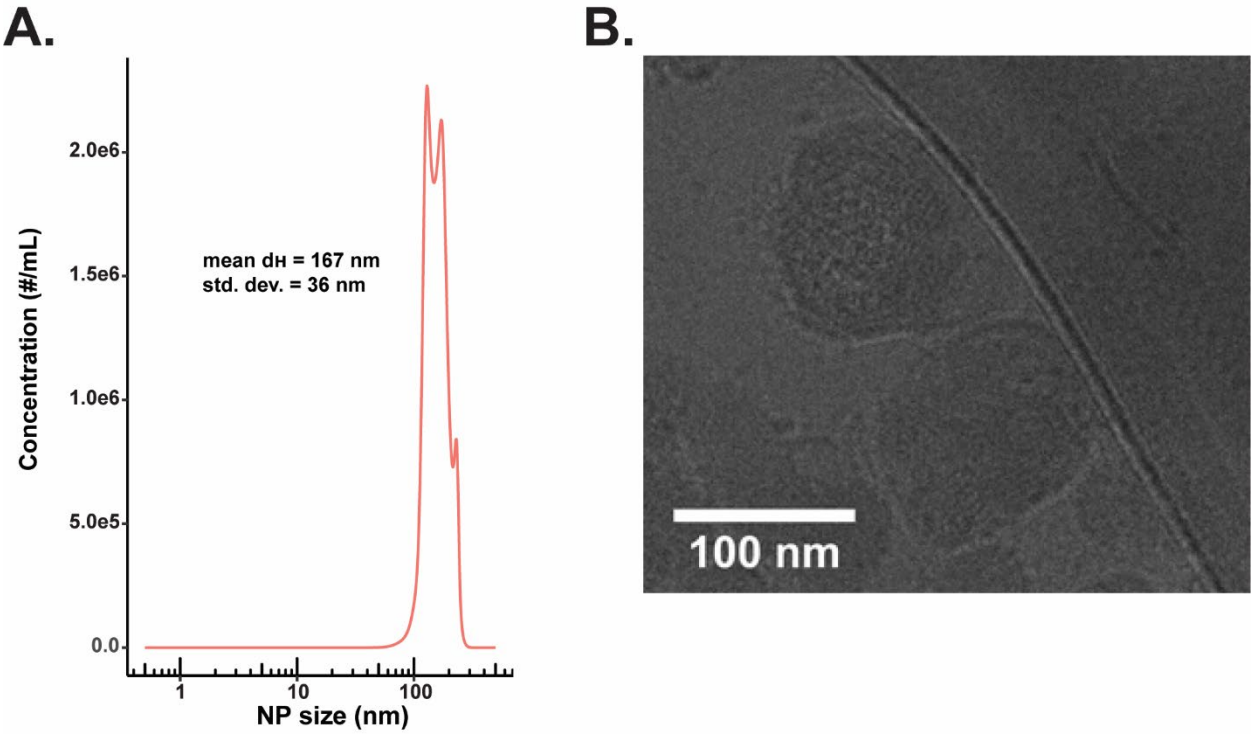

Figure 3.10 *Characterization of LNP-SNA B-19 with encapsulated Luc2 mRNA*

(A) Plot of the average of three NanoSight runs of B-19 LNP-SNA. (B) Cryo-TEM image of the same SNA.

Therefore, we used this formulation to evaluate Luc mRNA expression 6 h after intravenous injection of LNPs and LNP-SNAs into C57BL/6J mice (0.1 mg kg^{-1}). Comparing LNPs to LNP-SNAs, we observed significant differences in organ-level mRNA expression. In the liver, we observed that B-19 LNPs exhibited high levels of Luc mRNA expression, while the equivalent LNP-SNA had no expression (Figure 3.11A, 3B). In the spleen, however, both LNPs and LNP-SNAs exhibited roughly equal levels of mRNA expression (Figure 3.11C, N.S., two sample t-test), although both exhibited significantly greater expression than the control PBS treated mice. Differences between LNP and LNP-SNA functional distribution may be due to the differences in

receptors used for endocytosis of each nanoparticle. LNP uptake is largely mediated by the LDL receptor,[57] while SNA uptake is mainly mediated by class A scavenger receptors,[59,161] which recognize DNA. Because highly phagocytic cells in the liver are responsible for the sequestration of injected nanoparticles,[103,162,163] differences in accumulation of LNPs and SNAs in these cell types are likely the cause of these differences. We have previously observed sequence-dependent biodistribution with gold-based SNA structures. With the same poly(T) and G-rich DNA motifs used in this manuscript, we observed greater accumulation of SNAs with G-rich DNA sequences in the liver and spleen shortly after injection, as well as different proteins coating the nanoparticle surface[19,47]. To determine whether spleen-specific mRNA expression is dependent on the sequence present on the LNP-SNA surface, we compared poly(T) LNP-SNAs to G-rich LNP-SNAs. We observed spleen-specific mRNA expression only in the G-rich LNP-SNA structures (Figure 3.12), suggesting that this is a G-rich DNA specific effect (Figure 3.12).

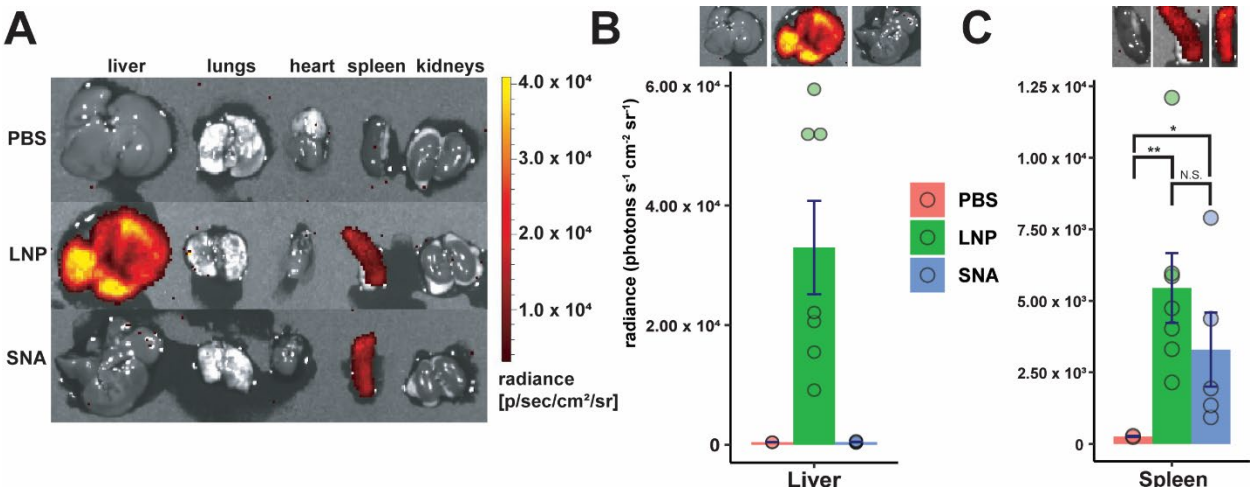

Figure 3.11 *LNP-SNAs effectively deliver mRNA with organ-specific function.* (A) Luc mRNA expression in major organs by treatment. Luminescence was detected in harvested organs 6 h after administration of 0.1 mg kg^{-1} Luc mRNA. (B, C) LNP-SNAs exhibit organ-specific

function in the context of mRNA expression. Luminescence was detected in harvested organs 6 h after administration of 0.1 mg kg^{-1} Luc mRNA. (one-tailed student's t-test, * = $p < 0.05$, each dot represents a biologically independent replicate, with 4-7 biologically independent replicates per treatment).

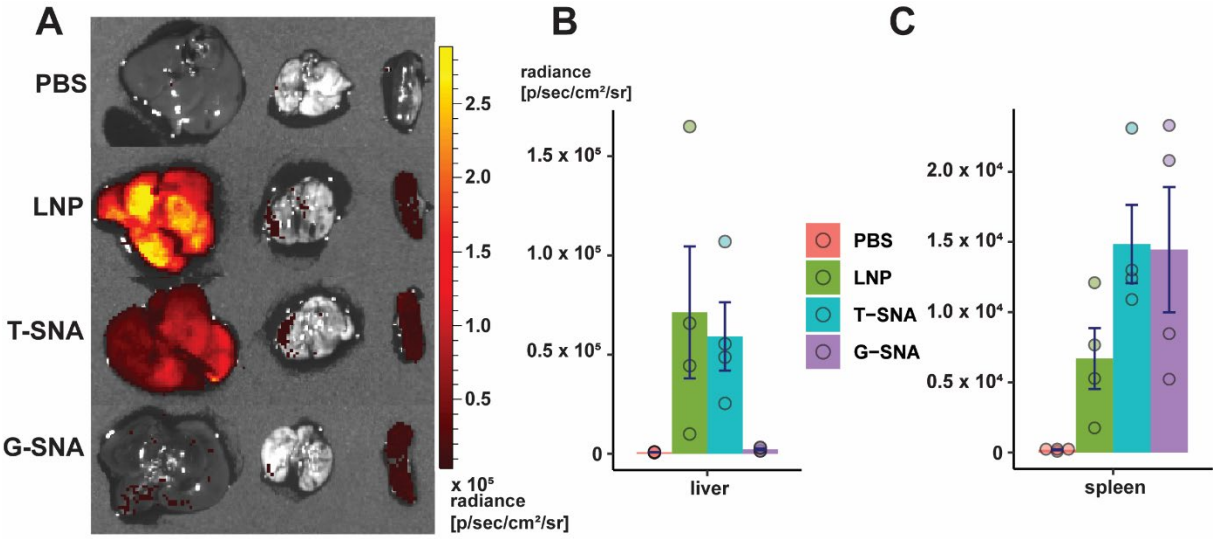

Figure 3.12 *LNP-SNA mRNA expression profile is sequence-dependent.*

(A) Luciferase mRNA in liver, lungs, and spleen by treatment. Luminescence was detected in harvested organs 6 h after administration of 0.1 mg kg^{-1} Luc mRNA. (B) LNP and T-SNA exhibit significant liver mRNA expression while G-SNA does not. (C) G-SNA exhibits mRNA expression in the spleen at levels comparable to LNP and T-SNA. (T-SNA is LNP functionalized with T21-SH DNA, G-SNA is LNP functionalized with (GGT)7-SH DNA sequence, N=4 biologically independent replicates).

3.4 Conclusion

Synthesizing LNP-SNAs with a library of different compositions allows for multivariate analysis of the effects of both sequence and lipid nanoparticle composition. We have observed

that both the surface-presented DNA sequence and the LNP composition determine activity of LNP-SNAs in cellular assays. From screening a series of LNP-SNA libraries, we determined that mol% cholesterol and DNA sequence were the two most important predictors of cytosolic delivery. While we initially screened libraries of LNP-SNA structures for activation of the cGAS-STING pathway mediated by dsDNA delivery, nanoparticles that were able to encapsulate dsDNA were also effective at delivering similarly-sized siRNA. Compared to the liposomal SNA,[44,45] LNP-SNAs demonstrated a 100-fold reduction in oligonucleotide concentration required to achieve gene silencing. In addition, LNP-SNAs increased gene silencing compared to the bare LNP with no DNA on its surface in cellular assays by 5%.

The optimized LNP-SNA formulations from *in vitro* screening were modified to encapsulate a larger, ~ 2kb mRNA encoding firefly luciferase (Luc). We identified a LNP-SNA formulation that was able to effectively encapsulate Luc mRNA while producing detectable mRNA expression in C57BL/6 mice. LNP-SNAs functionalized with G-quadruplex DNA exhibited organ-selective function in the spleen, while avoiding a high degree of off-target liver expression shown from the bare LNP. This effect is possibly due to the influence of G-quadruplexes on the proteins that adsorb to nanoparticle structures. We have previously observed that G-rich SNA structures have more total protein adsorbed to their surface, and the composition of the protein corona also changes.[62] This shift in the protein corona towards proteins such as factor H and C3b enhances uptake of G-quadruplex containing SNAs into macrophages in cellular assays.[63] As organs like the spleen contain many cell types that uptake materials via the complement pathway,[164,165] this may be partially responsible for this effect.

Organ-specific mRNA expression observed using LNP-SNAs bodes well for applications such as delivering a mixture of single-guide RNA (sgRNA) and mRNA coding for a base editor. Others have measured high levels of off-target edits in both RNA and DNA with base editors,[12,13,101] thus the use of a carrier with organ-specific activity may increase safety and efficacy. Specifically, targeting to the spleen has the potential to use mRNA for genome editing in important cell populations which regulate the immune response to pathologies such as cancers.[166] Future studies are necessary to elucidate the immune cell populations in which LNP-SNAs have greatest editing efficiency *in vivo*. We envision that the structure-dependent biodistribution and activity of LNP-SNAs may become a powerful tool to create safer and more efficacious genetic medicines.

3.5 Materials and Methods

3.5.1 Materials

DNA was synthesized using automated solid support phosphoramidite synthesis (model: MM12, BioAutomation, Inc.). Sequences were purified by reverse phase high-pressure liquid chromatography (HPLC, Agilent Technologies) and characterized using matrix assisted laser desorption ionization-time of flight (MALDI-ToF, Bruker Autoflex III). The DNA sequences used for experiments are listed in Table S1. Firefly luciferase mRNA was purchased from TriLink BioTechnologies.

DLin-MC3-DMA was purchased from MedChemExpress. DMPE-PEG(2000) Maleimide, DPPE-PEG(2000) Maleimide, and DSPE-PEG(2000) Maleimide were purchased from Nanocs, Inc. Cholesterol and Triton™-X-100 were purchased from Sigma. DOPC, DSPC, 18:1 DAP, and DOPE were purchased from Avanti Polar lipids, Inc. Lipofectamine™ 2000, Quant-iT™ PicoGreen™ dsDNA reagent, Quant-iT™ RiboGreen™ reagent, and 20X TE buffer

were purchased from ThermoFisher. D-Luciferin was purchased from Gold Biotechnologies, and Luc mRNA was purchased from TriLink Biotechnologies.

3.5.2 LNP-SNA Formulation

LNPs were formulated using the ethanol dilution method. Briefly, lipids and cholesterol were dissolved in 100% ethanol. dsDNA was dissolved in 10 mM citrate at pH 4.0 at a mass ratio of 5:1 ionizable lipid:dsDNA. After making both solutions, DNA was rapidly pipette mixed with the ethanol solution at a volume ratio of 3:1. After mixing, LNPs were dialyzed two times in a Pierce™ 3K MWCO microdialysis plate (ThermoFisher) for 60 min against 1X PBS. Then, LNPs were added to microcentrifuge tubes containing 1 equivalent of lyophilized thiol-terminated DNA sequences and shaken at 700 rpm at room temperature overnight to facilitate the reaction of maleimide-functionalized PEG lipids with sulfhydryl-terminated DNA.

3.5.3 LNP-SNA Characterization

LNP-SNAs size and nanoparticle concentration were determined by nanoparticle tracking analysis (NTA) using a Malvern NanoSight NS300 fitted with a NanoSight sample assistant. Nanoparticles were diluted 1:1000 in water and run through the microfluidics at 50 µL/min. Size was determined using the NTA software with a manually set detection threshold to avoid background. Encapsulation efficiency of dsDNA and RNA was determined by modified Quant-iT™ PicoGreen™ and Quant-iT™ RiboGreen™ (Invitrogen) assays, respectively. Briefly, two separate standard curves were created with the encapsulated nucleic acid. One was in 1X TE Buffer while the other contained 1X TE Buffer supplemented with 0.1% Triton™-X-100. Two samples were created from each nanoparticle, one diluted in TE and one diluted in TE with 0.1% Triton™-X-100. Following, 100 µL of 1X PicoGreen™ (dsDNA) or RiboGreen™ was added on top of the standards and samples and fluorescence of each sample was measured using a plate

reader. Concentration of free nucleic acids were determined from the TE standard curve and concentration of total nucleic acids was determined by the particles lysed in 0.1% Triton™-X-100. From this, the encapsulation efficiency was calculated from the following formula: (TritonX-[TE])/([TritonX]) or ([Total]-[Free])/([Total]).

3.5.4 Cellular assays to measure cGAS-STING pathway activation

The Raw 264.7- Lucia™ ISG cell line was purchased from Invivogen. For in vitro experiments, Zeocin™, Normocin™, and QUANTI-Luc™ were purchased from Invivogen. All cell lines were cultured according to the manufacturer's specifications. All cell lines were tested for Mycoplasma contamination and grown in a humidified atmosphere with 5% CO2 at 37 ºC.

The specified nanoparticle formulations and controls were diluted in Opti-MEM (Gibco) and plated in triplicate in a 96-well plate. Cell were then plated on top of the nanoparticle treatments at 100,000 cells per well. After a 24 h incubation, 20 µL of the media was removed and IRF3 induction was quantified using the Quanti-Luc™ reagent (Invivogen) according to the manufacturer's protocol. To normalize the number of viable cells to the amount of IRF3 induction we achieved, we used the PrestoBlue™ HS cell permeable viability reagent (Thermo Fisher). Next, additional media was removed such that the volume within the plate was 90 µL. 10 µL of PrestoBlue™ was added per well and the plates were incubated for 15 min, at which point the fluorescence was read according to the manufacturer's protocol. The IRF3 induction (luminescence) was then normalized to viable cells (PrestoBlue™ fluorescence) on a well-by-well basis.

3.5.5 LNP-SNAs delivering siRNA in cellular assays

U87-Luc2 cell lines were obtained from ATCC and cultured according to the manufacturer's specifications. To assess siRNA-mediated gene silencing, the top five LNP-SNA

candidates from the cGAS-STING pathways screening were formulated with siLuc2 and paired with control LNP-SNAs formulated with siGFP. Therefore, gene silencing could be read out as a decrease in luminescence due to silencing of Luc2.

The specified nanoparticle formulations and transfected siRNA controls were diluted in Opti-MEM (Gibco) and plated in triplicate in a 96-well plate. Cells were then plated on top of the nanoparticle treatments at 50,000 cells per well. After a 24 h incubation, 120 μL of the media was removed and 20 μL of CellTiter-Fluor™ reagent (Promega) was added to measure the number of viable cells within each well. After a 30 min incubation at 37 °C, fluorescence was read according to the manufacturer's protocol. Wells were subsequently washed with 100 μL of PBS three times. Luc2 luminescence was read using the Luciferase Assay System (Promega). Luc2 gene silencing was assessed in arbitrary units normalized to the CellTiter-Fluor™ viability.

3.5.6 Animal handling

Female mice (C57Bl/6) in the age range of 8-12 weeks were obtained from The Jackson Laboratory and maintained in conventional housing. All animals used were handled according to methods and procedures approved by the Institutional Animal Care and Use Committee at Northwestern University.

3.5.7 Luciferase (Luc2) mRNA expression

Cleancap® Luciferase mRNA was purchased from TriLink Biotechnologies. Mice were given a single bolus injection of 0.1 mg kg-1 of mRNA-containing formulations. After 6 h, mice were injected intraperitoneally with 150 mg kg-1 of D-luciferin. Animals were then sacrificed, and major organs were harvested and soaked in a 300 μg mL^{-1} solution of D-luciferin. Individual organs were then imaged using an IVIS Spectrum instrument (Perkin Elmer).

3.5.8 Statistical analysis

Design of Experiment (DoE) was used to create library designs A and B. DoE and statistical analysis were performed using R version 3.6.1 (cran.r-project.org) and JMP Pro 15. Descriptions of the DoE and statistical analysis are available in greater detail in section 4 of the Supporting Information. Statistical significance is defined as having a p-value of less than 0.05 in this study. All results are expressed as the mean ± SE and number of biological replicates (n) as noted in the figure captions. To design the 1st generation library, we used a definitive screening design to estimate the main and two-factor effects using less experimental runs. The factors used in Library A were: lipid-PEG Length, PEG mol %, chol. mol %, and ionizable lipid. For Library B, we used JMP to design a $3^3 2^2$ resolution IV fractional factorial design. The three-level factors used in Library B were phospholipid, PEG mol %, and chol mol %. The two-level factors used were PEG length and DNA sequence. Again, in this design, we were only interested in the main effects and first order interaction effects. Using a Custom Experiment Design on JMP, the minimum number of nanoparticles to run was 37 of the possible of the 108 full factorials. JMP software was used to plot the main effects and first order interaction effects in this experiment. To calculate the least squares regression model, we reduced the model until only significant main effects and first order interaction effects were included.

For mouse experiments, the free PS Power and Sample Size calculation tool Version 3.6.1 (Vanderbilt) was used to determine the minimum sample size for which the statistical power was greater than 0.8. This was generally 5-6 mice per group for Luc mRNA delivery experiment.

3.5.9 Discussion of DoE Optimization Process

With the initial selection of factors, we had a $2^2 3^2$ design. Because a full-factorial screening using this design would be 36 different nanoparticles, we used a definitive screening design (Jones and Nachtsheim) to estimate the main and two-factor effects using less experimental runs. In definitive screening experiments, unlike resolution III fractional factorial designs, the main effects are not confounded by two-factor interactions. Additionally, unlike resolution IV designs, two-factor interactions are not completely confounded with other two-factor interactions. These properties make it easier to move directly from screening to optimization. (For detailed descriptions of the creation and analysis of definitive screening and fractional factorial designs, we recommend the reader refer to the text *Design and Analysis of Experiments* (8^{th} ed.) by Douglas C. Montgomery.)

Following the use of a definitive screening design, we used a resolution IV fractional factorial design to perform further optimization. The base formulations were derived from the particles that exhibited significant IRF3 induction presented in Figure 2E. It is important to note that we used *coded* units instead of the *natural* or *engineering* units of each component. Coded units make the magnitude of the coefficients in the model directly comparable so that we can compare the relative size of factor effects, e.g., we can directly compare the effect size of changing percent cholesterol or changing percent PEG-lipid without the results being masked by large differences in engineering units.

3.5.10 Standard Least Squares Regression Model

A model describing all of the first and second-order effects was constructed using JMP. The program lists the effects of each parameter and second-order effect in the model as well as the LogWorth (-log10(FDR P-value)).

CHAPTER FOUR

4 DEFINING THE IN VIVO ACTIVITY AND DISTRIBUTION OF LNP-SNAS USED FOR MRNA DELIVERY

This chapter is based on unpublished work by: **Sinegra, A.J.**, Evangelopoulos, M.E., Mirkin, C.A.

4.1 Summary

While mRNA medicines show great promise due to the potential of expressing exogenous genes in cells, their applications require a carefully designed delivery vector to prevent their degradation, target their distribution in the body, and carry them into the cytoplasm of cells. Lipid nanoparticles (LNPs) are a highly modular delivery system with many interchangeable components. However, irrespective of their composition, their trafficking is thought to be limited to endogenous lipid trafficking mechanisms. Lipid nanoparticle spherical nucleic acids (LNP-SNAs) introduce DNA as a targeting ligand on the surface of LNPs to alter LNP trafficking. For example, a G-rich sequence on the surface of LNP-SNAs has been shown to increase specificity of mRNA expression by LNP-SNAs to the spleen. To benchmark LNP-SNA activity in the context of mRNA expression and genome editing *in vivo*, an approach using Cre mRNA was used. LNP-SNAs with encapsulated Cre mRNA exhibit (2-5%) editing efficiency in T-cells, B cells, and monocytes in the spleen while exhibiting very little background expression in the liver. To probe the mechanism underlying these properties, DNA barcoded LNP-SNAs were synthesized for sensitive and multiplexed detection of their biodistribution. LNP-SNAs distribute in greater amounts to highly phagocytic cells in the liver such as B cells and Kupffer cells than the corresponding LNP. These findings highlight that increased clearance of LNP-SNAs by cells with typically low transfection efficiency in the liver may cause their spleen specificity. The multiplexed assays presented demonstrate that the DNA on the surface LNP-SNAs may be used to tune their interactions with key cell types in the liver and spleen for increased specificity.

4.2 Introduction

Delivery of nucleic acids to organs other than the liver remains challenging. While development of antibody drug conjugates can potentially target around 15% of all proteins, siRNA and mRNA-based therapeutics may, in theory, target any mRNA or region of the genome present in the cell. Some of the most promising applications of RNA delivery are: siRNA to silence genes,[33,56,143,144] mRNA to replace mutated genes,[18,19] and mRNA sequences coding for genome editing agents to correct genetic diseases.[9–11] While RNA-based therapeutics possess the ability to change targets *via* simple changes in the nucleic acid sequence, creating nanoparticle carriers with predictable biodistribution and activity remains a hurdle to implementing them in the clinic.

In vitro assays are capable of predicting the nanoparticles' abilities to target hepatocytes,[167] but there is very little correlation between nanoparticle function in other cell types in cellular assays and their activity profiles in mice.[168] This lack of correlation between cellular assays and the distribution of nanoparticles after systemic administration (i.v. administration) is likely due to the lack of semblance to physiological blood flow, clearance by immune cells of the mononuclear phagocyte system (MPS),[30,31,139] and physiological barriers that disassemble nanoparticle structures.[141,169] Highly modular structures whose properties such as stability, charge, and size may be easily altered and screened *in vivo* present a change to use large data sets to elucidate structure-activity relationships.

Lipid nanoparticles (LNPs) which are have been used for FDA approved siRNA therapeutics[8] and the emergency authorized mRNA vaccines for SARS-CoV-2.[170] While LNPs present the advantages of efficient encapsulation of RNA of various lengths and escape from cell compartments,[16,90,171] the greatest advantages of these multicomponent systems is their

modularity. LNPs are typically comprised of four different classes of components: a phospholipid (helper lipid), a sterol, a lipid-PEG, and an ionizable lipid.[33] While these classes remain common to many LNPs in the literature, both the structures within each component class and their molar ratios may be tuned for delivery to different tissues and greater activity. However, while LNP structures are very modular, they are limited in trafficking without extensive modifications. It is hypothesized that they are taken up into hepatocytes after exchange in serum with ApoE, which mediates uptake *via* the LDL receptor.[57] In chapter 3, we demonstrated a strategy of forming LNP-SNAs, wherein a DNA sequences conjugated to the surface of LNPs may be used for targeting. Using luciferase mRNA delivery as a model system, we demonstrate that G-rich DNA sequences conjugated to a LNP increase activity in cellular assays as well as target the mRNA expression to the spleen. This initial study indicates that the distribution and activity of existing LNP structures may be programmed by conjugating DNA sequences to the surface. However, the mechanism of this specificity and scope of the versatility of programming distribution using DNA sequences is unclear.

With this complex design space afforded by LNP and LNP-SNA structures, optimization is necessary to find more potent structures[16] and those with greater delivery to the target cell.[93,95] Kauffman et al demonstrate that a Design of Experiment (DoE)-based optimization process can find LNPs with more than four-fold increase in activity compared to the original construct.[16] While this careful structure design finds improved structures, it is difficult to screen many different nanoparticle structures simultaneously *in vivo*, where all of the barriers to nanoparticle delivery are intact. The use of next-generation sequencing (NGS) assays to assess nanoparticle delivery to cells has enabled the screening of hundreds of nanoparticle structures simultaneously

in mice.[96] Indexing structures with DNA barcodes enables pooling of many different structures, injecting the pool into one animal, and reading of nanoparticle delivery using NGS. Especially when coupled with a functional readout, these techniques can be used to screen modular nanoparticle structures in wild-type animals where all the barriers to delivery are intact.

Here, we present a study designed to elucidate the cells and tissues that may be targeted by LNP-SNAs. Using both modified Ai14 C57BL/6 mice (Jackson Laboratories) and DNA barcoded nanoparticles, we investigated the cell populations in which LNP-SNAs achieve significant genome editing. Following, we sought to investigate the mechanism underlying the differences in activity profiles found between LNPs and LNP-SNAs in chapter 3. As mentioned, DNA barcoding strategies allow for the multiplexed detection of the biodistribution of many nanoparticles in one mouse. In this study, we present a DNA barcoding method to screen LNP-SNA structures for enhanced delivery to major cell types in the liver, spleen, and lungs.

4.3 Results and Discussion

To examine the genome editing capability of LNP-SNAs and the cells in which significant activity occurs, we employed C56BL6/J mice genetically modified with the Ai14 reporter allele (Figure 4.1A). In these mice, we were able to use expression of Cre recombinase RNA to demonstrate genome editing. The Ai14 allele contains the tdTomato (tdTom) fluorescent protein downstream of a stop cassette floxed by two LoxP sites. If Cre recombinase mRNA is successfully expressed, the tdTom is expressed, and genome editing in cell types may be assessed by flow cytometry. In chapter 3, we demonstrated that LNP-SNAs functionalized with a G-rich DNA sequence exhibited spleen-specific mRNA expression using luciferase mRNA as a model system. This system provided rapid whole-organ results, but lacked the single-cell resolution of the Ai14 mice.

Using commercially available magnetic cell separation kits designed for spleen cells (EasySep™, Stem Cell Tech, Inc.), we separated different major spleen cell types after injecting Ai14 mice with 0.3 mg kg^{-1} and waiting for 48 h. We were able to separate T cells, B cells, and monocytes in the spleen. Previous works indicate that B cells and monocytes in the spleen sequester the majority of nanoparticles in the organ.[28] After gating tdTom positive cells based on PBS control mice, we found that both the LNP and LNP-SNA exhibited low, but detectable levels of genome editing in major spleen cell types (Figure 4.1B). LNPs and SNAs achieve similar levels of editing in B cells, with 2.5 and 2.6 percent tdTom positive cells respectively. SNAs achieve higher levels of editing in monocytes with an average of 6.3% tdTom positive cells *versus* 2.2% positive cells with the LNP. In T cells, LNP achieves a higher level of genome editing, 5% positive cells, and 2.8% positive cells with the SNA.

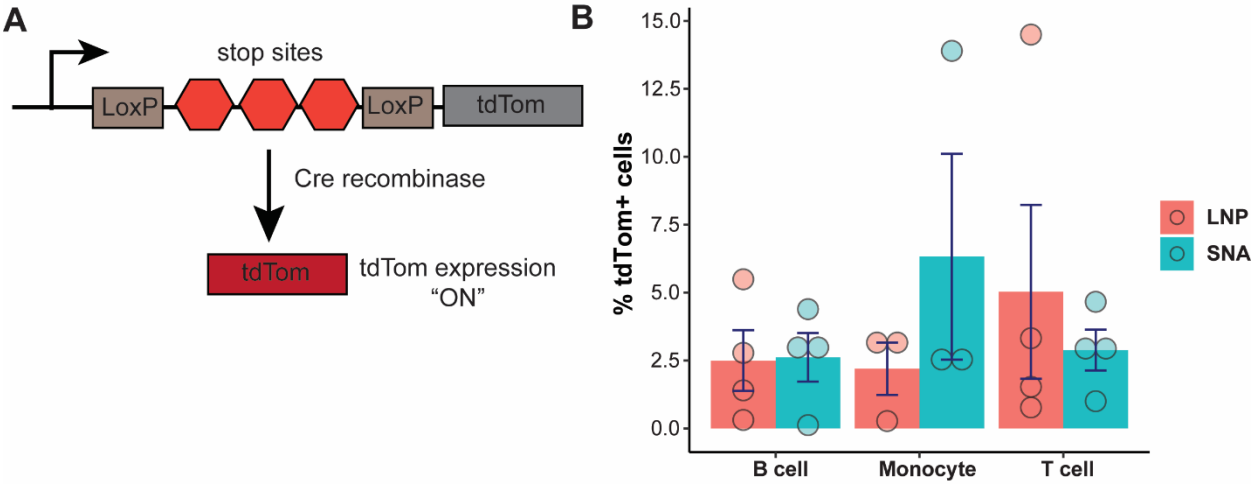

Figure 4.1 *Assays for cell population-level genome editing using Ai14 mice*. (A) Ai14 mice express tdTom downstream of a floxed STOP cassette. Expression of Cre recombinase removes the stop cassette, turning on tdTom expression. (B) Percent tdTom positive cell types in spleen

after treatment with either LNP or LNP-SNA containing Cre mRNA. (0.3 mg kg^{-1}, 48 h, N = 3-4 biologically independent replicates).

Following observing these small, but detectable, levels of genome editing in spleen cells we sought to determine whether mRNA expression levels in Ai14 mice would corroborate our findings in chapter 3, where we observed little detectable mRNA expression from LNP-SNAs in the liver. In the same mice as shown in Figure 4.1., we isolated livers, digested cells with collagenases, and stained important cell types for analysis using flow cytometry. We stained T cells with anti-CD3e, B cells with anti-CD19, endothelial cells with anti-CD31, and Kupffer cells with anti-CD68 and used the gating strategy developed by Chan et al.[28] The results corroborated our findings in chapter 3 as well as supported claims in the LNP literature on cells targeted by conventional LNPs. We observed a significant degree of tdTom positive cells in endothelial cells (11.9%), hepatocytes (31.2%), B cells (9.1%) in mice treated with the LNP (Figure 4.2A, B, C). This corroborates the large LNP literature, where most LNPs are able to achieve high activity in hepatocytes due to uptake *via* the LDL receptor.[57,90,167] We observed very little activity in Kupffer cells with the LNP (2.8%) (Figure 4.2D). The LNP-SNA formulation, as expected from chapter 3, did not achieve significant genome editing in either hepatocytes, B cells, or T cells. While SNAs achieved little function in liver cells, this does not indicate their degree of distribution in liver cells. We hypothesized that, while LNP-SNAs don't produce detectable luciferase or Cre mRNA expression in the liver, that they may still be distributing to the highly phagocytic cell types found there. Some of these cell types, like Kupffer cells, may be difficult to transfect with mRNA, limiting LNP-SNA activity in the liver.

In order to determine the distribution of LNPs and LNP-SNAs in a multiplexed fashion, we used the aforementioned barcoding strategy of Dahlman et al.[96] The procedure for these experiments is shown in Figure 4.3. LNPs and LNP-SNAs can be synthesized individually with different 59 nucleotide barcodes indexing each structure (Figure 4.3A, sequences in Table 4.1). Including a free control barcode validates that the barcodes detected are at above background levels, as the free barcode should be cleared faster from mice, resulting in fewer sequencing reads. Following injection of the pooled library, individual cell types can be isolated using FACS or magnetic separation and the barcode DNA is isolated and amplified (Figure 4.3D).

Table 4.1 *Barcode Sequences used in initial library*

barcode #	Sequence
1	A*G*A CGT GTG CTC TTC CGA TCT GAC ACA GT NNNNNNN AGA TCG GAA GAG CGT CGT*G*T
2	A*G*A CGT GTG CTC TTC CGA TCT GCA TAA CG NNNNNNN AGA TCG GAA GAG CGT CGT*G*T
3	A*G*A CGT GTG CTC TTC CGA TCT ACA GAG GT NNNNNNN AGA TCG GAA GAG CGT CGT*G*T
4	A*G*A CGT GTG CTC TTC CGA TCT CCA CTA AG NNNNNNN AGA TCG GAA GAG CGT CGT*G*T
5	A*G*A CGT GTG CTC TTC CGA TCT TGT TCC GT NNNNNNN AGA TCG GAA GAG CGT CGT*G*T
6	A*G*A CGT GTG CTC TTC CGA TCT GAT ACC TG NNNNNNN AGA TCG GAA GAG CGT CGT*G*T
7	A*G*A CGT GTG CTC TTC CGA TCT AGC CGT AA NNNNNNN AGA TCG GAA GAG CGT CGT*G*T
8	A*G*A CGT GTG CTC TTC CGA TCT CTC CTG AA NNNNNNN AGA TCG GAA GAG CGT CGT*G*T
9	A*G*A CGT GTG CTC TTC CGA TCT ACG AAT CC NNNNNNN AGA TCG GAA GAG CGT CGT*G*T
10	A*G*A CGT GTG CTC TTC CGA TCT AAT GGT CG NNNNNNN AGA TCG GAA GAG CGT CGT*G*T
11	A*G*A CGT GTG CTC TTC CGA TCT CGC TAC AT NNNNNNN AGA TCG GAA GAG CGT CGT*G*T

* = phosphorothioate backbone, N = random A,C,G, or T base (equal mixture)

After unsuccessful sequencing runs using a nested, two-step PCR protocol, we consolidated our amplification and indexing steps into one three primer PCR step (Figure 4.4A).

Here, a universal primer is used to amplify barcodes and two adapter index primers are used to add sequencer chemistry and index samples. To validate that indexed samples were present, we used a qPCR-based normalization kit. Importantly, before injecting the pooled LNPs and LNP-SNAs into mice, we characterized each nanoparticle in terms of size (Figure 4.4B) and encapsulation efficiency of the barcode sequence (Figure 4.4C). Sizes measured using nanoparticle tracking analysis ranged from ~100-210 nm. It is important in this step that each nanoparticle exhibits a monodispersed, stable size distribution, as mixing of different barcode sequences would confound sequencing results. Each nanoparticle exhibited similar encapsulation efficiency, between 85 and 90 percent, indicating there are similar orders of barcodes per nanoparticle.

Following sequencing runs, nanoparticle distribution is calculated within each sample on a relative basis. Nanoparticle reads are first normalized to their portion of the input, averaged by biological replicates, and then normalized within individual cell types. Unfortunately, several barcodes from our initial sequencing run did not have detectable readings from the input sample. Therefore, we could not normalize the data. This issue is likely due to nanoparticle instability. However, we did find a LNP and LNP-SNA pair that produced comparable read counts.

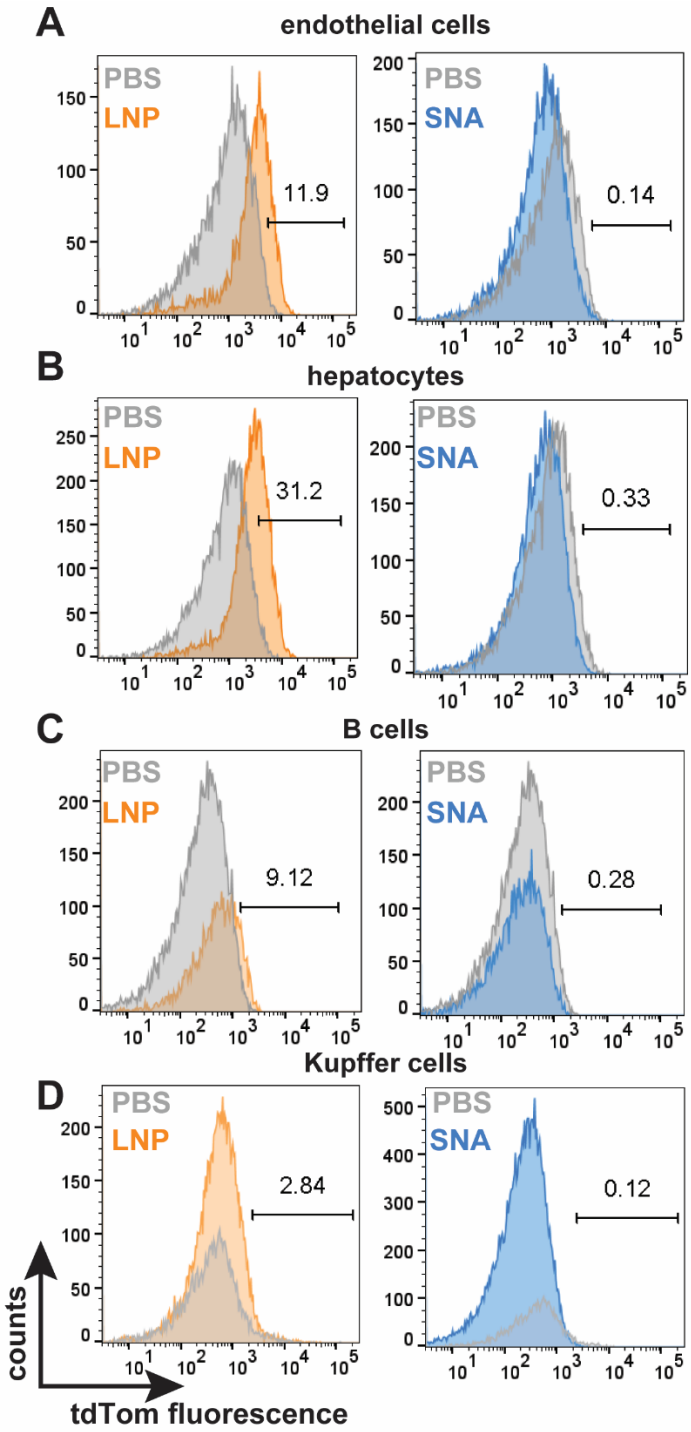

Figure 4.2 *Liver flow cytometry data of Ai14 mice 2 days after injection of 0.3 mg kg^{-1} Cre mRNA.* (A) determination of tdTom positive cells in endothelial cells. (B) tdTom positive cells in hepatocytes (C) tdTom positive cells in liver B cells (D) tdTom positive cells in Kupffer cells.

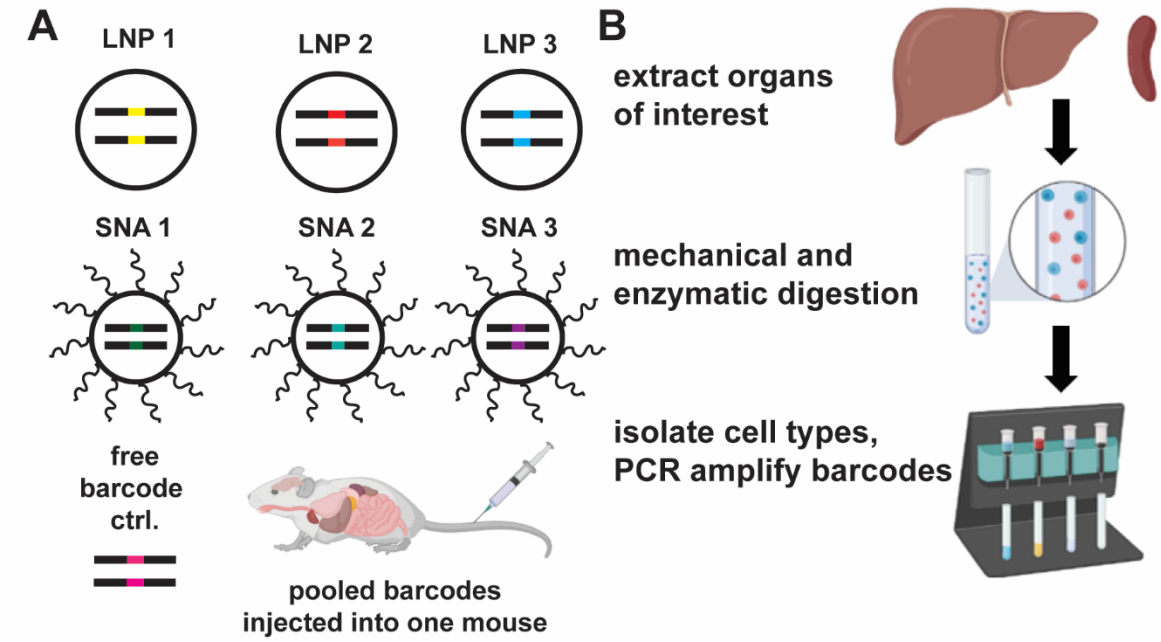

Figure 4.3 *Scheme of experimental procedure for nanoparticle barcoding*. (A) LNPs and SNAs are synthesized with a unique barcode encapsulated within the nanoparticle core to index each structure. A free barcode control (free barcode ctrl.) is included to ensure that read counts are above background. (B) Procedure for isolation of barcodes. Tissues of interest like the liver and spleen are isolated from mice 2 d after injection with NP pool. Tissues are mechanically and enzymatically digested to form single cell suspension. Finally, individual cell types are isolated using magnetic separation (shown) or FACS so that barcode delivery to individual cell populations can be assessed.

LNP-4 and LNP-SNA-4 produced data that we could analyze. Their formulations are similar to our initial formulation and are listed in Table 4.2. This LNP core is comprised of 21.5% DSPC, 25% cholesterol, 50% D-Lin-MC3-DMA, and 3.5% DMPE-PEG(200)-Maleimide.

The LNP-SNA is functionalized with a G-Rich DNA sequence. Here, we observed that LNP-SNA-4 achieved roughly 25% more delivery to major cell types in the liver and spleen that are responsible for the clearance of nanoparticles (Figure 4.4). First, this supported our hypothesis that LNP-SNAs do accumulate in liver cells, even though we observe no activity in luciferase mRNA expression or Cre-mediated genome editing (Figure 4.2). Second, LNP-SNAs accumulating in higher amounts in phagocytic cell types such as B cells and Monocytes supports claims of LSNAs we established in chapter 2 that SNA architecture allows for uptake *via* class A scavenger-receptor (SR-A) mediated endocytosis.[58,60,161,172] These cell types are known in the literature to express SR-A as well.[156,173,174] Finally, taken with data from Figure 4.2, where we observe low transfection efficiency in cells like Kupffer cells and B cells in the liver, we hypothesize that the lack of liver mRNA expression from LNP-SNAs in the liver may be due to entry into difficult-to-transfect cell types. Low editing efficiency, less than 25%, has been observed in these cell types in the liver in similar LNPs.[175]

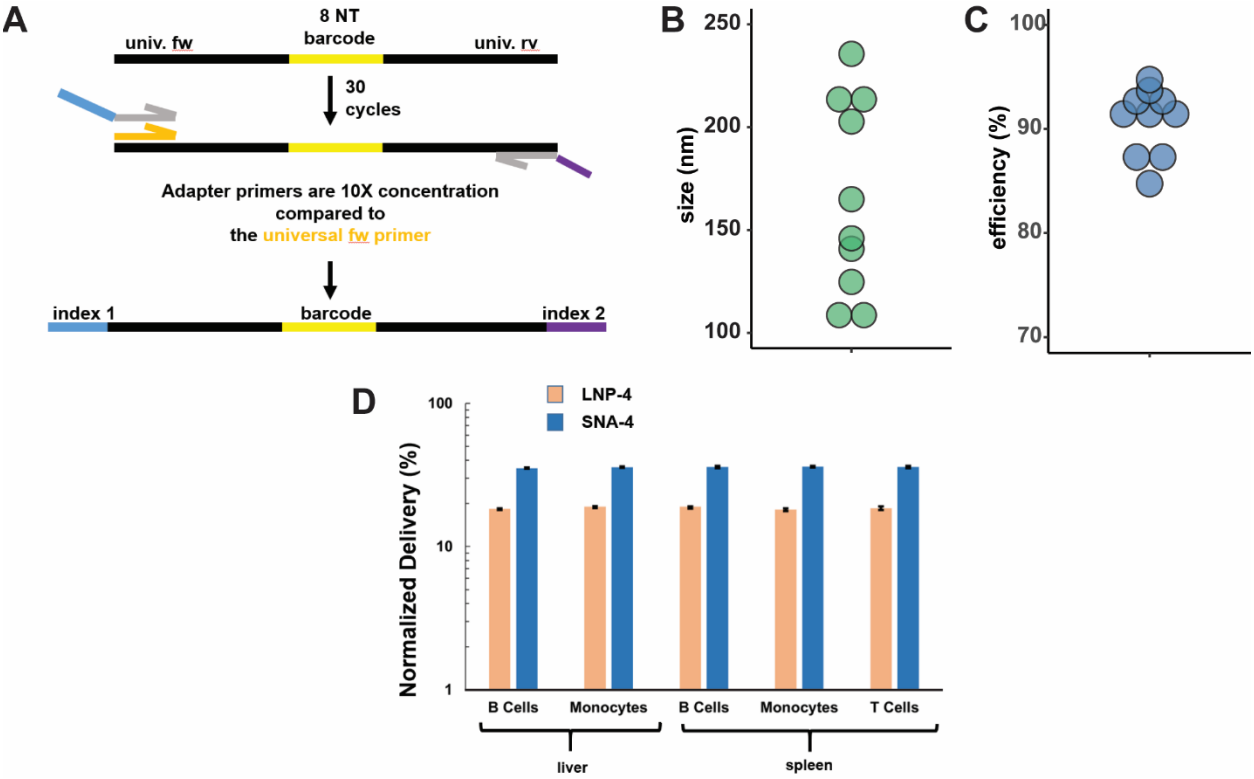

Figure 4.4 *Barcode Amplification Strategy and Example Result*. (A) Barcodes are isolated from cells using solid phase extraction columns, cleaned-up, and amplified using the following strategy. 3-primer PCR is performed with two sequencing adapter primers to impart Nextera XT chemistry (grey) and index samples (blue and purple), and one universal forward primer (gold). The reaction is run for 35 cycles with the indexing primers at 10-fold the concentration of the universal primer. (B) hydrodynamic size of each nanoparticle in an initial 10-nanoparticle library. (C) Barcode encapsulation efficiency of each nanoparticle in an initial 10-nanoparticle library. (D) Normalized delivery of LNP-4 vs. SNA-4 in major cell types in the liver and spleen.

Table 4.2 *Formulations used in LNP-SNA Barcode study*.

barcode #	phospholipid	% phospholipid	% chol	% D-Lin-MC3-DMA	% PEG-Mal	PEG_length	DNA Seq.
1	DOPC	24	25	50	1	C16	(GGT)7
2	DOPC	3.5	45	50	1.5	C16	(GGT)7
3	DOPE	2.5	45	50	2.5	**C16**	(GGT)7
4	DSPC	21.5	25	50	3.5	C14	(GGT)7
5	DOPC	1.5	45	50	3.5	C16	(GGT)7
6	DOPC	24	25	50	1	C16	NA
7	DOPC	3.5	45	50	1.5	**C16**	NA
8	DOPE	2.5	45	50	2.5	C16	NA
9	DSPC	21.5	25	50	3.5	**C14**	NA
10	DOPC	1.5	45	50	3.5	C16	NA

4.4 Conclusion

Taken with the results of chapter 3, we extend studies of mRNA expression *in vivo* using LNP-SNAs to include genome editing with Cre mRNA. Here, we find that we can achieve detectable levels of genome editing up to approximately 5% in Ai14 mice. In liver cells, we corroborate the findings of chapter 3, where LNP-SNAs did not exhibit significant activity in any major liver cell type. This spleen-specific activity profile is promising for applications in genome editing and base editing *in vivo* where high degrees of off-target editing have limited translation of promising nanocarriers into the clinic.[14,176] Further work using LNP-SNAs should quantify genome editing efficiency in a model gene in the spleen. Given we find low levels of detectable editing (2-5%), targeted next-generation sequencing based assays should be used to absolutely quantify indel frequency using Cas9 mRNA or base editing using a base editor mRNA.[177]

In Figure 4.4, we demonstrated that LNP-SNAs still accumulate in prominent liver cell types— even though we observe no detectable activity. While it is common to the literature that transfection efficiency is lower in phagocytic cells such as B cells and Kupffer cells,[30,175] further work using other LNP-SNA structures should be completed to determine whether the G-rich DNA confers this property across many LNP compositions. The DNA barcoding approach

demonstrated in Figure 4.4 shows promise to measure this effect across many LNP-SNAs differing by both core composition and DNA sequence. Besides G-rich DNA, many different aptamers and secondary structures have been used to target nanoparticles and may be used in the future to expand the scope of this work.[51,178]

4.5 Materials and Methods

4.5.1 Materials

DNA was synthesized using solid phase phosphoramidite synthesis (model: MM12, BioAutomation, Inc.). After synthesis completion, DNA sequences were deprotected and cleaved from solid support *via* a 20 min. incubation in AMA at 65°C. AMA was removed under a stream of nitrogen. Sequences were filter and purified by reverse phase high-performance liquid chromatography (RP-HPLC, Agilent Technologies) on a C18 column. Strands were characterized using matrix assisted laser desorption ionization-time of flight (MALDI-ToF, Bruker RapiFlex). The DNA sequences used for experiments are listed in Table S1. Strands synthesized on a 3'-Thiol-Modifier CpG were reduced before reacting with lipid-PEG-Maleimides in 100 mM DTT, pH 8.3-8.5 in TBE buffer

DLin-MC3-DMA was purchased from MedChemExpress. DMPE-PEG(2000) Maleimide, DPPE-PEG(2000) Maleimide, and DSPE-PEG(2000) Maleimide were purchased from Nanocs, Inc. Cholesterol and Triton™-X-100 were purchased from Sigma. DOPC, DSPC, and DOPE were purchased from Avanti Polar lipids, Inc. Lipofectamine™ 2000, Quant-iT RiboGreen™ reagent, and 20x TE buffer were purchased from ThermoFisher. Cre mRNA was purchased from Trilink Biotechnologies.

4.5.2 LNP-SNA Formulation

LNPs were formulated using the ethanol dilution method. Lipids and cholesterol were dissolved in 100% ethanol. dsDNA was dissolved in 10 mM citrate at pH 4.0 at a mass ratio of 20-40:1 total lipids:mRNA. After making both solutions, mRNA was rapidly pipette mixed with the ethanol solution at a volume ratio of 3:1. After mixing, LNPs were dialyzed two times in a PierceTM 3K MWCO microdialysis plate (ThermoFisher) for 60 min against 1X PBS. Then, LNPs were added to microcentrifuge tubes containing 1 equivalent of lyophilized thiol-terminated DNA sequences and shaken at 700 rpm at room temperature for two hours to facilitate the maleimide-sulfhydryl reaction between the lipids and DNA.

4.5.3 LNP-SNA Characterization

LNP-SNAs size and nanoparticle concentration were determined by nanoparticle tracking analysis (NTA) using a Malvern NanoSight NS300 fitted with a NanoSight sample assistant. Size was determined using the NTA software with a manually set detection threshold to avoid background. Encapsulation efficiency of mRNA was determined by a modified Quant-iT^{TM} RiboGreen^{TM} (Invitrogen) assay. The assay used two standard curves, one diluted in TE and one diluted in TE with 0.1% Triton^{TM}-X-100 to measure the concentration of free mRNA in intact nanoparticles (TE) versus the total mRNA concentration (0.1% Triton^{TM}-X-100).

4.5.4 Animal handling

Female mice (C57Bl/6J (#000664) and LSL-Tomato/Ai14 (#007914)) in the age range of 8-12 weeks were obtained from The Jackson Laboratory and maintained in conventional housing. All animals used were handled according to methods and procedures approved by the Institutional Animal Care and Use Committee at Northwestern University.

4.5.5 Cell isolation

Organs were harvested and incubated in a digestion mixture of 5000U/mL of collagenase I for 30 minutes at 37°C. Following, organs were chopped into small slices ~3 mm thick and pushed through 70 μm filters. Following, red blood cells were lysed using ACK lysis buffer for 5 min at RT (Thermo-Fisher) and cells were counted and resuspended in PBS containing 2.5% bovine serum albumin.

Cell types of interest derived from each organ were isolated using magnetic separation. Spleen macrophages and B-cells were isolated using EasySep™ kits (Stemcell™ Technologies). Liver B-cells were isolated using the identical EasySep™ kit. Hepatocytes were isolated *via* centrifugation at 200 x g.

4.5.6 DNA isolation and Next-Generation Sequencing

With cell types of interest, DNA was isolated using Clarity OTX™ columns (Phenomenex). The samples were lyophilized and cleaned using a PCR-Cleanup kit (New England Biolabs, Inc.). Following, nested PCR was performed according to previous protocols.[168] A universal primer was used to amplify barcode sequences, followed by adapter sequences used to index samples and add Nextera XT chemistry. Samples were sequenced using an Illumina NextSeq™.

4.5.7 Analysis of NGS data

Sequence files were analyzed using a custom R script. First, reads were preprocessed to filter out adapter primer sequences as well as reads shorter than 40 bases. Next, reads were processed so that there are no reads containing a quality score less than 20. Finally, each barcode was counted within each sample by searching for the reverse complement of the barcode sequence. With the number of reads of each barcode in each sample, the numbers were

normalized to the input. This is used to normalize the number of reads from each barcode to how many were originally injected. Following, delivery was quantified as “normalized delivery” or the percent of normalized reads from each barcode as a percentage of the total number of reads in the sample.

4.5.8 Statistical analysis

Statistical significance is defined as having a p-value of less than 0.05 in this study. All results are expressed as the mean ± SE and number of biological replicates (n) as noted in the figure captions. To design the 1st generation library, we used a definitive screening design to estimate the main and two-factor effects using less experimental runs

For mouse experiments, the free PS Power and Sample Size calculation tool Version 3.6.1 (Vanderbilt) was used to determine the minimum sample size for which the statistical power was greater than 0.8. This was generally 4-5 mice per group for Cre mRNA delivery to LSL-Tomato/Ai14 mice.

CHAPTER FIVE

5 SUMMARY, CONCLUSIONS, AND FUTURE WORK

This dissertation presents general approaches to evaluate the structures of nanoparticles, their interactions with barriers to delivery, and optimizing their structures for activity *in vivo*. In chapter 2, I described an approach to use nanoparticles with different release rates of the nucleic acid cargo to target their delivery to specific organs and cells.[145] In chapter 3, I expanded the utility of SNA structures to lipid nanoparticle structures designed to deliver cargo to the cytoplasm of cells. Finally, in chapter 4, I combined the structure-function relationships we developed with the original lipid nanoparticle spherical nucleic acids with single-cell resolution of genome editing function as well as a DNA barcoding method to evaluate many different structures at once. In this section, I will describe the future directions of aspects of these research areas.

5.1 Structure-dependent distribution of degradable SNAs

The study I presented on the structure-dependent biodistribution of liposomal spherical nucleic acids illustrated that a hydrophobic nanoparticle [liposome] can be used as a template for the delivery of nucleic acids modified on one end with a hydrophobic anchor. The study compared a 16-carbon diacyl lipid anchor to a cholesterol-triethylene glycol anchor. Future directions of this work will determine the mechanism underlying differences in distribution observed with increasing LSNA stability. While the release rate differences we observed between oligos in serum may be a driver of changes in distribution, other interactions in the body likely include affinity to serum proteins such as albumin, apolipoproteins, and immunoglobulins. *In vitro* measurements of different DNA-lipid or DNA-sterol conjugates and LSNAs may shed light on the mechanism underlying differences in distribution. In addition to studying the mechanism of distribution and clearance of LSNAs, a functional readout could be attached to biodistribution studies. As we have indicated previous activity of ASOs when formulated into

LSNA structures,[44] evaluating their activity in major organs outside of the liver where I observed accumulation, such as the lungs, liver, kidneys, and spleen,[145] will provide greater motivation for modulating the distribution of ASOs or siRNA using LSNA structures.

5.1.1 Future direction: expanding this study: analysis of protein corona of LSNAs

A possible explanation for different distributions of LSNA structures is that the protein corona on the surface of the particles differs by DNA conjugation chemistry to the liposome core. The protein corona of nanoparticles is largely responsible for their distribution into many organs as well as their clearance.[179,180] While the protein corona of AuSNAs has been studied, establishing the effect of DNA on the protein corona of soft nanoparticle-based SNAs such as liposomes, lipid nanoparticles, and PLGA may give important insights into their mechamisms *in vivo*. Often, establishing the protein coronae of soft nanomaterials involves more complicated approaches than simple pull-down assays. Mohammed-Beigi et al presented a click chemistry based approach to measure both the hard corona and soft corona on softer nanomaterials.[181] In this approach, the soft corona proteins, which have slightly less affinity for the nanoparticle surface than the hard corona proteins, are functionalized with a strained alkyne-terminated linker. Following, the hard corona proteins, which are still on the nanoparticle, are functionalized with an azide linker. When the soft corona proteins are reintroduced to the nanoparticle, the copper-free click reaction of azides to the alkynes can trap the more transiently bound soft corona proteins on the nanoparticle surface for analysis. While we expect the protein corona of LSNAs to be enriched in proteins such as complement C3b with G-rich SNAs,[62] there is great opportunity to both find differences in low-quantity "soft corona" proteins by DNA sequence as well as determine whether the rules established by Chinen et al[63] with AuSNAs apply to softer cores.

5.1.2 Future direction: measuring the affinity of lipid-DNA conjugates for major serum proteins

Abundant serum proteins such as albumin are useful for transporting drugs throughout the body, extending half-life and distribution to important organs.[182] With systems like the LSNA, I hypothesize that some of the effects of DNA anchor on distribution may be due to differences in affinity of each DNA sequence to albumin and other major serum proteins. While the release rate measurements of DNA from LSNAs using FRET have involved albumin, the affinities of these free conjugates to albumin and other important proteins found on SNAs such as apolipoproteins and complement proteins[63] have not been measured.

Recent research with soft nanomaterials highlights that simple measurements of a nanoparticle's affinity for a protein may provide a possible mechanism for an effect like the one we observe with LSNAs. A potential method we could use to assess the affinity of cholesterol or lipid-terminated DNA for a protein is quartz crystal microbalance (QCM).[183] QCM can be used to compare the affinity of proteins and nanoparticles to coated surfaces by measuring a frequency shift upon adsorption. In the case of our modified DNA sequences, I envision that we could coat the QCM with different proteins such as albumin, ApoE, or C3b and compare frequency shifts between chol-tail DNA and lipid-tail DNA as well as these same hydrophobic modifications with different DNA sequences. These types of experiments, as well as possible protein corona studies, could give us insight on both what proteins bind the intact LSNAs as well as what carries the free DNA once it is released from the nanoparticle.

5.2 **Lipid nanoparticle spherical nucleic acids for intracellular DNA and RNA delivery**

5.2.1 Future direction: delivering therapeutically-relevant mRNA for absolute quantification

In chapter 3, I presented a study on how we can use the delivery properties of SNAs to re-target existing lipid nanoparticles for applications such as DNA, siRNA, and mRNA delivery. While this is a promising proof-of-concept study illustrating that the delivery advantages we have found with other nanoparticle cores also apply to lipid nanoparticles, further work should be done to explore more DNA structures on the surface of LNPs as well as benchmark activity in more therapeutically relevant models. An advantage of the LNP-SNA over lipidoid nanoparticle or lipid nanoparticle systems is that the DNA on the surface of the particle is easier to synthesize and can form more predictable structures than unnatural synthetic lipids. In my work, we compared poly(T) and G-rich DNA sequences, however, more structures such as aptamers and other secondary structures may present opportunities to change LNP-SNA tropism further. In more therapeutically relevant applications, LNP-SNAs should be used to deliver an mRNA output which has an absolute value that may be used for quantification. For example, since I observed spleen-specific mRNA expression from LNP-SNAs functionalized with a G-rich DNA sequence, an mRNA coding for a protein relevant to the spleen may be delivered with the SNA. An example of this would be the anti-inflammatory cytokine IL-10 which is largely produced in the spleen.[184] A LNP-SNA can be formulated with encapsulated mRNA for IL-10, injected into a wild-type mouse, and IL-10 expression can be quantified in the serum. If IL-10 expression increases are detected in the serum, this study would demonstrate therapeutically relevant delivery of mRNA using LNP-SNAs.

5.2.2 Future direction: expanding analysis of DNA secondary structures' effects on organ-specific mRNA expression

While the studies in chapters 3 and 4 indicate that DNA sequences on the surface of LNP-SNAs may be used for changing their activity in mice, there is great potential for

investigating other DNA sequences which may be used to enter different cell types, respond to different conditions, as well as enhance activity. In chapter 3, I compared a Poly-T DNA sequence with a G-rich DNA sequence which forms a G-quadruplex secondary structure.[62] While only G-rich DNA sequences give LNP-SNAs spleen-specific activity, it is still unknown whether this is specific to G-quadruplex forming secondary structures or just G-rich DNA sequences. A method to test this would be to include a G-rich scramble sequence that contains the same number of G bases without this secondary structure.

In addition to testing the specificity of G-quadruplex structures, known aptamer sequences can be tested on the surface of LNP-SNAs. One promising aptamer is the transferrin aptamer (TfR), which binds transferrin and enhances accumulation of the associated DNA sequences in the brain.[178] Other stimuli-responsive sequences such as iMotif DNA[185] and cleavable DNA-PEG conjugates[71] may be interesting to test on the surface of LNP-SNAs. iMotif DNA, forms a secondary structure of cytosine base pairs in low pH environments. Cleavable DNA has been used to increase the uptake of SNAs into tumors, as DNA is cleaved by enzymes present in the tumor microenvironment. The versatility and cost-effectiveness of DNA conjugates as opposed to proteins and antibody fragments should be leveraged to create the next generation of LNP-SNAs.

5.2.3 Future direction: gaining insight into LNP-SNA structures and their interactions with cells

While the effects of adding DNA to the surface of LNPs for enhanced targeting are promising, little is known about the dynamics of DNA on the surface of the LNP. There are a few different experiments that could be used to probe the DNA exchange between particles and proximity of different DNA strands to each other on the LNP surface. First, we previously

compared the release rate of DNA strands from liposomes using FRET-based assays.[131] In these experiments, we take a nanoparticle labeled with small amount of fluorescent lipid as well as a DNA sequence forming a FRET pair on the surface. If these FRET SNAs are mixed with an excess of other SNAs or 10% serum, we are able to measure the release of the FRET acceptor (DNA) by decrease in the FRET ratio. If these experiments are run with proper controls, a positive control FRET-paired DNA sequence and a negative control where the particles are lysed so they no longer exhibit FRET, I envision that we could compare the release rate of DNA on the surface of LNPs with other SNAs, such as liposomal SNAs.

Another important dynamic which may affect the activity of LNP-SNAs in cells is the arrangement of DNA on the LNP surface. Whether different LNP-SNA structures form evenly dispersed DNA on the surface or lipid rafts of closely arranged DNA sequences may underlie engagement with receptors on the surface of cells such as scavenger receptors. Peruzzi et al present an interesting study wherein complimentary DNA sequences are used to enhance the fusion of liposomes.[186] In this study, the authors demonstrate that vesicles are more likely to fuse if the DNA arranged on their surface is more phase segregated. To probe this using LNP-SNAs, similar assays could be used. First, lipid mixing assays, usually based on FRET, could be used to demonstrate that different LNP-SNA structures are more likely to fuse with model lipid membranes. In addition, giant LNP-SNAs (of several microns in size), could be formed and imaged to determine the spatial arrangement of the DNA on their surface. Like formation of giant unilamellar vesicles (GUVs), imaging of large LNP structures or similar structures could allow us to gain insight into what compositions phase segregate DNA on the surface of LNP-SNAs and which evenly disperse the DNA.

5.2.4 Future direction: probing cellular uptake and endosomal escape simultaneously

Because LNP-SNAs can efficiently encapsulate DNA and RNA, we can use this ability to deliver DNA-based probes to assess how different DNA sequences on the surface of LNP-SNAs affect uptake into different cell lines and gain a functional readout simultaneously. Using a similar strategy to Samanta et al,[51] we can use forced intercalation (FIT) probes to assess the DNA binding to a target in the cytosol of cells such as mRNA while also delivering a normalizing dye to measure uptake of the LNP-SNA. In this case, we can assess LNP-SNAs' gene silencing potential normalized to how many NPs enter the cell. Properly designed experiments in this case would use a scrambled FIT probe designed to bind very few mRNA sequences and measure the background signal as well as a transfected or electroporated targeting sequence to assess the maximum possible signal.

While function in cell lines is not very predictive of activity in cells other than hepatocytes *in vivo*, these studies can be used to assess the mechanism of LNP-SNA uptake, which we anticipate remains via SR-A mediated endocytosis.[58,172] To assess this, the study above can be repeated using SR-A inhibitors. In addition, this study would give insight into the cell-line dependence of LNP-SNA uptake and escape from cell compartments if the same experiment is repeated in many relevant cell lines. This will be useful especially in the context of explaining spleen-specific mRNA delivery, where LNP-SNAs likely enter many major liver cell types, but do not escape from their cell compartments. This FIT probe assay should be performed in major liver cell types as well as spleen cell types such as splenic macrophages, B cells, and T cells to assess the underlying mechanism of my observations in chapter 3.

5.3 Studying the relationship of LNP-SNA structures to their biodistribution and activity in high-throughput

In chapter 3, I demonstrated that LNP-SNA distribution and activity depends on both LNP composition and the DNA sequence conjugated to the LNP surface. An important research avenue following this work is to determine the extent of LNP formulations to which this principle applies. Chapter 3 illustrates that the activity profile of one formulation can be altered using a G-rich DNA sequence and is not altered with a poly(T) sequence. In the LNP literature, there are many examples of altering LNP structures in order to achieve higher delivery to cells other than hepatocytes.[95,135,187] With this in mind, I believe the logical next direction of this research is to study how different DNA sequences affect biodistribution and activity of LNP-SNAs across LNP core structures. In chapter 4, I describe the beginning of this process using DNA barcoded LNP-SNAs to compare biodistribution in a high-throughput and multiplexed fashion. A limitation of this method is that it is difficult to couple distribution studies to In the future, genetically engineered animals may be used to screen both function and distribution of libraries of LNP-SNAs. Mice such as (Ai14) mice with a LoxP flanked STOP cassette could allow for multiplexed screening of genome editing LNP-SNAs. For example, a library of barcoded LNP-SNAs may be formed with encapsulated Cas9 mRNA and sgRNA targeting the tdTomato STOP cassette. Cells which are positive for tdTomato fluorescence indicate that a LNP-SNA or multiple SNAs are functioning in that cell type and can be isolated using FACS. Following, barcodes can be isolated and sequenced. Each nanoparticle's contribution to genome editing activity can then be calculated using normalization methods.[93,95]

Following this type of screening experiment, both the on-target and off-target genome editing efficiency should be quantified by targeting a model gene. For example, in chapter 3, I

described a LNP-SNA with near spleen-exclusive mRNA expression. While this is useful for gene replacement in the spleen, this is perhaps more promising for delivering mRNA coding for a base editor, where off-target effects are of great concern.[12,13] Commercially available assays which leverage NGS technologies may be useful for this purpose. An example would be rhAmpSeq™ available from IDT, Inc. wherein custom probes can be designed to sequence the sgRNA's target site as well as several of the most likely off-target sites. With LNP-SNAs exhibiting spleen-exclusive mRNA expression, this type of assay should be used after isolating cells from major organs such as the spleen, liver, and lungs to determine the off-target editing efficiency with great sensitivity.

5.3.1 Future direction: using large data sets to evaluate modular nanoparticle structures

In chapters 3 and 4 I demonstrated that evaluating many different structures helps in both optimizing function as well as learning about a nanoparticle's interaction with physiological barriers to delivery. Advances in DNA and RNA sequencing, proteomics, and high-throughput assay design, while useful to study biology, should be leveraged to understand the nano-bio interface. Initial studies with AuNP-based SNAs have laid the groundwork for further work. For example, sequence-dependent effects on SNAs' protein corona have been evaluated.[62,63] Similar work comparing LNPs' protein corona with LNP-SNAs may validate the hypothesis that LNP-SNAs do not function in hepatocytes because of less ApoE adsorption.[57] Advances in other omics-based methods could help to describe nanoparticle delivery as a complex phenotype.[188] As SNA uptake has been described as *via* Class A scavenger receptors in a lipid-raft, cavelolin-dependent manner, further lipidomics studies could also inform how SNAs interact with cells enriched in different lipid structures. Finally, RNA sequencing methods, especially on the single

cell level, have the potential to inform how SNAs affect the cell's machinery compared to other nanoparticle structures.

With large data sets, more advanced methods of analysis including dimensional reduction and machine learning can assist our understanding of the complex data sets generated by omics methods. For example, unsupervised clustering of RNA-seq data sets from different nanoparticle treatments of cells could elucidate which nanoparticle features create similar responses in the cell.[189] Machine learning methods can assist in making important predictions regarding nanoparticle structures. Machine learning methods such as random forests have been used to predict which peptide nanoparticles will form stable structures[190] as well as predict a pulmonary immune response to nanoparticle delivery.[191] The future of nanoparticle drugs depends on exploring a large design space, understanding biological barriers, and our ability to create methods to accurately predict activity and distribution.

6 REFERENCES

(1) Fire, A.; Xu, S.; Montgomery, M. K.; Kostas, S. A.; Driver, S. E.; Mello, C. C. Potent and Specific Genetic Interference by Double-Stranded RNA in Caenorhabditis Elegans. *Nature* **1998**, *391* (6669), 806–811. https://doi.org/10.1038/35888.

(2) Lee, Y. S.; Nakahara, K.; Pham, J. W.; Kim, K.; He, Z.; Sontheimer, E. J.; Carthew, R. W. Distinct Roles for Drosophila Dicer-1 and Dicer-2 in the SiRNA/MiRNA Silencing Pathways. *Cell* **2004**, *117* (1), 69–81. https://doi.org/10.1016/S0092-8674(04)00261-2.

(3) Elbashir, S. M.; Harborth, J.; Lendeckel, W.; Yalcin, A.; Weber, K.; Tuschl, T. Duplexes of 21-Nucleotide RNAs Mediate RNA Interference in Cultured Mammalian Cells. *Nature* **2001**, *411* (6836), 494–498. https://doi.org/10.1038/35078107.

(4) Tuschl, T.; Zamore, P. D.; Lehmann, R.; Bartel, D. P.; Sharp, P. A. Targeted MRNA Degradation by Double-Stranded RNA in Vitro. *Genes Dev.* **1999**, *13* (24), 3191–3197. https://doi.org/10.1101/gad.13.24.3191.

(5) Stephenson, M. L.; Zamecnik, P. C. Inhibition of Rous Sarcoma Viral RNA Translation by a Specific Oligodeoxyribonucleotide. *Proc. Natl. Acad. Sci. U. S. A.* **1978**, *75* (1), 285–288. https://doi.org/10.1073/pnas.75.1.285.

(6) Bartlett, D. W.; Davis, M. E. Insights into the Kinetics of SiRNA-Mediated Gene Silencing from Live-Cell and Live-Animal Bioluminescent Imaging. *Nucleic Acids Res.* **2006**, *34* (1), 322–333. https://doi.org/10.1093/nar/gkj439.

(7) Kole, R.; Krainer, A. R.; Altman, S. RNA Therapeutics: Beyond RNA Interference and Antisense Oligonucleotides. *Nature Reviews Drug Discovery*. Nat Rev Drug Discov February 2012, pp 125–140. https://doi.org/10.1038/nrd3625.

(8) Pharmaceuticals, A. Our Products: Approved for Use in the United States

https://www.alnylam.com/our-products/.

(9) Doudna, J. A.; Charpentier, E. The New Frontier of Genome Engineering with CRISPR-Cas9. *Science*. American Association for the Advancement of Science November 2014, p 1258096. https://doi.org/10.1126/science.1258096.

(10) Wang, H. X.; Li, M.; Lee, C. M.; Chakraborty, S.; Kim, H. W.; Bao, G.; Leong, K. W. CRISPR/Cas9-Based Genome Editing for Disease Modeling and Therapy: Challenges and Opportunities for Nonviral Delivery. *Chemical Reviews*. American Chemical Society August 2017, pp 9874–9906. https://doi.org/10.1021/acs.chemrev.6b00799.

(11) Sander, J. D.; Joung, J. K. CRISPR-Cas Systems for Editing, Regulating and Targeting Genomes. *Nature Biotechnology*. Nature Publishing Group 2014, pp 347–350. https://doi.org/10.1038/nbt.2842.

(12) Rees, H. A.; Liu, D. R. Base Editing: Precision Chemistry on the Genome and Transcriptome of Living Cells. *Nature Reviews Genetics*. Nature Publishing Group December 1, 2018, pp 770–788. https://doi.org/10.1038/s41576-018-0059-1.

(13) Grünewald, J.; Zhou, R.; Garcia, S. P.; Iyer, S.; Lareau, C. A.; Aryee, M. J.; Joung, J. K. Transcriptome-Wide off-Target RNA Editing Induced by CRISPR-Guided DNA Base Editors. *Nature* **2019**, *569* (7756), 433–437. https://doi.org/10.1038/s41586-019-1161-z.

(14) Rosenblum, D.; Gutkin, A.; Dammes, N.; Peer, D. Progress and Challenges towards CRISPR/Cas Clinical Translation. *Advanced Drug Delivery Reviews*. Elsevier B.V. January 1, 2020, pp 176–186. https://doi.org/10.1016/j.addr.2020.07.004.

(15) Cheng, Q.; Wei, T.; Farbiak, L.; Johnson, L. T.; Dilliard, S. A.; Siegwart, D. J. Selective Organ Targeting (SORT) Nanoparticles for Tissue-Specific MRNA Delivery and

CRISPR-Cas Gene Editing. *Nat. Nanotechnol.* **2020**, 1–8. https://doi.org/10.1038/s41565-020-0669-6.

(16) Kauffman, K. J.; Dorkin, J. R.; Yang, J. H.; Heartlein, M. W.; Derosa, F.; Mir, F. F.; Fenton, O. S.; Anderson, D. G. Optimization of Lipid Nanoparticle Formulations for MRNA Delivery in Vivo with Fractional Factorial and Definitive Screening Designs. *Nano Lett.* **2015**, *15* (11), 7300–7306. https://doi.org/10.1021/acs.nanolett.5b02497.

(17) Kowalski, P. S.; Rudra, A.; Miao, L.; Anderson, D. G. Delivering the Messenger: Advances in Technologies for Therapeutic MRNA Delivery. *Molecular Therapy*. Cell Press April 10, 2019, pp 710–728. https://doi.org/10.1016/j.ymthe.2019.02.012.

(18) Hajj, K. A.; Whitehead, K. A. Tools for Translation: Non-Viral Materials for Therapeutic MRNA Delivery. *Nature Reviews Materials*. Nature Publishing Group September 2017, pp 1–17. https://doi.org/10.1038/natrevmats.2017.56.

(19) Sahin, U.; Karikó, K.; Türeci, Ö. MRNA-Based Therapeutics-Developing a New Class of Drugs. *Nature Reviews Drug Discovery*. Nature Publishing Group January 2014, pp 759–780. https://doi.org/10.1038/nrd4278.

(20) Motwani, M.; Pesiridis, S.; Fitzgerald, K. A. DNA Sensing by the CGAS–STING Pathway in Health and Disease. *Nature Reviews Genetics*. Nature Publishing Group November 2019, pp 657–674. https://doi.org/10.1038/s41576-019-0151-1.

(21) Ishii, K. J.; Coban, C.; Kato, H.; Takahashi, K.; Torii, Y.; Takeshita, F.; Ludwig, H.; Sutter, G.; Suzuki, K.; Hemmi, H.; Sato, S.; Yamamoto, M.; Uematsu, S.; Kawai, T.; Takeuchi, O.; Akira, S. A Toll-like Receptor-Independent Antiviral Response Induced by Double-Stranded B-Form DNA. *Nat. Immunol.* **2006**, *7* (1), 40–48.

https://doi.org/10.1038/ni1282.

(22) Stetson, D. B.; Medzhitov, R. Recognition of Cytosolic DNA Activates an IRF3-Dependent Innate Immune Response. *Immunity* **2006**, *24* (1), 93–103. https://doi.org/10.1016/j.immuni.2005.12.003.

(23) Kim, E.; Yang, J.; Park, J.; Kim, S.; Kim, N. H.; Yook, J. I.; Suh, J. S.; Haam, S.; Huh, Y. M. Consecutive Targetable Smart Nanoprobe for Molecular Recognition of Cytoplasmic MicroRNA in Metastatic Breast Cancer. *ACS Nano* **2012**, *6* (10), 8525–8535. https://doi.org/10.1021/nn300289u.

(24) Park, Y. K.; Jung, W. Y.; Park, M. G.; Song, S. K.; Lee, Y. S.; Heo, H.; Kim, S. Bioimaging of Multiple PiRNAs in a Single Breast Cancer Cell Using Molecular Beacons. *Medchemcomm* **2017**, *8* (12), 2228–2232. https://doi.org/10.1039/c7md00515f.

(25) Ke, G.; Wang, C.; Ge, Y.; Zheng, N.; Zhu, Z.; Yang, C. J. L -DNA Molecular Beacon: A Safe, Stable, and Accurate Intracellular Nano-Thermometer for Temperature Sensing in Living Cells. *J. Am. Chem. Soc.* **2012**, *134* (46), 18908–18911. https://doi.org/10.1021/ja3082439.

(26) Ohlson, M.; Sörensson, J.; Haraldsson, B. Glomerular Size and Charge Selectivity in the Rat as Revealed by FITC-Ficoll and Albumin. *Am. J. Physiol. Physiol.* **2000**, *279* (1), F84–F91. https://doi.org/10.1152/ajprenal.2000.279.1.F84.

(27) Chang, R. L.; Ueki, I. F.; Troy, J. L.; Deen, W. M.; Robertson, C. R.; Brenner, B. M. Permselectivity of the Glomerular Capillary Wall to Macromolecules. II. Experimental Studies in Rats Using Neutral Dextran. *Biophys. J.* **1975**, *15* (9), 887–906. https://doi.org/10.1016/S0006-3495(75)85863-2.

(28) Tsoi, K. M.; MacParland, S. A.; Ma, X.-Z.; Spetzler, V. N.; Echeverri, J.; Ouyang, B.; Fadel, S. M.; Sykes, E. A.; Goldaracena, N.; Kaths, J. M.; Conneely, J. B.; Alman, B. A.; Selzner, M.; Ostrowski, M. A.; Adeyi, O. A.; Zilman, A.; McGilvray, I. D.; Chan, W. C. W. Mechanism of Hard Nanomaterial Clearance by the Liver. *Nat. Mater.* **2016**, *15* (11), 1212. https://doi.org/10.1038/NMAT4718.

(29) Alexis, F.; Pridgen, E.; Molnar, L. K.; Farokhzad, O. C. Factors Affecting the Clearance and Biodistribution of Polymeric Nanoparticles. *Mol. Pharm.* **2008**, *5* (4), 505–515. https://doi.org/10.1021/mp800051m.

(30) Tavares, A. J.; Poon, W.; Zhang, Y.-N.; Dai, Q.; Besla, R.; Ding, D.; Ouyang, B.; Li, A.; Chen, J.; Zheng, G.; Robbins, C.; Chan, W. C. W. Effect of Removing Kupffer Cells on Nanoparticle Tumor Delivery. *Proc. Natl. Acad. Sci. U. S. A.* **2017**, *114* (51), E10871–E10880. https://doi.org/10.1073/pnas.1713390114.

(31) Wilhelm, S.; Tavares, A. J.; Dai, Q.; Ohta, S.; Audet, J.; Dvorak, H. F.; Chan, W. C. W. Analysis of Nanoparticle Delivery to Tumours. *Nat. Rev. Mater.* **2016**, *1* (5), 16014. https://doi.org/10.1038/natrevmats.2016.14.

(32) Sindhwani, S.; Syed, A. M.; Ngai, J.; Kingston, B. R.; Maiorino, L.; Rothschild, J.; MacMillan, P.; Zhang, Y.; Rajesh, N. U.; Hoang, T.; Wu, J. L. Y.; Wilhelm, S.; Zilman, A.; Gadde, S.; Sulaiman, A.; Ouyang, B.; Lin, Z.; Wang, L.; Egeblad, M.; Chan, W. C. W. The Entry of Nanoparticles into Solid Tumours. *Nat. Mater.* **2020**. https://doi.org/10.1038/s41563-019-0566-2.

(33) Whitehead, K. A.; Langer, R.; Anderson, D. G. Knocking down Barriers: Advances in SiRNA Delivery. *Nat. Rev. Drug Discov.* **2009**, *8*, 129.

(34) Zámecník, J.; Vargová, L.; Homola, A.; Kodet, R.; Syková, E. Extracellular Matrix Glycoproteins and Diffusion Barriers in Human Astrocytic Tumours. *Neuropathol. Appl. Neurobiol.* **2004**, *30* (4), 338–350. https://doi.org/10.1046/j.0305-1846.2003.00541.x.

(35) Rees, P.; Wills, J. W.; Brown, M. R.; Barnes, C. M.; Summers, H. D. The Origin of Heterogeneous Nanoparticle Uptake by Cells. *Nat. Commun.* **2019**, *10* (1), 1–8. https://doi.org/10.1038/s41467-019-10112-4.

(36) Di Guglielmo, G. M.; Le Roy, C.; Goodfellow, A. F.; Wrana, J. L. Distinct Endocytic Pathways Regulate TGF-β Receptor Signalling and Turnover. *Nat. Cell Biol.* **2003**, *5* (5), 410–421. https://doi.org/10.1038/ncb975.

(37) Gilleron, J.; Querbes, W.; Zeigerer, A.; Borodovsky, A.; Marsico, G.; Schubert, U.; Manygoats, K.; Seifert, S.; Andree, C.; Stöter, M.; Epstein-Barash, H.; Zhang, L.; Koteliansky, V.; Fitzgerald, K.; Fava, E.; Bickle, M.; Kalaidzidis, Y.; Akinc, A.; Maier, M.; Zerial, M. Image-Based Analysis of Lipid Nanoparticle-Mediated SiRNA Delivery, Intracellular Trafficking and Endosomal Escape. *Nat. Biotechnol.* **2013**, *31* (7), 638–646. https://doi.org/10.1038/nbt.2612.

(38) Mirkin, C. A.; Letsinger, R. L.; Mucic, R. C.; Storhoff, J. J. A DNA-Based Method for Rationally Assembling Nanoparticles into Macroscopic Materials. *Nature* **1996**, *382* (6592), 607–609. https://doi.org/10.1038/382607a0.

(39) Seferos, D. S.; Prigodich, A. E.; Giljohann, D. A.; Patel, P. C.; Mirkin, C. A. Polyvalent DNA Nanoparticle Conjugates Stabilize Nucleic Acids. *Nano Lett.* **2009**, *9* (1), 308–311. https://doi.org/10.1021/nl802958f.

(40) Jensen, S. A.; Day, E. S.; Ko, C. H.; Hurley, L. A.; Luciano, J. P.; Kouri, F. M.; Merkel,

T. J.; Luthi, A. J.; Patel, P. C.; Cutler, J. I.; Daniel, W. L.; Scott, A. W.; Rotz, M. W.; Meade, T. J.; Giljohann, D. A.; Mirkin, C. A.; Stegh, A. H. Spherical Nucleic Acid Nanoparticle Conjugates as an RNAi-Based Therapy for Glioblastoma. *Sci. Transl. Med.* **2013**, *5* (209), 209ra152. https://doi.org/10.1126/scitranslmed.3006839.

(41) Kumthekar, P.; Ko, C. H.; Paunesku, T.; Dixit, K.; Sonabend, A. M.; Bloch, O.; Tate, M.; Schwartz, M.; Zuckerman, L.; Lezon, R.; Lukas, R. V.; Jovanovic, B.; McCortney, K.; Colman, H.; Chen, S.; Lai, B.; Antipova, O.; Deng, J.; Li, L.; Tommasini-Ghelfi, S.; Hurley, L. A.; Unruh, D.; Sharma, N. V.; Kandpal, M.; Kouri, F. M.; Davuluri, R. V.; Brat, D. J.; Muzzio, M.; Glass, M.; Vijayakumar, V.; Heidel, J.; Giles, F. J.; Adams, A. K.; James, C. D.; Woloschak, G. E.; Horbinski, C.; Stegh, A. H. A First-in-Human Phase 0 Clinical Study of RNA Interference-Based Spherical Nucleic Acids in Patients with Recurrent Glioblastoma. *Sci. Transl. Med.* **2021**, *13* (584). https://doi.org/10.1126/scitranslmed.abb3945.

(42) Prigodich, A. E.; Randeria, P. S.; Briley, W. E.; Kim, N. J.; Daniel, W. L.; Giljohann, D. A.; Mirkin, C. A. Multiplexed Nanoflares: MRNA Detection in Live Cells. *Anal. Chem.* **2012**, *84* (4), 2062–2066. https://doi.org/10.1021/ac202648w.

(43) Zhu, S.; Xing, H.; Gordiichuk, P.; Park, J.; Mirkin, C. A. PLGA Spherical Nucleic Acids. *Adv. Mater.* **2018**, *30* (22), 1707113. https://doi.org/10.1002/adma.201707113.

(44) Banga, R. J.; Chernyak, N.; Narayan, S. P.; Nguyen, S. T.; Mirkin, C. A. Liposomal Spherical Nucleic Acids. *J. Am. Chem. Soc.* **2014**, *136* (28), 9866–9869. https://doi.org/10.1021/ja504845f.

(45) Sprangers, A. J.; Hao, L.; Banga, R. J.; Mirkin, C. A. Liposomal Spherical Nucleic Acids

for Regulating Long Noncoding RNAs in the Nucleus. *Small* **2017**, *13* (10), 1602753. https://doi.org/10.1002/smll.201602753.

(46) Ferrer, J. R.; Wertheim, J. A.; Mirkin, C. A. Dual Toll-Like Receptor Targeting Liposomal Spherical Nucleic Acids. *Bioconjug. Chem.* **2019**, acs.bioconjchem.9b00047. https://doi.org/10.1021/acs.bioconjchem.9b00047.

(47) Radovic-Moreno, A. F.; Chernyak, N.; Mader, C. C.; Nallagatla, S.; Kang, R. S.; Hao, L.; Walker, D. A.; Halo, T. L.; Merkel, T. J.; Rische, C. H.; Anantatmula, S.; Burkhart, M.; Mirkin, C. A.; Gryaznov, S. M. Immunomodulatory Spherical Nucleic Acids. *Proc. Natl. Acad. Sci. U. S. A.* **2015**, *112* (13), 3892–3897. https://doi.org/10.1073/pnas.1502850112.

(48) Meckes, B.; Banga, R. J.; Nguyen, S. T.; Mirkin, C. A. Enhancing the Stability and Immunomodulatory Activity of Liposomal Spherical Nucleic Acids through Lipid-Tail DNA Modifications. *Small* **2018**, *14* (5), 1702909. https://doi.org/10.1002/smll.201702909.

(49) Rouge, J. L.; Sita, T. L.; Hao, L.; Kouri, F. M.; Briley, W. E.; Stegh, A. H.; Mirkin, C. A. Ribozyme-Spherical Nucleic Acids. *J. Am. Chem. Soc.* **2015**, *137* (33), 10528–10531. https://doi.org/10.1021/jacs.5b07104.

(50) Seferos, D. S.; Giljohann, D. A.; Hill, H. D.; Prigodich, A. E.; Mirkin, C. A. Nano-Flares: Probes for Transfection and MRNA Detection in Living Cells. *J. Am. Chem. Soc.* **2007**, *129* (50), 15477–15479. https://doi.org/10.1021/ja0776529.

(51) Samanta, D.; Ebrahimi, S. B.; Kusmierz, C. D.; Cheng, H. F.; Mirkin, C. A. Protein Spherical Nucleic Acids for Live-Cell Chemical Analysis. *J. Am. Chem. Soc.* **2020**, *142* (31), 13350–13355. https://doi.org/10.1021/jacs.0c06866.

(52) Cutler, J. I.; Auyeung, E.; Mirkin, C. A. Spherical Nucleic Acids. *J. Am. Chem. Soc.* **2012**, *134* (3), 1376–1391. https://doi.org/10.1021/ja209351u.

(53) Wang, T.; Larcher, L. M.; Ma, L.; Veedu, R. N. Systematic Screening of Commonly Used Commercial Transfection Reagents towards Efficient Transfection of Single-Stranded Oligonucleotides. *Molecules* **2018**, *23* (10). https://doi.org/10.3390/molecules23102564.

(54) Seferos, D. S.; Prigodich, A. E.; Giljohann, D. A.; Patel, P. C.; Mirkin, C. A. Polyvalent DNA Nanoparticle Conjugates Stabilize Nucleic Acids. *Nano Lett.* **2009**, *9* (1), 308–311. https://doi.org/10.1021/nl802958f.

(55) Barnaby, S. N.; Lee, A.; Mirkin, C. A. Probing the Inherent Stability of SiRNA Immobilized on Nanoparticle Constructs. *Proc. Natl. Acad. Sci. U. S. A.* **2014**, *111* (27), 9739–9744. https://doi.org/10.1073/pnas.1409431111.

(56) Soutschek, J.; Akinc, A.; Bramlage, B.; Charisse, K.; Constien, R.; Donoghue, M.; Elbashir, S.; Gelck, A.; Hadwiger, P.; Harborth, J.; John, M.; Kesavan, V.; Lavine, G.; Pandey, R. K.; Racie, T.; Rajeev, K. S.; Röhl, I.; Toudjarska, I.; Wang, G.; Wuschko, S.; Bumcrot, D.; Kotellansky, V.; Limmer, S.; Manoharan, M.; Vornlocher, H. P. Therapeutic Silencing of an Endogenous Gene by Systemic Administration of Modified SiRNAs. *Nature* **2004**, *432* (7014), 173–178. https://doi.org/10.1038/nature03121.

(57) Akinc, A.; Querbes, W.; De, S.; Qin, J.; Frank-Kamenetsky, M.; Jayaprakash, K. N.; Jayaraman, M.; Rajeev, K. G.; Cantley, W. L.; Dorkin, J. R.; Butler, J. S.; Qin, L.; Racie, T.; Sprague, A.; Fava, E.; Zeigerer, A.; Hope, M. J.; Zerial, M.; Sah, D. W.; Fitzgerald, K.; Tracy, M. A.; Manoharan, M.; Koteliansky, V.; Fougerolles, A. De; Maier, M. A. Targeted Delivery of RNAi Therapeutics with Endogenous and Exogenous Ligand-Based

Mechanisms. *Mol. Ther.* **2010**, *18* (7), 1357–1364. https://doi.org/10.1038/mt.2010.85.

(58) Choi, C. H. J.; Hao, L.; Narayan, S. P.; Auyeung, E.; Mirkin, C. A. Mechanism for the Endocytosis of Spherical Nucleic Acid Nanoparticle Conjugates. *Proc. Natl. Acad. Sci.* **2013**, *110* (19), 7625–7630. https://doi.org/10.1073/pnas.1305804110.

(59) PrabhuDas, M. R.; Baldwin, C. L.; Bollyky, P. L.; Bowdish, D. M. E.; Drickamer, K.; Febbraio, M.; Herz, J.; Kobzik, L.; Krieger, M.; Loike, J.; McVicker, B.; Means, T. K.; Moestrup, S. K.; Post, S. R.; Sawamura, T.; Silverstein, S.; Speth, R. C.; Telfer, J. C.; Thiele, G. M.; Wang, X.-Y.; Wright, S. D.; El Khoury, J. A Consensus Definitive Classification of Scavenger Receptors and Their Roles in Health and Disease. *J. Immunol.* **2017**, *198* (10), 3775–3789. https://doi.org/10.4049/jimmunol.1700373.

(60) Narayan, S. P.; Choi, C. H. J.; Hao, L.; Calabrese, C. M.; Auyeung, E.; Zhang, C.; Goor, O. J. G. M.; Mirkin, C. A. The Sequence-Specific Cellular Uptake of Spherical Nucleic Acid Nanoparticle Conjugates. *Small* **2015**, *11* (33), 4173–4182. https://doi.org/10.1002/smll.201500027.

(61) Kawabata, K.; Takakura, Y.; Hashida, M. The Fate of Plasmid DNA After Intravenous Injection in Mice: Involvement of Scavenger Receptors in Its Hepatic Uptake. *Pharm. Res. An Off. J. Am. Assoc. Pharm. Sci.* **1995**, *12* (6), 825–830. https://doi.org/10.1023/A:1016248701505.

(62) Chinen, A. B.; Guan, C. M.; Mirkin, C. A. Spherical Nucleic Acid Nanoparticle Conjugates Enhance G-Quadruplex Formation and Increase Serum Protein Interactions. *Angew. Chemie - Int. Ed.* **2015**, *54* (2), 527–531. https://doi.org/10.1002/anie.201409211.

(63) Chinen, A. B.; Guan, C. M.; Ko, C. H.; Mirkin, C. A. The Impact of Protein Corona

Formation on the Macrophage Cellular Uptake and Biodistribution of Spherical Nucleic Acids. *Small* **2017**, *13* (16), 1603847. https://doi.org/10.1002/smll.201603847.

(64) Vu, V. P.; Gifford, G. B.; Chen, F.; Benasutti, H.; Wang, G.; Groman, E. V.; Scheinman, R.; Saba, L.; Moghimi, S. M.; Simberg, D. Immunoglobulin Deposition on Biomolecule Corona Determines Complement Opsonization Efficiency of Preclinical and Clinical Nanoparticles. *Nat. Nanotechnol.* **2019**, *14* (3), 260–268. https://doi.org/10.1038/s41565-018-0344-3.

(65) Rosi, N. L.; Giljohann, D. A.; Thaxton, C. S.; Lytton-Jean, A. K. R.; Han, M. S.; Mirkin, C. A. Oligonucleotide-Modified Gold Nanoparticles for Intracellular Gene Regulation. *Science (80-.).* **2006**, *312* (5776), 1027–1030. https://doi.org/10.1126/science.1125559.

(66) Kusmierz, C. D.; Bujold, K. E.; Callmann, C. E.; Mirkin, C. A. Defining the Design Parameters for in Vivo Enzyme Delivery through Protein Spherical Nucleic Acids. *ACS Cent. Sci.* **2020**, *6* (5), 815–822. https://doi.org/10.1021/acscentsci.0c00313.

(67) Lai-Cheong, J. E.; McGrath, J. A. Advances in Understanding the Genetic Basis of Inherited Single Gene Skin Barrier Disorders: New Clues to Key Genes That May Be Involved in the Pathogenesis of Atopic Dermatitis. *Anais Brasileiros de Dermatologia*. Sociedade Brasileira de Dermatologia 2006, pp 567–571. https://doi.org/10.1590/s0365-05962006000600009.

(68) Zheng, D.; Giljohann, D. A.; Chen, D. L.; Massich, M. D.; Wang, X.-Q.; Iordanov, H.; Mirkin, C. A.; Paller, A. S. Topical Delivery of SiRNA-Based Spherical Nucleic Acid Nanoparticle Conjugates for Gene Regulation. *Proc. Natl. Acad. Sci. U. S. A.* **2012**, *109* (30), 11975–11980. https://doi.org/10.1073/pnas.1118425109.

(69) Randeria, P. S.; Seeger, M. A.; Wang, X. Q.; Wilson, H.; Shipp, D.; Mirkin, C. A.; Paller, A. S. SiRNA-Based Spherical Nucleic Acids Reverse Impaired Wound Healing in Diabetic Mice by Ganglioside GM3 Synthase Knockdown. *Proc. Natl. Acad. Sci. U. S. A.* **2015**, *112* (18), 5573–5578. https://doi.org/10.1073/pnas.1505951112.

(70) Ponedal, A.; Zhu, S.; Sprangers, A. J.; Wang, X. Q.; Yeo, D. C.; Lio, D. C. S.; Zheng, M.; Capek, M.; Narayan, S. P.; Meckes, B.; Paller, A. S.; Xu, C.; Mirkin, C. A. Attenuation of Abnormal Scarring Using Spherical Nucleic Acids Targeting Transforming Growth Factor Beta 1. *ACS Appl. Bio Mater.* **2020**, *3* (12), 8603–8610. https://doi.org/10.1021/acsabm.0c00990.

(71) Zhang, W.; Meckes, B.; Mirkin, C. A. Spherical Nucleic Acids with Tailored and Active Protein Coronae. *ACS Cent. Sci.* **2019**, *5* (12), 1983–1990. https://doi.org/10.1021/ACSCENTSCI.9B01105.

(72) Zhang, K.; Hao, L.; Hurst, S. J.; Mirkin, C. A. Antibody-Linked Spherical Nucleic Acids for Cellular Targeting. *J. Am. Chem. Soc.* **2012**, *134* (40), 16488–16491. https://doi.org/10.1021/JA306854D.

(73) Dhar, S.; Daniel, W. L.; Giljohann, D. A.; Mirkin, C. A.; Lippard, S. J. Polyvalent Oligonucleotide Gold Nanoparticle Conjugates as Delivery Vehicles for Platinum(IV) Warheads. *J. Am. Chem. Soc.* **2009**, *131* (41), 14652–14653. https://doi.org/10.1021/JA9071282.

(74) Zheng, D.; Seferos, D. S.; Giljohann, D. A.; Patel, P. C.; Mirkin, C. A. Aptamer Nano-Flares for Molecular Detection in Living Cells. *Nano Lett.* **2009**, *9* (9), 3258–3261. https://doi.org/10.1021/NL901517B.

(75) Kouri, F. M.; Hurley, L. A.; Daniel, W. L.; Day, E. S.; Hua, Y.; Hao, L.; Peng, C.-Y.; Merkel, T. J.; Queisser, M. A.; Ritner, C.; Zhang, H.; James, C. D.; Sznajder, J. I.; Chin, L.; Giljohann, D. A.; Kessler, J. A.; Peter, M. E.; Mirkin, C. A.; Stegh, A. H. MiR-182 Integrates Apoptosis, Growth, and Differentiation Programs in Glioblastoma. *Genes Dev.* **2015**, *29* (7), 732. https://doi.org/10.1101/GAD.257394.114.

(76) H, C.; A, D.; S, S.; DJ, H.; MB, C.; SM, V. In Vivo Study of Spherical Gold Nanoparticles: Inflammatory Effects and Distribution in Mice. *PLoS One* **2013**, *8* (2). https://doi.org/10.1371/JOURNAL.PONE.0058208.

(77) Banga, R. J.; Chernyak, N.; Narayan, S. P.; Nguyen, S. T.; Mirkin, C. A. Liposomal Spherical Nucleic Acids. *J. Am. Chem. Soc.* **2014**, *136* (28), 9866–9869. https://doi.org/10.1021/ja504845f.

(78) Ebrahimi, S. B.; Samanta, D.; Cheng, H. F.; Nathan, L. I.; Mirkin, C. A. Forced Intercalation (FIT)-Aptamers. *J. Am. Chem. Soc.* **2019**, *141* (35), 13744–13748. https://doi.org/10.1021/jacs.9b06450.

(79) Guan, C.; Chernyak, N.; Dominguez, D.; Cole, L.; Zhang, B.; Mirkin, C. A. RNA-Based Immunostimulatory Liposomal Spherical Nucleic Acids as Potent TLR7/8 Modulators. *Small* **2018**, *14* (49), 1803284. https://doi.org/10.1002/SMLL.201803284.

(80) Skakuj, K.; Wang, S.; Qin, L.; Lee, A.; Zhang, B.; Mirkin, C. A. Conjugation Chemistry-Dependent T-Cell Activation with Spherical Nucleic Acids. *J. Am. Chem. Soc.* **2018**, *140* (4), 1227–1230. https://doi.org/10.1021/JACS.7B12579.

(81) Yamankurt, G.; Berns, E. J.; Xue, A.; Lee, A.; Bagheri, N.; Mrksich, M.; Mirkin, C. A. Exploration of the Nanomedicine-Design Space with High-Throughput Screening and

Machine Learning. *Nat. Biomed. Eng.* **2019**, *3* (4), 318–327. https://doi.org/10.1038/s41551-019-0351-1.

(82) Callmann, C. E.; Cole, L. E.; Kusmierz, C. D.; Huang, Z.; Horiuchi, D.; Mirkin, C. A. Tumor Cell Lysate-Loaded Immunostimulatory Spherical Nucleic Acids as Therapeutics for Triple-Negative Breast Cancer. *Proc. Natl. Acad. Sci.* **2020**, *117* (30), 17543–17550. https://doi.org/10.1073/PNAS.2005794117.

(83) Callmann, C. E.; Kusmierz, C. D.; Dittmar, J. W.; Broger, L.; Mirkin, C. A. Impact of Liposomal Spherical Nucleic Acid Structure on Immunotherapeutic Function. *ACS Cent. Sci.* **2021**, *7*, 899. https://doi.org/10.1021/ACSCENTSCI.1C00181.

(84) Akinc, A.; Zumbuehl, A.; Goldberg, M.; Leshchiner, E. S.; Busini, V.; Hossain, N.; Bacallado, S. A.; Nguyen, D. N.; Fuller, J.; Alvarez, R.; Borodovsky, A.; Borland, T.; Constien, R.; de Fougerolles, A.; Dorkin, J. R.; Narayanannair Jayaprakash, K.; Jayaraman, M.; John, M.; Koteliansky, V.; Manoharan, M.; Nechev, L.; Qin, J.; Racie, T.; Raitcheva, D.; Rajeev, K. G.; Sah, D. W. Y.; Soutschek, J.; Toudjarska, I.; Vornlocher, H.-P.; Zimmermann, T. S.; Langer, R.; Anderson, D. G. A Combinatorial Library of Lipid-like Materials for Delivery of RNAi Therapeutics. *Nat. Biotechnol.* **2008**, *26* (5), 561–569. https://doi.org/10.1038/nbt1402.

(85) Allen, T. M.; Cullis, P. R. Liposomal Drug Delivery Systems: From Concept to Clinical Applications. *Adv. Drug Deliv. Rev.* **2013**, *65* (1), 36–48. https://doi.org/10.1016/J.ADDR.2012.09.037.

(86) Lu, J. J.; Langer, R.; Chen, J. A Novel Mechanism Is Involved in Cationic Lipid-Mediated Functional SiRNA Delivery. *Mol. Pharm.* **2009**, *6* (3), 763–771.

https://doi.org/10.1021/mp900023v.

(87) Kanasty, R.; Dorkin, J. R.; Vegas, A.; Anderson, D. Delivery Materials for SiRNA Therapeutics. *Nat. Mater.* **2013**, *12* (11), 967–977. https://doi.org/10.1038/nmat3765.

(88) Zuhorn, I. S.; Bakowsky, U.; Polushkin, E.; Visser, W. H.; Stuart, M. C. A.; Engberts, J. B. F. N.; Hoekstra, D. Nonbilayer Phase of Lipoplex-Membrane Mixture Determines Endosomal Escape of Genetic Cargo and Transfection Efficiency. *Mol. Ther.* **2005**, *11* (5), 801–810. https://doi.org/10.1016/j.ymthe.2004.12.018.

(89) Maier, M. A.; Jayaraman, M.; Matsuda, S.; Liu, J.; Barros, S.; Querbes, W.; Tam, Y. K.; Ansell, S. M.; Kumar, V.; Qin, J.; Zhang, X.; Wang, Q.; Panesar, S.; Hutabarat, R.; Carioto, M.; Hettinger, J.; Kandasamy, P.; Butler, D.; Rajeev, K. G.; Pang, B.; Charisse, K.; Fitzgerald, K.; Mui, B. L.; Du, X.; Cullis, P.; Madden, T. D.; Hope, M. J.; Manoharan, M.; Akinc, A. Biodegradable Lipids Enabling Rapidly Eliminated Lipid Nanoparticles for Systemic Delivery of RNAi Therapeutics. *Mol. Ther.* **2013**, *21* (8), 1570–1578. https://doi.org/10.1038/mt.2013.124.

(90) Semple, S. C.; Akinc, A.; Chen, J.; Sandhu, A. P.; Mui, B. L.; Cho, C. K.; Sah, D. W. Y.; Stebbing, D.; Crosley, E. J.; Yaworski, E.; Hafez, I. M.; Dorkin, J. R.; Qin, J.; Lam, K.; Rajeev, K. G.; Wong, K. F.; Jeffs, L. B.; Nechev, L.; Eisenhardt, M. L.; Jayaraman, M.; Kazem, M.; Maier, M. A.; Srinivasulu, M.; Weinstein, M. J.; Chen, Q.; Alvarez, R.; Barros, S. A.; De, S.; Klimuk, S. K.; Borland, T.; Kosovrasti, V.; Cantley, W. L.; Tam, Y. K.; Manoharan, M.; Ciufolini, M. A.; Tracy, M. A.; de Fougerolles, A.; MacLachlan, I.; Cullis, P. R.; Madden, T. D.; Hope, M. J. Rational Design of Cationic Lipids for SiRNA Delivery. *Nat. Biotechnol.* **2010**, *28* (2), 172–176. https://doi.org/10.1038/nbt.1602.

(91) Jayaraman, M.; Ansell, S. M.; Mui, B. L.; Tam, Y. K.; Chen, J.; Du, X.; Butler, D.; Eltepu, L.; Matsuda, S.; Narayanannair, J. K.; Rajeev, K. G.; Hafez, I. M.; Akinc, A.; Maier, M. A.; Tracy, M. A.; Cullis, P. R.; Madden, T. D.; Manoharan, M.; Hope, M. J. Maximizing the Potency of SiRNA Lipid Nanoparticles for Hepatic Gene Silencing In Vivo**. *Angew. Chemie Int. Ed.* **2012**, *51* (34), 8259–33. https://doi.org/10.1002/anie.201203263.

(92) Love, K. T.; Mahon, K. P.; Levins, C. G.; Whitehead, K. A.; Querbes, W.; Dorkin, J. R.; Qin, J.; Cantley, W.; Qin, L. L.; Racie, T.; Frank-Kamenetsky, M.; Yip, K. N.; Alvarez, R.; Sah, D. W. Y.; De Fougerolles, A.; Fitzgerald, K.; Koteliansky, V.; Akinc, A.; Langer, R.; Anderson, D. G. Lipid-like Materials for Low-Dose, in Vivo Gene Silencing. *Proc. Natl. Acad. Sci. U. S. A.* **2010**, *107* (5), 1864–1869. https://doi.org/10.1073/pnas.0910603106.

(93) Lokugamage, M. P.; Sago, C. D.; Gan, Z.; Krupczak, B. R.; Dahlman, J. E. Constrained Nanoparticles Deliver SiRNA and SgRNA to T Cells In Vivo without Targeting Ligands. *Adv. Mater.* **2019**, *31* (41), 1902251. https://doi.org/10.1002/adma.201902251.

(94) Montgomery, D. C. *Design and Analysis of Experiments*, Eighth edi.; John Wiley & Sons, Inc.: Hoboken, NJ, 2013.

(95) Sago, C. D.; Lokugamage, M. P.; Islam, F. Z.; Krupczak, B. R.; Sato, M.; Dahlman, J. E. Nanoparticles That Deliver RNA to Bone Marrow Identified by in Vivo Directed Evolution. *J. Am. Chem. Soc.* **2018**, *140* (49), 17095–17105. https://doi.org/10.1021/jacs.8b08976.

(96) Dahlman, J. E.; Kauffman, K. J.; Xing, Y.; Shaw, T. E.; Mir, F. F.; Dlott, C. C.; Langer,

R.; Anderson, D. G.; Wang, E. T. Barcoded Nanoparticles for High Throughput in Vivo Discovery of Targeted Therapeutics. *Proc. Natl. Acad. Sci. U. S. A.* **2017**, *114* (8), 2060–2065. https://doi.org/10.1073/pnas.1620874114.

(97) Chandler, R. J. Messenger RNA Therapy as an Option for Treating Metabolic Disorders. *Proc. Natl. Acad. Sci. U. S. A.* **2019**, *116* (42). https://doi.org/10.1073/PNAS.1914673116.

(98) Truong, B.; Allegri, G.; Liu, X.-B.; Burke, K. E.; Zhu, X.; Cederbaum, S. D.; Häberle, J.; Martini, P. G. V.; Lipshutz, G. S. Lipid Nanoparticle-Targeted MRNA Therapy as a Treatment for the Inherited Metabolic Liver Disorder Arginase Deficiency. *Proc. Natl. Acad. Sci.* **2019**, *116* (42), 21150–21159. https://doi.org/10.1073/PNAS.1906182116.

(99) Guimaraes, P. P. G.; Zhang, R.; Spektor, R.; Tan, M.; Chung, A.; Billingsley, M. M.; El-Mayta, R.; Riley, R. S.; Wang, L.; Wilson, J. M.; Mitchell, M. J. Ionizable Lipid Nanoparticles Encapsulating Barcoded MRNA for Accelerated in Vivo Delivery Screening. *J. Control. Release* **2019**, *316*. https://doi.org/10.1016/j.jconrel.2019.10.028.

(100) Musunuru, K.; Chadwick, A. C.; Mizoguchi, T.; Garcia, S. P.; DeNizio, J. E.; Reiss, C. W.; Wang, K.; Iyer, S.; Dutta, C.; Clendaniel, V.; Amaonye, M.; Beach, A.; Berth, K.; Biswas, S.; Braun, M. C.; Chen, H.-M.; Colace, T. V.; Ganey, J. D.; Gangopadhyay, S. A.; Garrity, R.; Kasiewicz, L. N.; Lavoie, J.; Madsen, J. A.; Matsumoto, Y.; Mazzola, A. M.; Nasrullah, Y. S.; Nneji, J.; Ren, H.; Sanjeev, A.; Shay, M.; Stahley, M. R.; Fan, S. H. Y.; Tam, Y. K.; Gaudelli, N. M.; Ciaramella, G.; Stolz, L. E.; Malyala, P.; Cheng, C. J.; Rajeev, K. G.; Rohde, E.; Bellinger, A. M.; Kathiresan, S. In Vivo CRISPR Base Editing of PCSK9 Durably Lowers Cholesterol in Primates. *Nat. 2021 5937859* **2021**, *593* (7859), 429–434. https://doi.org/10.1038/s41586-021-03534-y.

(101) Zhou, C.; Sun, Y.; Yan, R.; Liu, Y.; Zuo, E.; Gu, C.; Han, L.; Wei, Y.; Hu, X.; Zeng, R.; Li, Y.; Zhou, H.; Guo, F.; Yang, H. Off-Target RNA Mutation Induced by DNA Base Editing and Its Elimination by Mutagenesis. *Nature* **2019**, *571* (7764), 275–278. https://doi.org/10.1038/s41586-019-1314-0.

(102) Wang, S.; Qin, L.; Yamankurt, G.; Skakuj, K.; Huang, Z.; Chen, P.-C.; Dominguez, D.; Lee, A.; Zhang, B.; Mirkin, C. A. Rational Vaccinology with Spherical Nucleic Acids. *Proc. Natl. Acad. Sci.* **2019**, *116* (21), 10473–10481. https://doi.org/10.1073/PNAS.1902805116.

(103) Ouyang, B.; Poon, W.; Zhang, Y. N.; Lin, Z. P.; Kingston, B. R.; Tavares, A. J.; Zhang, Y.; Chen, J.; Valic, M. S.; Syed, A. M.; MacMillan, P.; Couture-Senécal, J.; Zheng, G.; Chan, W. C. W. The Dose Threshold for Nanoparticle Tumour Delivery. *Nat. Mater.* **2020**, 1–10. https://doi.org/10.1038/s41563-020-0755-z.

(104) Lebedeva, I.; Stein, C. ANTISENSE OLIGONUCLEOTIDES : Promise and Reality. *Annu. Rev. Pharmacol. Toxicol.* **2001**, *41* (1), 403–419. https://doi.org/10.1146/annurev.pharmtox.41.1.403.

(105) de Wolf, H. K.; Snel, C. J.; Verbaan, F. J.; Schiffelers, R. M.; Hennink, W. E.; Storm, G. Effect of Cationic Carriers on the Pharmacokinetics and Tumor Localization of Nucleic Acids after Intravenous Administration. *Int. J. Pharm.* **2007**, *331* (2), 167–175. https://doi.org/10.1016/J.IJPHARM.2006.10.029.

(106) Samanta, D.; Ebrahimi, S. B.; Mirkin, C. A. Nucleic-Acid Structures as Intracellular Probes for Live Cells. *Adv. Mater.* **2019**, 1901743. https://doi.org/10.1002/adma.201901743.

(107) Barnaby, S. N.; Perelman, G. A.; Kohlstedt, K. L.; Chinen, A. B.; Schatz, G. C.; Mirkin, C. A. Design Considerations for RNA Spherical Nucleic Acids (SNAs). *Bioconjug. Chem.* **2016**, *27* (9), 2124–2131. https://doi.org/10.1021/acs.bioconjchem.6b00350.

(108) Zheng, D.; Giljohann, D. A.; Chen, D. L.; Massich, M. D.; Wang, X.-Q.; Iordanov, H.; Mirkin, C. A.; Paller, A. S. Topical Delivery of SiRNA-Based Spherical Nucleic Acid Nanoparticle Conjugates for Gene Regulation. *Proc. Natl. Acad. Sci.* **2012**, *109* (30), 11975–11980. https://doi.org/10.1073/pnas.1118425109.

(109) Jensen, S. A.; Day, E. S.; Ko, C. H.; Hurley, L. A.; Luciano, J. P.; Kouri, F. M.; Merkel, T. J.; Luthi, A. J.; Patel, P. C.; Cutler, J. I.; Daniel, W. L.; Scott, A. W.; Rotz, M. W.; Meade, T. J.; Giljohann, D. A.; Mirkin, C. A.; Stegh, A. H. Spherical Nucleic Acid Nanoparticle Conjugates as an RNAi-Based Therapy for Glioblastoma. *Sci. Transl. Med.* **2013**, *5* (209), 209ra152 LP-209ra152.

(110) Sita, T. L.; Kouri, F. M.; Hurley, L. A.; Merkel, T. J.; Chalastanis, A.; May, J. L.; Ghelfi, S. T.; Cole, L. E.; Cayton, T. C.; Barnaby, S. N.; Sprangers, A. J.; Savalia, N.; James, C. D.; Lee, A.; Mirkin, C. A.; Stegh, A. H. Dual Bioluminescence and Near-Infrared Fluorescence Monitoring to Evaluate Spherical Nucleic Acid Nanoconjugate Activity in Vivo. *Proc. Natl. Acad. Sci. U. S. A.* **2017**, *114* (16), 4129–4134. https://doi.org/10.1073/pnas.1702736114.

(111) Ernsting, M. J.; Murakami, M.; Roy, A.; Li, S.-D. Factors Controlling the Pharmacokinetics, Biodistribution and Intratumoral Penetration of Nanoparticles. *J. Control. Release* **2013**, *172* (3), 782–794. https://doi.org/10.1016/J.JCONREL.2013.09.013.

(112) Hoshyar, N.; Gray, S.; Han, H.; Bao, G. The Effect of Nanoparticle Size on *in Vivo* Pharmacokinetics and Cellular Interaction. *Nanomedicine* **2016**, *11* (6), 673–692. https://doi.org/10.2217/nnm.16.5.

(113) Jasinski, D. L.; Li, H.; Guo, P. The Effect of Size and Shape of RNA Nanoparticles on Biodistribution. *Mol. Ther.* **2018**, *26* (3), 784–792. https://doi.org/10.1016/j.ymthe.2017.12.018.

(114) Hadjidemetriou, M.; Kostarelos, K. Evolution of the Nanoparticle Corona. *Nat. Nanotechnol.* **2017**, *12* (4), 288–290. https://doi.org/10.1038/nnano.2017.61.

(115) Zhang, C.; Qu, G.; Sun, Y.; Wu, X.; Yao, Z.; Guo, Q.; Ding, Q.; Yuan, S.; Shen, Z.; Ping, Q.; Zhou, H. Pharmacokinetics, Biodistribution, Efficacy and Safety of N-Octyl-O-Sulfate Chitosan Micelles Loaded with Paclitaxel. *Biomaterials* **2008**, *29* (9), 1233–1241. https://doi.org/10.1016/J.BIOMATERIALS.2007.11.029.

(116) Fonge, H.; Huang, H.; Scollard, D.; Reilly, R. M.; Allen, C. Influence of Formulation Variables on the Biodistribution of Multifunctional Block Copolymer Micelles. *J. Control. Release* **2012**, *157* (3), 366–374. https://doi.org/10.1016/J.JCONREL.2011.09.088.

(117) Ye, L.; Yong, K.-T.; Liu, L.; Roy, I.; Hu, R.; Zhu, J.; Cai, H.; Law, W.-C.; Liu, J.; Wang, K.; Liu, J.; Liu, Y.; Hu, Y.; Zhang, X.; Swihart, M. T.; Prasad, P. N. A Pilot Study in Non-Human Primates Shows No Adverse Response to Intravenous Injection of Quantum Dots. *Nat. Nanotechnol.* **2012**, *7* (7), 453–458. https://doi.org/10.1038/nnano.2012.74.

(118) Fischer, H. C.; Liu, L.; Pang, K. S.; Chan, W. C. W. Pharmacokinetics of Nanoscale Quantum Dots: In Vivo Distribution, Sequestration, and Clearance in the Rat. *Adv. Funct.*

Mater. **2006**, *16* (10), 1299–1305. https://doi.org/10.1002/adfm.200500529.

(119) De Jong, W. H.; Hagens, W. I.; Krystek, P.; Burger, M. C.; Sips, A. J. A. M.; Geertsma, R. E. Particle Size-Dependent Organ Distribution of Gold Nanoparticles after Intravenous Administration. *Biomaterials* **2008**, *29* (12), 1912–1919. https://doi.org/10.1016/J.BIOMATERIALS.2007.12.037.

(120) Semmler-Behnke, M.; Kreyling, W. G.; Lipka, J.; Fertsch, S.; Wenk, A.; Takenaka, S.; Schmid, G.; Brandau, W. Biodistribution of 1.4- and 18-Nm Gold Particles in Rats. *Small* **2008**, *4* (12), 2108–2111. https://doi.org/10.1002/smll.200800922.

(121) Liu, Z.; Cai, W.; He, L.; Nakayama, N.; Chen, K.; Sun, X.; Chen, X.; Dai, H. In Vivo Biodistribution and Highly Efficient Tumour Targeting of Carbon Nanotubes in Mice. *Nat. Nanotechnol.* **2007**, *2* (1), 47–52. https://doi.org/10.1038/nnano.2006.170.

(122) Yang, S.-T.; Guo, W.; Lin, Y.; Deng, X.-Y.; Wang, H.-F.; Sun, H.-F.; Liu, Y.-F.; Wang, X.; Wang, W.; Chen, M.; Huang, Y.-P.; Sun, Y.-P. Biodistribution of Pristine Single-Walled Carbon Nanotubes In Vivo †. *J. Phys. Chem. C* **2007**, *111*, 17761–17764. https://doi.org/10.1021/jp070712c.

(123) Ferrari, M. Frontiers in Cancer Nanomedicine: Directing Mass Transport through Biological Barriers. *Trends Biotechnol.* **2010**, *28* (4), 181–188. https://doi.org/10.1016/j.tibtech.2009.12.007.

(124) NU-0129 in Treating Patients With Recurrent Glioblastoma or Gliosarcoma Undergoing Surgery o Title https://clinicaltrials.gov/ct2/show/NCT03020017?term=spherical+nucleic+acid&rank=1 (accessed Sep 4, 2019).

(125) Exicure announces data for topical anti-TNF compound AST-005 in patients with mild to moderate psoriasis http://investors.exicuretx.com/phoenix.zhtml?c=254193&p=irol-newsArticle&ID=2346007 (accessed Sep 5, 2019).

(126) Intratumoral AST-008 Combined With Pembrolizumab in Patients With Advanced Solid Tumors.

(127) Exicure, Inc. Reports Full Year 2018 Financial Results and Corporate Progress https://www.sec.gov/Archives/edgar/data/1698530/000169853019000014/a8k3819exhibit991.htm (accessed Sep 5, 2019).

(128) Pfeiffer, I.; Höök, F. Bivalent Cholesterol-Based Coupling of Oligonucletides to Lipid Membrane Assemblies. *J. Am. Chem. Soc.* **2004**, *126*, 10224–10225. https://doi.org/10.1021/ja048514b.

(129) van der Meulen, S. A. J.; Dubacheva, G. V.; Dogterom, M.; Richter, R. P.; Leunissen, M. E. Quartz Crystal Microbalance with Dissipation Monitoring and Spectroscopic Ellipsometry Measurements of the Phospholipid Bilayer Anchoring Stability and Kinetics of Hydrophobically Modified DNA Oligonucleotides. *Langmuir* **2014**, *30* (22), 6525–6533. https://doi.org/10.1021/la500940a.

(130) Gambinossi, F.; Banchelli, M.; Durand, A.; Berti, D.; Brown, T.; Caminati, G.; Baglioni, P. Modulation of Density and Orientation of Amphiphilic DNA Anchored to Phospholipid Membranes. I. Supported Lipid Bilayers. *J. Phys. Chem. B* **2010**, *114* (21), 7338–7347. https://doi.org/10.1021/jp100730x.

(131) Meckes, B.; Banga, R. J.; Nguyen, S. T.; Mirkin, C. A. Enhancing the Stability and Immunomodulatory Activity of Liposomal Spherical Nucleic Acids through Lipid-Tail

DNA Modifications. *Small* **2018**, *14* (5), 1702909. https://doi.org/10.1002/smll.201702909.

(132) Banga, R. J.; Chernyak, N.; Narayan, S. P.; Nguyen, S. T.; Mirkin, C. A. Liposomal Spherical Nucleic Acids. *J. Am. Chem. Soc.* **2014**, *136* (28), 9866–9869. https://doi.org/10.1021/ja504845f.

(133) Krieg, A. M.; Yi, A.-K.; Matson, S.; Waldschmidt, T. J.; Bishop, G. A.; Teasdale, R.; Koretzky, G. A.; Klinman, D. M. CpG Motifs in Bacterial DNA Trigger Direct B-Cell Activation. *Nature* **1995**, *374* (6522), 546–549. https://doi.org/10.1038/374546a0.

(134) Ballas, Z. K.; Krieg, A. M.; Warren, T.; Rasmussen, W.; Davis, H. L.; Waldschmidt, M.; Weiner, G. J. Divergent Therapeutic and Immunologic Effects of Oligodeoxynucleotides with Distinct CpG Motifs. *J. Immunol.* **2001**, *167* (9), 4878–4886. https://doi.org/10.4049/jimmunol.167.9.4878.

(135) Nguyen, D. N.; Mahon, K. P.; Chikh, G.; Kim, P.; Chung, H.; Vicari, A. P.; Love, K. T.; Goldberg, M.; Chen, S.; Krieg, A. M.; Chen, J.; Langer, R.; Anderson, D. G. Lipid-Derived Nanoparticles for Immunostimulatory RNA Adjuvant Delivery. *Proc. Natl. Acad. Sci.* **2012**, *109* (14), E797–E803. https://doi.org/10.1073/pnas.1121423109.

(136) Jackson, A. L.; Linsley, P. S. Recognizing and Avoiding SiRNA Off-Target Effects for Target Identification and Therapeutic Application. *Nat. Rev. Drug Discov.* **2010**, *9* (1), 57–67. https://doi.org/10.1038/nrd3010.

(137) Dobrovolskaia, M. A.; McNeil, S. E. Immunological and Hematological Toxicities Challenging Clinical Translation of Nucleic Acid-Based Therapeutics. *Expert Opin. Biol. Ther.* **2015**, *15* (7), 1023–1048. https://doi.org/10.1517/14712598.2015.1014794.

(138) Massich, M. D.; Giljohann, D. A.; Schmucker, A. L.; Patel, P. C.; Mirkin, C. A. Cellular Response of Polyvalent Oligonucleotide−Gold Nanoparticle Conjugates. *ACS Nano* **2010**, *4* (10), 5641–5646. https://doi.org/10.1021/nn102228s.

(139) Colotta, F.; Borré, A.; Wang, J. M.; Tattanelli, M.; Maddalena, F.; Polentarutti, N.; Peri, G.; Mantovani, A. Expression of a Monocyte Chemotactic Cytokine by Human Mononuclear Phagocytes. *J. Immunol.* **1992**, *148* (3), 760–765.

(140) Serbina, N. V.; Jia, T.; Hohl, T. M.; Pamer, E. G. Monocyte-Mediated Defense Against Microbial Pathogens. *Annu. Rev. Immunol.* **2008**, *26* (1), 421–452. https://doi.org/10.1146/annurev.immunol.26.021607.090326.

(141) Blanco, E.; Shen, H.; Ferrari, M. Principles of Nanoparticle Design for Overcoming Biological Barriers to Drug Delivery. *Nat. Biotechnol.* **2015**, *33* (9), 941–951. https://doi.org/10.1038/nbt.3330.

(142) Whitehead, K. A.; Langer, R.; Anderson, D. G. Knocking down Barriers: Advances in SiRNA Delivery. *Nat. Rev. Drug Discov.* **2009**, *8* (2), 129–138. https://doi.org/10.1038/nrd2742.

(143) McCaffrey, A. P.; Meuse, L.; Pham, T. T. T.; Conklin, D. S.; Hannon, G. J.; Kay, M. A. RNA Interference in Adult Mice. *Nature* **2002**, *418* (6893), 38–39. https://doi.org/10.1038/418038a.

(144) Morrissey, D. V.; Lockridge, J. A.; Shaw, L.; Blanchard, K.; Jensen, K.; Breen, W.; Hartsough, K.; Machemer, L.; Radka, S.; Jadhav, V.; Vaish, N.; Zinnen, S.; Vargeese, C.; Bowman, K.; Shaffer, C. S.; Jeffs, L. B.; Judge, A.; MacLachlan, I.; Polisky, B. Potent and Persistent in Vivo Anti-HBV Activity of Chemically Modified SiRNAs. *Nat.*

Biotechnol. **2005**, *23* (8), 1002–1007. https://doi.org/10.1038/nbt1122.

(145) Ferrer, J. R.; Sinegra, A. J.; Ivancic, D.; Yeap, X. Y.; Qiu, L.; Wang, J. J.; Zhang, Z. J.; Wertheim, J. A.; Mirkin, C. A. Structure-Dependent Biodistribution of Liposomal Spherical Nucleic Acids. *ACS Nano* **2020**, *14* (2), 1682–1693. https://doi.org/10.1021/acsnano.9b07254.

(146) Rizk, M.; Tüzmen, Ş. Update on the Clinical Utility of an RNA Interference-Based Treatment: Focus on Patisiran. *Pharmacogenomics and Personalized Medicine*. Dove Medical Press Ltd November 2017, pp 267–278. https://doi.org/10.2147/PGPM.S87945.

(147) Corrales, L.; Glickman, L. H.; McWhirter, S. M.; Kanne, D. B.; Sivick, K. E.; Katibah, G. E.; Woo, S. R.; Lemmens, E.; Banda, T.; Leong, J. J.; Metchette, K.; Dubensky, T. W.; Gajewski, T. F. Direct Activation of STING in the Tumor Microenvironment Leads to Potent and Systemic Tumor Regression and Immunity. *Cell Rep.* **2015**, *11* (7), 1018–1030. https://doi.org/10.1016/j.celrep.2015.04.031.

(148) Yum, S.; Li, M.; Frankel, A. E.; Chen, Z. J. Roles of the CGAS-STING Pathway in Cancer Immunosurveillance and Immunotherapy. *Annu. Rev. Cancer Biol.* **2019**, *3* (1), 323–344. https://doi.org/10.1146/annurev-cancerbio-030518-055636.

(149) Ishikawa, H.; Barber, G. N. STING Is an Endoplasmic Reticulum Adaptor That Facilitates Innate Immune Signalling. *Nature* **2008**, *455* (7213), 674–678. https://doi.org/10.1038/nature07317.

(150) Sun, L.; Wu, J.; Du, F.; Chen, X.; Chen, Z. J. Cyclic GMP-AMP Synthase Is a Cytosolic DNA Sensor That Activates the Type I Interferon Pathway. *Science (80-.).* **2013**, *339* (6121), 786–791. https://doi.org/10.1126/science.1232458.

(151) Chen, Q.; Sun, L.; Chen, Z. J. Regulation and Function of the CGAS-STING Pathway of Cytosolic DNA Sensing. *Nature Immunology*. Nature Publishing Group September 2016, pp 1142–1149. https://doi.org/10.1038/ni.3558.

(152) Kanasty, R.; Dorkin, J. R.; Vegas, A.; Anderson, D. Delivery Materials for SiRNA Therapeutics. *Nat. Mater.* **2013**, *12* (11), 967–977. https://doi.org/10.1038/nmat3765.

(153) Allen, T. M.; Cullis, P. R. Liposomal Drug Delivery Systems: From Concept to Clinical Applications. *Advanced Drug Delivery Reviews*. January 2013, pp 36–48. https://doi.org/10.1016/j.addr.2012.09.037.

(154) Semple, S. C.; Akinc, A.; Chen, J.; Sandhu, A. P.; Mui, B. L.; Cho, C. K.; Sah, D. W. Y.; Stebbing, D.; Crosley, E. J.; Yaworski, E.; Hafez, I. M.; Dorkin, J. R.; Qin, J.; Lam, K.; Rajeev, K. G.; Wong, K. F.; Jeffs, L. B.; Nechev, L.; Eisenhardt, M. L.; Jayaraman, M.; Kazem, M.; Maier, M. A.; Srinivasulu, M.; Weinstein, M. J.; Chen, Q.; Alvarez, R.; Barros, S. A.; De, S.; Klimuk, S. K.; Borland, T.; Kosovrasti, V.; Cantley, W. L.; Tam, Y. K.; Manoharan, M.; Ciufolini, M. A.; Tracy, M. A.; De Fougerolles, A.; MacLachlan, I.; Cullis, P. R.; Madden, T. D.; Hope, M. J. Rational Design of Cationic Lipids for SiRNA Delivery. *Nat. Biotechnol.* **2010**, *28* (2), 172–176. https://doi.org/10.1038/nbt.1602.

(155) Jayaraman, M.; Ansell, S. M.; Mui, B. L.; Tam, Y. K.; Chen, J.; Du, X.; Butler, D.; Eltepu, L.; Matsuda, S.; Narayanannair, J. K.; Rajeev, K. G.; Hafez, I. M.; Akinc, A.; Maier, M. A.; Tracy, M. A.; Cullis, P. R.; Madden, T. D.; Manoharan, M.; Hope, M. J. Maximizing the Potency of SiRNA Lipid Nanoparticles for Hepatic Gene Silencing in Vivo. *Angew. Chemie - Int. Ed.* **2012**, *51* (34), 8529–8533. https://doi.org/10.1002/anie.201203263.

(156) Pearson, A. M.; Rich, A.; Kriegers, M. *THE JOURNAL OF BlOLOCICAL CHEMISTRY Polynucleotide Binding to Macrophage Scavenger Receptors Depends on the Formation of Base-Quartet-Stabilized Four-Stranded Helices**; 1993; Vol. 268.

(157) Arteta, M. Y.; Kjellman, T.; Bartesaghi, S.; Wallin, S.; Wu, X.; Kvist, A. J.; Dabkowska, A.; Székely, N.; Radulescu, A.; Bergenholtz, J.; Lindfors, L. Successful Reprogramming of Cellular Protein Production through MRNA Delivered by Functionalized Lipid Nanoparticles. *Proc. Natl. Acad. Sci. U. S. A.* **2018**, *115* (15), E3351–E3360. https://doi.org/10.1073/pnas.1720542115.

(158) Pozzi, D.; Marchini, C.; Cardarelli, F.; Amenitsch, H.; Garulli, C.; Bifone, A.; Caracciolo, G. Transfection Efficiency Boost of Cholesterol-Containing Lipoplexes. *Biochim. Biophys. Acta - Biomembr.* **2012**, *1818* (9), 2335–2343. https://doi.org/10.1016/j.bbamem.2012.05.017.

(159) Ramishetti, S.; Hazan-Halevy, I.; Palakuri, R.; Chatterjee, S.; Naidu Gonna, S.; Dammes, N.; Freilich, I.; Kolik Shmuel, L.; Danino, D.; Peer, D. A Combinatorial Library of Lipid Nanoparticles for RNA Delivery to Leukocytes. *Adv. Mater.* **2020**, *32* (12), 1906128. https://doi.org/10.1002/adma.201906128.

(160) Kauffman, K. J.; Mir, F. F.; Jhunjhunwala, S.; Kaczmarek, J. C.; Hurtado, J. E.; Yang, J. H.; Webber, M. J.; Kowalski, P. S.; Heartlein, M. W.; DeRosa, F.; Anderson, D. G. Efficacy and Immunogenicity of Unmodified and Pseudouridine-Modified MRNA Delivered Systemically with Lipid Nanoparticles in Vivo. *Biomaterials* **2016**, *109*, 78–87. https://doi.org/10.1016/j.biomaterials.2016.09.006.

(161) Patel, P. C.; Giljohann, D. A.; Daniel, W. L.; Zheng, D.; Prigodich, A. E.; Mirkin, C. A.

Scavenger Receptors Mediate Cellular Uptake of Polyvalent Oligonucleotide-Functionalized Gold Nanoparticles. *Bioconjug. Chem.* **2010**, *21* (12), 2250–2256. https://doi.org/10.1021/bc1002423.

(162) Zhang, Y. N.; Poon, W.; Tavares, A. J.; McGilvray, I. D.; Chan, W. C. W. Nanoparticle–Liver Interactions: Cellular Uptake and Hepatobiliary Elimination. *J. Control. Release* **2016**, *240*, 332–348. https://doi.org/10.1016/j.jconrel.2016.01.020.

(163) Proffitt, R. T.; Williams, L. E.; Presant, C. A.; Tin, G. W.; Uliana, J. A.; Gamble, R. C.; Baldeschwieler, J. D. Liposomal Blockade of the Reticuloendothelial System: Improved Tumor Imaging with Small Unilamellar Vesicles. *Science (80-.).* **1983**, *220* (4596), 502–505. https://doi.org/10.1126/science.6836294.

(164) Nagayama, S.; Ogawara, K. ichi; Fukuoka, Y.; Higaki, K.; Kimura, T. Time-Dependent Changes in Opsonin Amount Associated on Nanoparticles Alter Their Hepatic Uptake Characteristics. *Int. J. Pharm.* **2007**, *342* (1–2), 215–221. https://doi.org/10.1016/j.ijpharm.2007.04.036.

(165) Taylor, P. R.; Martinez-Pomares, L.; Stacey, M.; Lin, H. H.; Brown, G. D.; Gordon, S. Macrophage Receptors and Immune Recognition. *Annual Review of Immunology*. Annu Rev Immunol 2005, pp 901–944. https://doi.org/10.1146/annurev.immunol.23.021704.115816.

(166) Khalil, D. N.; Smith, E. L.; Brentjens, R. J.; Wolchok, J. D. The Future of Cancer Treatment: Immunomodulation, CARs and Combination Immunotherapy. *Nature Reviews Clinical Oncology*. Nature Publishing Group May 1, 2016, pp 273–290. https://doi.org/10.1038/nrclinonc.2016.25.

(167) Whitehead, K. A.; Dorkin, J. R.; Vegas, A. J.; Chang, P. H.; Veiseh, O.; Matthews, J.; Fenton, O. S.; Zhang, Y.; Olejnik, K. T.; Yesilyurt, V.; Chen, D.; Barros, S.; Klebanov, B.; Novobrantseva, T.; Langer, R.; Anderson, D. G. Degradable Lipid Nanoparticles with Predictable in Vivo SiRNA Delivery Activity. *Nat. Commun.* **2014**, *5*, 4277. https://doi.org/10.1038/ncomms5277.

(168) Paunovska, K.; Sago, C. D.; Monaco, C. M.; Hudson, W. H.; Castro, M. G.; Rudoltz, T. G.; Kalathoor, S.; Vanover, D. A.; Santangelo, P. J.; Ahmed, R.; Bryksin, A. V.; Dahlman, J. E. A Direct Comparison of in Vitro and in Vivo Nucleic Acid Delivery Mediated by Hundreds of Nanoparticles Reveals a Weak Correlation. *Nano Lett.* **2018**, *18* (3), 2148–2157. https://doi.org/10.1021/acs.nanolett.8b00432.

(169) Cheng, C. J.; Tietjen, G. T.; Saucier-Sawyer, J. K.; Saltzman, W. M. A Holistic Approach to Targeting Disease with Polymeric Nanoparticles. *Nature Reviews Drug Discovery*. 2015. https://doi.org/10.1038/nrd4503.

(170) Milane, L.; Amiji, M. Clinical Approval of Nanotechnology-Based SARS-CoV-2 MRNA Vaccines: Impact on Translational Nanomedicine. *Drug Deliv. Transl. Res.* **2021**, 1. https://doi.org/10.1007/S13346-021-00911-Y.

(171) Dong, Y.; Siegwart, D. J.; Anderson, D. G. Strategies, Design, and Chemistry in SiRNA Delivery Systems. *Adv. Drug Deliv. Rev.* **2019**. https://doi.org/10.1016/J.ADDR.2019.05.004.

(172) Melamed, J. R.; Ioele, S. A.; Hannum, A. J.; Ullman, V. M.; Day, E. S. Polyethylenimine–Spherical Nucleic Acid Nanoparticles against Gli1 Reduce the Chemoresistance and Stemness of Glioblastoma Cells. *Mol. Pharm.* **2018**, *15* (11), 5135–5145.

https://doi.org/10.1021/acs.molpharmaceut.8b00707.

(173) Duhlin, A.; Grasset, E. K.; He, C.; Amara, K.; Sippl, N.; Lindh, E.; Vargas, L.; Dahlberg, C.; Westerberg, L.; Smith, E. C.; Malmström, V.; Pierce, S. K.; Karlsson, M. C. Scavenger Receptor CD36 on B Cells Senses Modified Self-Antigens to Prevent Autoimmunity. *J. Immunol.* **2017**, *198* (1 Supplement).

(174) Platt, N.; Gordon, S. Scavenger Receptors: Diverse Activities and Promiscuous Binding of Polyanionic Ligands. *Chemistry and Biology*. Elsevier Ltd 1998. https://doi.org/10.1016/S1074-5521(98)90156-9.

(175) Sago, C. D.; Krupczak, B. R.; Lokugamage, M. P.; Gan, Z.; Dahlman, J. E. Cell Subtypes Within the Liver Microenvironment Differentially Interact with Lipid Nanoparticles. *Cell. Mol. Bioeng.* **2019**, *12* (5), 389. https://doi.org/10.1007/S12195-019-00573-4.

(176) Liu, Y.; Zhou, C.; Huang, S.; Dang, L.; Wei, Y.; He, J.; Zhou, Y.; Mao, S.; Tao, W.; Zhang, Y.; Yang, H.; Huang, X.; Chi, T. A Cas-Embedding Strategy for Minimizing off-Target Effects of DNA Base Editors. *Nat. Commun.* **2020**, *11* (1), 1–9. https://doi.org/10.1038/s41467-020-19690-0.

(177) Sentmanat, M. F.; Peters, S. T.; Florian, C. P.; Connelly, J. P.; Pruett-Miller, S. M. A Survey of Validation Strategies for CRISPR-Cas9 Editing. *Sci. Reports 2018 81* **2018**, *8* (1), 1–8. https://doi.org/10.1038/s41598-018-19441-8.

(178) X, L.; Y, Y.; H, Z.; T, Z.; Z, Y.; H, X.; Y, F.; F, L.; X, P.; L, L.; C, C.; M, H.; L, Y.; KK, W.; W, T. Enhanced in Vivo Blood-Brain Barrier Penetration by Circular Tau-Transferrin Receptor Bifunctional Aptamer for Tauopathy Therapy. *J. Am. Chem. Soc.* **2020**, *142* (8), 3862–3872. https://doi.org/10.1021/JACS.9B11490.

(179) Ritz, S.; Schöttler, S.; Kotman, N.; Baier, G.; Musyanovych, A.; Kuharev, J.; Landfester, K.; Schild, H.; Jahn, O.; Tenzer, S.; Mailänder, V. Protein Corona of Nanoparticles: Distinct Proteins Regulate the Cellular Uptake. *Biomacromolecules* **2015**, *16* (4), 1311–1321. https://doi.org/10.1021/ACS.BIOMAC.5B00108.

(180) Lundqvist, M.; Stigler, J.; Elia, G.; Lynch, I.; Cedervall, T.; Dawson, K. A. Nanoparticle Size and Surface Properties Determine the Protein Corona with Possible Implications for Biological Impacts. *Proc. Natl. Acad. Sci.* **2008**, *105* (38), 14265–14270. https://doi.org/10.1073/pnas.0805135105.

(181) Mohammad-Beigi, H.; Hayashi, Y.; Zeuthen, C. M.; Eskandari, H.; Scavenius, C.; Juul-Madsen, K.; Vorup-Jensen, T.; Enghild, J. J.; Sutherland, D. S. Mapping and Identification of Soft Corona Proteins at Nanoparticles and Their Impact on Cellular Association. *Nat. Commun. 2020 111* **2020**, *11* (1), 1–16. https://doi.org/10.1038/s41467-020-18237-7.

(182) Hoogenboezem, E. N.; Duvall, C. L. Harnessing Albumin as a Carrier for Cancer Therapies. *Adv. Drug Deliv. Rev.* **2018**, *130*, 73–89. https://doi.org/10.1016/J.ADDR.2018.07.011.

(183) Zhang, R.; El-Mayta, R.; Murdoch, T. J.; Warzecha, C. C.; Billingsley, M. M.; Shepherd, S. J.; Gong, N.; Wang, L.; Wilson, J. M.; Lee, D.; Mitchell, M. J. Helper Lipid Structure Influences Protein Adsorption and Delivery of Lipid Nanoparticles to Spleen and Liver †. *Cite this Biomater. Sci* **2021**, *9*, 1449. https://doi.org/10.1039/d0bm01609h.

(184) J, Z.; Z, D.; L, J.; C, Y.; J, L.; H, S.; W, H.; Y, S. Spleen-Derived Anti-Inflammatory Cytokine IL-10 Stimulated by Adipose Tissue-Derived Stem Cells Protects Against Type

2 Diabetes. *Stem Cells Dev.* **2017**, *26* (24), 1749–1758. https://doi.org/10.1089/SCD.2017.0119.

(185) Day, H. A.; Pavlou, P.; Waller, Z. A. E. I-Motif DNA: Structure, Stability and Targeting with Ligands. *Bioorg. Med. Chem.* **2014**, *22* (16), 4407–4418. https://doi.org/10.1016/J.BMC.2014.05.047.

(186) Peruzzi, J. A.; Jacobs, M. L.; Vu, T. Q.; Wang, K. S.; Kamat, N. P. Barcoding Biological Reactions with DNA-Functionalized Vesicles. *Angew. Chemie* **2019**, *131* (51), 18856–18863. https://doi.org/10.1002/ANGE.201911544.

(187) Riley, R. S.; Kashyap, M. V.; Billingsley, M. M.; White, B.; Alameh, M.-G.; Bose, S. K.; Zoltick, P. W.; Li, H.; Zhang, R.; Cheng, A. Y.; Weissman, D.; Peranteau, W. H.; Mitchell, M. J. Ionizable Lipid Nanoparticles for in Utero MRNA Delivery. *Sci. Adv.* **2021**, *7* (3), eaba1028. https://doi.org/10.1126/SCIADV.ABA1028.

(188) Paunovska, K.; Loughrey, D.; Sago, C. D.; Langer, R.; Dahlman, J. E. Using Large Datasets to Understand Nanotechnology. *Adv. Mater.* **2019**, *31* (43), 1902798. https://doi.org/10.1002/adma.201902798.

(189) T, R.; Z, Q.; KM, N. Avoiding Common Pitfalls When Clustering Biological Data. *Sci. Signal.* **2016**, *9* (432). https://doi.org/10.1126/SCISIGNAL.AAD1932.

(190) Lynn, G. M.; Sedlik, C.; Baharom, F.; Zhu, Y.; Ramirez-Valdez, R. A.; Coble, V. L.; Tobin, K.; Nichols, S. R.; Itzkowitz, Y.; Zaidi, N.; Gammon, J. M.; Blobel, N. J.; Denizeau, J.; de la Rochere, P.; Francica, B. J.; Decker, B.; Maciejewski, M.; Cheung, J.; Yamane, H.; Smelkinson, M. G.; Francica, J. R.; Laga, R.; Bernstock, J. D.; Seymour, L. W.; Drake, C. G.; Jewell, C. M.; Lantz, O.; Piaggio, E.; Ishizuka, A. S.; Seder, R. A.

Peptide–TLR-7/8a Conjugate Vaccines Chemically Programmed for Nanoparticle Self-Assembly Enhance CD8 T-Cell Immunity to Tumor Antigens. *Nat. Biotechnol.* **2020**, *38* (3), 320–332. https://doi.org/10.1038/s41587-019-0390-x.

(191) Yu, F.; Wei, C.; Deng, P.; Peng, T.; Hu, X. Deep Exploration of Random Forest Model Boosts the Interpretability of Machine Learning Studies of Complicated Immune Responses and Lung Burden of Nanoparticles. *Sci. Adv.* **2021**, *7* (22), eabf4130. https://doi.org/10.1126/SCIADV.ABF4130.

Andrew Sinegra

asinegra@u.northwestern.edu; (570) 441-3296; Linkedin

Experience

Northwestern University, International Institute for Nanotechnology (IIN) 2016-present
PhD Candidate, Biomedical Engineering

- Characterized structures of liposomes and lipid nanoparticles functionalized with DNA with goal of targeting drug delivery
- Assayed for nanoparticle delivery to both immune and non-immune cell types within tissues using multi-color flow cytometry
- Used Design of Experiment (DoE) process to reduce number of screening assays—this led to a ~100-fold decrease in minimum effective concentration compared to the original nanoparticle
- Analyzed mRNA expression and genome editing efficiency levels in mice after nanoparticle treatment
- Developed DNA barcode-indexed nanoparticles for high-throughput assessment of biodistribution using NGS
- Published co-authored research in high-impact journals such as *ACS Nano* (1 published, 1 submitted, 1 in preparation) and presented at national conferences such as the Biomedical Engineering Society (BMES) meeting

The University of Virginia School of Medicine 2014-2016
Undergraduate Student Opportunities in Academic Research (USOAR) Fellow

- Identified several long non-coding RNAs associated with brain tumor prognosis from RNA sequencing data and clinical data
- Measured effect of non-coding RNA silencing on brain tumor stem cells in invasion and migration assays
- Presented results at regional and national conferences

Education

Northwestern University June 2021(expected)
PhD Candidate in Biomedical Engineering

- Advisor: Prof. Chad A. Mirkin

Kellogg School of Management, Northwestern University 2020
Certificate in Management for Scientists and Engineers

- Selective program taught by Kellogg Faculty for PhD candidates to immerse students in topics such as finance, accounting, entrepreneurship, leadership, and intellectual property management

The University of Virginia 2016
B.Sc with High Distinction in Chemistry

- Undergraduate Student Opportunities in Academic Research (USOAR) fellowship recipient

Technical Skills

Materials: synthesis of liposomes and lipid nanoparticles; solid-phase synthesis of custom DNA and RNA, in vitro transcription of mRNA

Characterization: NanoSight; DLS; zeta potential; Luminex; Tangential flow filtration (TFF); HPLC, UPLC,

FPLC, MALDI-MS; SDS-PAGE

Biology: cell culture; cellular assays; ELISA; immunoassays; multi-color flow cytometry (FACS); qPCR; ddPCR; vector cloning; Western blotting; NGS library preparation; siRNA, mRNA, and CRISPR-Cas9 delivery

Computer: R, MATLAB; JMP; NGS data analysis; Adobe Creative Cloud

Leadership & Teamwork

Science Club | Northwestern University 2018-present
Volunteer Mentor

- Long-term, weekly mentoring of 4 Chicago public school students in an after-school science program
- Leading students in creating independent science projects for middle school science fair

Northwestern Biomedical Engineering Dept. 2019
Head Teaching Assistant

- Head teaching assistant for a 300-level Renal Physiology course with ~100 third year undergraduates
- Taught weekly sessions to lead students through quantitative problems
- Coordinated with four undergraduate teaching assistants to grade homework, exams

Science in Your Community Center (SICC) | Northwestern University 2016-2018
Volunteer Teacher

- Led Evanston middle school students in monthly exploratory science projects
- Organized interactive student tours of Northwestern research laboratories

Publications

Ferrer, J.R.†, **Sinegra, A.J.**†, Ivancic, D., Yeap, X.Y., Qiu, L., Wang, J., Zhang, Z.J., Wertheim, J.A., Mirkin, C.A. "Structure-Dependent Biodistribution of Liposomal Spherical Nucleic Acids". *ACS Nano*. **2020**. 14, 1682-1693.

Sinegra, A.J., Evangelopoulos, M., Park, J., Mirkin, C.A. "Lipid Nanoparticle Spherical Nucleic Acids for DNA and RNA Delivery". *Submitted*. **February 2020**.

† = equal contribution

Patents

Chad A. Mirkin and **Andrew J. Sinegra**. "Lipid Nanoparticle Spherical Nucleic Acids". **2021**. US Patent Application 63/136,501.

Contributed Talks (1 of 3)

"Probing Structure-Function Relationships to Optimize Liposomal Spherical Nucleic Acids for RNAi". *BMES National Meeting*, Atlanta, GA, **September 2018** (Oral).